

How Sperm Beat and Swim

From Filament Deformation to Activity

Inaugural-Dissertation

zur

Erlangung des Doktorgrades

der Mathematisch-Naturwissenschaftlichen Fakultät

der Universität zu Köln

vorgelegt von

Guglielmo Saggiorato
aus Noventa Vicentina, Italien

Jülich

2016

Berichterstatter: **Prof. Dr. Gerhard Gompper**
(Gutachter) **Prof. Dr. U. Benjamin Kaupp**

Tag der mündlichen Prüfung: 30th October 2015

*It is by logic that we prove,
but by intuition that we discover.
To know how to criticize is good,
to know how to create is better.*

H. POINCARÉ

Abstract

Understanding the dynamics of microbiological swimmers is a key element on the way to discovering biological mechanisms, to develop new sophisticated bio-mimetic technologies, e.g., artificial microswimmers, and to design novel microfluidic devices, e.g., for diagnosis applications. In this work, we focus on the dynamics of microswimmers with a slender flexible body, for which the *spermatozoon* is one of the best biological representatives.

The overarching theme of our investigation is the relation between elasticity and dynamics of semiflexible filaments, their hydrodynamic interactions and active motion.

We first study the dynamics of one, two and three sedimenting filaments in a viscous fluid. The dynamics of a settling filament is simpler than that of the beating flagellum because it is dominated only by the passive elastic restoring force. It allows a fundamental understanding of the dynamics generated by the competition of elastic and hydrodynamic forces. At the same time, the settling dynamics is of technological importance as it may suggest, e.g., new purification techniques. We find that the settling plane of an isolated semi-flexible filament is not always stable. When the external field is strong enough, the system encounters two (subsequent) dynamical transitions that break the planarity and chirality of the filament shape. New stationary settling shapes are found that correspond to drift and helical trajectories. Investigations with more filaments show that the settling dynamics may be much more rich than expected already at fields generated by modern centrifuges.

Sperm cells are composed of a mostly spherical head and a whip-like appendage called *flagellum*. The flagellum has an oscillatory movement that sustains a traveling wave from the head to the tail. The motion of the flagellum provides the thrust needed to propel the spermatozoon and generates a complex flow field. As an essential

step toward understanding the hydrodynamic cooperation between spermatozoa, we analyze high-speed experimental recording of pinned human sperm (in collaboration with researchers at the research center CAESAR, Bonn) and develop a minimal model of realistic beating. We infer the flagellum internal forces and, in the future, the generated flow field. It turns out that the model needs not to be complex and not to explicitly account for the observed left-right asymmetries in the rotational motion around the pinning point. The simulation closely reproduces the flagellum tracks recorded by high-speed video-microscopy, and the appropriate parameters are, thus, estimated directly from the experimental recordings. This is a new approach to extract also forces from the observed data in addition to the kinematics, as done by other established techniques.

The inspection of high-speed recording of human spermatozoa also leads us to suggest a novel mechanism to control the swimming direction of spermatozoa via higher harmonic components of the beating frequency. The proposed mechanisms explain the usual circular trajectories by a shape anisotropy, a curved flagellum or a bent midpiece. Although it may look puzzling at first that higher beating frequency break a spatial symmetry, we show that a simple model can explain the observed behavior and match simulations with experiments.

The beating pattern is not due to a predefined sinusoidal pacemaker, as used in the previous model. Instead, it is believed that the molecular motors distributed along the flagellum reach a self-organized state that generates the required force-pattern. Different models have been proposed to explain how the beating pattern is generated by a feedback system between molecular forces and flagellum shapes; however, explicit simulations lead to unexpected buckling instabilities. Thus, we present a simple mathematical (and later computational) model that is not bounded to a specific biomechanical hypothesis on the traits of the molecular motors. The resulting model highlights the difference between different feedback responses that couple the axoneme shape to the molecular motors forces. Among the possible models, we choose the model with the smoothest and the most regular behavior as we expect that, because of the variability of the biological environment and of the resilience of spermatozoa in the most disparate conditions, any representative model

of active beating should not display ill-defined behaviors. The model is applied to the fascinating and contemporary investigation of the active response of the beating pattern to controlled perturbations. By numerical integration of the model, we quantify how the beating pattern (amplitude, frequency and wave vector) is affected by the medium viscosity and we show that it is possible to entrain the beating frequency to an external periodic force as generated in experimental setup or by other, surrounding, spermatozoa. This top-down approach provides a simple reference model that allows both investigation of small scale details and investigation of large cooperative assemblies of swimmers.

Kurzzusammenfassung

Das Verständnis der Dynamik von mikrobiologischen Schwimmen ist ein Schlüsselement auf dem Weg zur Entdeckung von biologischen Mechanismen, zur Entwicklung neuer anspruchsvoller biomimetischer Technologien, z.B. künstlicher Mikroschwimmer, und zur Entwicklung neuartiger mikrofluidischer Systeme, z.B. für Diagnoseanwendungen. Im Fokus der vorliegenden Doktorarbeit steht die Dynamik von Mikroschwimmern mit filament-artiger Form und hoher Flexibilität, für die *Spermien* einer der besten biologischen Vertreter sind.

Das übergreifende Thema der Arbeit ist das Wechselspiel von Elastizität und Dynamik von semiflexiblen Filamenten, deren hydrodynamische Wechselwirkungen und ihrer aktiven Bewegung.

Wir untersuchen zuerst die Dynamik von einem, zwei und drei sedimentierenden Filamenten in einer viskosen Flüssigkeit. Die Sedimentationsdynamik eines passiven Filaments ist einfacher als die eines schlagenden Flagellums, weil sie nur durch die passive elastische Rückstellkraft bestimmt wird. Dies ermöglicht ein grundlegendes Verständnis der durch die Konkurrenz von elastischen und hydrodynamischen Kräften erzeugten Dynamik. Gleichzeitig hat die Sedimentationsdynamik technologische Bedeutung, z.B. für neue Reinigungsmethoden kolloidaler Suspensionen. Wir zeigen, dass die Deformationsebene eines isolierten flexiblen Filaments nicht immer stabil ist. Wenn das äußere Feld stark genug ist, ereignen sich zwei aufeinander folgende dynamische Übergänge, die die Planarität und die Chiralität der Filament-Deformation betreffen. Dies führt zu neuen stationären Sedimentationsformen, die Drift- und Spiraltrajektorien entsprechen. Die Untersuchung von mehreren Filamenten zeigt, dass die Sedimentationsdynamik vielfältiger ist. Die hierfür notwendigen Beschleunigungen können von modernen Zentrifugen problemlos erzeugt werden.

Spermien bestehen aus einem kugelförmigen Kopf und einem peitschen-ähnlichen

Schwanz, der als *Flagellum* oder *Geißel* bezeichnet wird. Das Flagellum macht einer oszillierenden wellenförmigen Bewegung, die sich vom Kopf zum Schwanzende hin fortpflanzt. Die Bewegung des Flagellums liefert den Schub, welcher erforderlich ist um das Spermium voran zu treiben und erzeugt außerdem ein komplexes Strömungsfeld. Als einen wesentlicher Schritt zum Verständnis der hydrodynamischen Kooperation zwischen Spermatozoen analysieren wir experimentelle Hochgeschwindigkeitsaufnahmen von Kopf fixierter menschlicher Spermien (in Zusammenarbeit mit Forschern vom Forschungszentrum CAESAR, Bonn) und entwickeln ein minimales Modell für realistische Schlagmuster des Flagellums. Daraus ergeben sich die internen Kräfte, und in Zukunft das erzeugte Strömungsfeld. Es stellt sich heraus, dass das Modell nicht allzu komplex sein muss und die beobachteten Links-Rechts-Asymmetrien in der Drehbewegung um den Fixierungspunkt nicht explizit modelliert werden müssen. Die Simulation reproduziert die Bewegung des Flagellums, die durch Hochgeschwindigkeits-Video-Mikroskopie erfasst wurde; geeignete Modell-Parameter können somit direkt aus den experimentellen Aufnahmen abgeschätzt werden. Dies ist ein neues Konzept, um zusätzlich zur Kinematik, die mit anderen etablierten Techniken beschrieben werden kann, auch Kräfte aus den beobachteten Daten zu extrahieren.

Die Untersuchung der Hochgeschwindigkeitsaufnahmen menschlicher Spermatozoen führt ebenfalls zur Entdeckung eines neuen Mechanismus, wie Spermien die Schwimmrichtung durch höhere harmonische Komponenten der Schlagfrequenz steuern können. Die bisher vorgeschlagenen Mechanismen erklären die beobachteten Kreisbahnen durch eine Formanisotropie, entweder durch ein gekrümmtes Flagellum oder durch ein gebogenes Mittelstück. Obwohl es auf den ersten Blick rätselhaft erscheint, dass auch höhere Harmonische der Schlagfrequenz die räumliche Symmetrie brechen können, erklärt ein einfaches Modell das beobachtete Verhalten; eine quantitative Auswertung zeigt, dass die Simulationen mit den Experimenten sehr gut übereinstimmen.

Das Schlagmuster wird in diesem Fall nicht durch einen vordefinierten sinusförmigen Schrittmacher erzeugt, wie er im vorherigen Modell verwendet wurde. Stattdessen wird angenommen, dass die entlang der Geißel verteilten molekularen Motoren selbst-

organisiert das erforderliche Kraftmuster erzeugen. Verschiedene Modelle wurden vorgeschlagen, um zu erklären, wie das Schlagmuster durch ein Rückkopplungssystem zwischen aktiven molekularen Kräften und der Form und Elastizität des Flagellums erzeugt wird; explizite Simulationen solcher Modelle führen jedoch zu unerwarteten Knickinstabilitäten. Daher stellen wir ein einfaches mathematisches Modell-Schema vor, das keine spezifischen biomechanischen Hypothesen über die Merkmale der molekularen Motoren beinhaltet. Die resultierenden Modelle betonen den Unterschied zwischen den verschiedenen Rückkopplungsmechanismen, durch die die Form des Axonems mit den Kräften der molekularen Motoren gekoppelt wird. Unter den möglichen Modellen wählen wir das mit dem glattesten und regelmässigsten Verhalten aus. Aufgrund der Variabilität der biologischen Umgebung und der Widerstandsfähigkeit von Spermien unter verschiedensten Bedingungen sollte ein repräsentative Modell des aktiven Flagellenschlags kein irreguläres Verhaltensmuster aufweisen. Das Modell wird dann zur Untersuchung der aktiven Regulation des Schlagmusters auf äußere Störungen angewendet. Durch numerische Integration des Modells quantifizieren wir, wie das Schlagmuster (Amplitude, Frequenz und Wellenvektor) durch die Viskosität des Mediums beeinflusst wird und zeigen, dass es möglich ist, die Schlagfrequenz mit einem externen periodischen Kräften zu synchronisieren, wie sie in Experimenten z.B. durch andere umgebende Spermien erzeugt werden können. Dieser Top-down-Ansatz liefert ein einfache Referenzmodell, das sowohl zur Untersuchung von Details des Schlagmusters einzelner Spermien als auch zur Untersuchung des kollektiven Verhaltens großer Schwärme von Mikroschwimmern geeignet ist.

Contents

1. Introduction	1
2. Filaments, Elasticity, and Hydrodynamics	9
2.1. Hydrodynamics	9
2.2. Swimming with a semi-flexible filament	12
2.3. Semi-flexible filaments	19
2.4. Coupling Hydrodynamics and Elasticity	25
2.5. Active Axonemes	27
3. Models and Methods	31
3.1. Molecular dynamics simulations	31
3.1.1. Forces	32
3.2. Data Analysis	34
3.2.1. Discussion	38
3.3. Spectrogram	40
3.4. Filament Modes	41
4. Sedimenting Filaments	43
4.1. Introduction	43
4.2. Results	46
4.2.1. Deformation and Dynamics of Single Filament	46
4.2.2. Conformations and Dynamics of Two Interacting Filaments	48
4.2.3. Three Filaments	56
4.3. Discussion and Conclusions	58

5. Flagellar Beat of Pinned Human Sperm	61
5.1. Quantitative description of sperm beating	62
5.2. Steering with Higher Harmonics	69
5.2.1. Resistive-Force Theory	71
5.2.2. Derivation of the Net Normal Force	72
5.2.3. High-speed Microscopy of the Beat Pattern of Human Sperm	77
5.2.4. Simulations of Human Sperm	80
5.2.5. Summary	85
5.3. Dissipation and Work	86
5.4. Concluding remarks	88
6. Autonomous Flagellar Beating	91
6.1. Early Failed Attempts	92
6.2. Dynamic Ginzburg-Landau Approach	95
6.3. Linear theory	97
6.3.1. Eigenvalues and model selection	97
6.4. Nonlinear model	101
6.4.1. Internal and external viscous dissipation	102
6.4.2. Dynamical behavior	104
6.5. Discussion	107
7. Concluding Summary	109
8. Outlook	113
Appendices	115
A. Adaptive time-step Velocity-Verlet	117
Bibliography	121

Definitions

In this thesis, we discuss of biological arguments that do not belong to the background of most physicists. To clarify some common sources of confusion (at least, common for the author), we summarize in this list some of the most frequent terms that do not belong to the vocabulary of classical physics. The definitions are intentionally simplified with respect to what can be found in technical publications:

Axoneme Biomechanical structure formed of 9 double-microtubules arranged in a cylindrical conformation, some times surrounding a pair of simple microtubules. This structure forms the core of eukaryote flagella and cilia

Cilium (Plural: Cilia) Whip-like appendages of eukaryote cells, shorter than spermatozoa, whose periodic movement has two moments: a fast stroke and a slow recovery motion.

Eukaryote Any organism whose nucleus is membrane-bounded. Example: *Paramecium*

Flagellum (Plural: Flagella) Whip-like appendage developed by certain prokaryote and eukaryote cells as sensory systems and motility mechanism. *Bacterial* flagella are helical filaments connected to a motor at the base. *Eukaryotic* flagella have a complex internal arrangements of microtubules and the shape is defined by internally modulated forces.

Motor proteins/Molecular motor “Motor proteins are enzymes that convert the chemical energy derived from the hydrolysis of ATP into mechanical work used to drive cell motility.”[1] There are different molecular motors depending on the function, on the walking substrate and, even, on the walking direction.

The motors found between microtubules in the axoneme are called (Axonemal) dyneins (see Fig. 1.4).

Prokaryote Organism made of a single cell whose nucleus is not membrane-bound and lacks of mitochondria and other membrane-bound organelles. Example: *E. Coli*

Sperm Mature male reproductive cell or the male gamete.

Spermatium A non-motile sperm cell.

Spermatozoon (Plural: Spermatozoa) A uniflagellar motile sperm cell.

1. Introduction

We, living and adapting the world to our needs, are integrated and surrounded by a multitude of life forms. Zoology, biology and, recently, microbiology show us how diverse forms of life developed, pushed by evolutionary forces. It is common belief that most of the life forms be tailored to fill a particular niche, balancing their use or re-use of nutrients and “free energy”, all together belonging to a network where everyone is needed.

Microorganisms are important waste recyclers that re-insert carbon and other heavier elements that cannot be synthesized by biological processes in the food chain. Their presence inside our body in a positive symbiotic interaction (digestion) or as pathogenic sources determines our daily life. The sheer importance in the ecological systems is widely recognized [2]. Acquaintance with the biological and physical aspects is vital to the understanding of our impact on such systems, to their exploitation [3], and to the development of micro-robots [4] and innovative bio-mimetic technology.

Here we focus on a tiny portion of the biophysics panorama: microswimmers; whose foundative studies trace back to the works of Gray and Hancock [5] and of Berg [6]. For microorganisms bigger than $\approx 1 \mu m$ active directed swimming can be an advantage over simple diffusion [2]. Among the different microorganisms that actively move, we will focus on those that mostly live in a fluid environment, that developed a flagellum (a whip-like appendage), and that are eukaryote. Fig. 1.1(inner circle) shows an overview of the big variety of organisms that swim thanks to the movement of one or many flagella. Flagella are flexible organelles that elegantly generate the thrust with a non-reciprocal periodic motion (Fig 1.3). At these scales, indeed, a simple periodic paddling would not generate thrust because the equation of motion of the fluid is time-reversible and does not distinguish fast or slow strokes [7–9].

1. Introduction



Figure 1.1.: A general overview of microorganisms with flagella and related organisms. From Ref. [10].

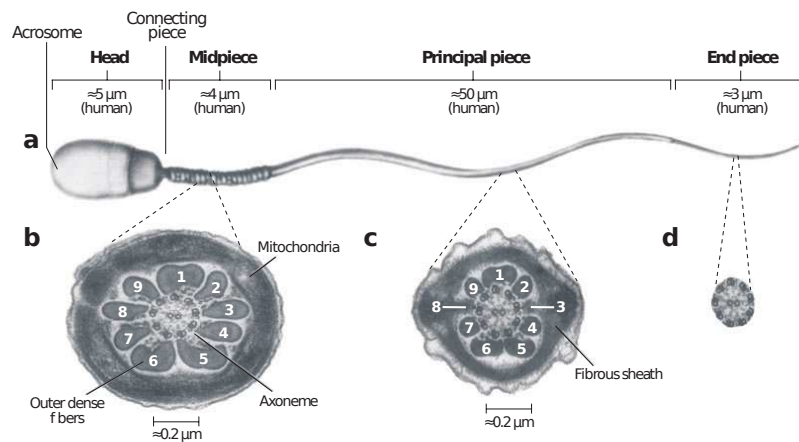


Figure 1.2.: Illustration of a mammalian sperm (adapted from Ref. [14]). **a)** Regions of the sperm flagellum and approximate lengths. **b)** Cross-section of the midpiece. The microtubule doublets and associated fibers are numbered with the usual convention. **c)** and **d)** Cross section of the principal and end pieces.

Among the flagellated eukariote microorganisms, sperm cells have a particular role, being the male gamete that is actively responsible for the ovum fertilization and, ultimately, for the organism reproduction. Sperm cells come in a variety of different shapes: some have many flagella [11], some heads are spatulate-shaped, other falciform-shaped [12], and length and size too, vary quite considerably from species to species. Indeed, one may think that spermatozoa are a mammals' affair, but that is not the case. We are surrounded by these small cells as they are produced and released also by trees [11], insects [13] and molluscs [5]. This highlights how the sperm cells, although very diverse from species to species, are a remarkable piece of biology, adapted to very diverse and adverse environments, while still retaining their fundamental functions.

Sperm cells are not like other regular microorganisms: they do not divide nor feed or hunt; they behave more like “single-use machines”¹: their life-program being simplified into “find the ovum” then “fertilize it”. From some points of view, they may seem simpler than proper organisms which need, e.g., to feed or to live in colonies, nonetheless there are still many questions to answer about their delicate taxis and

¹Thanks to Prof. B. Kaupp for this mind-opening definition.

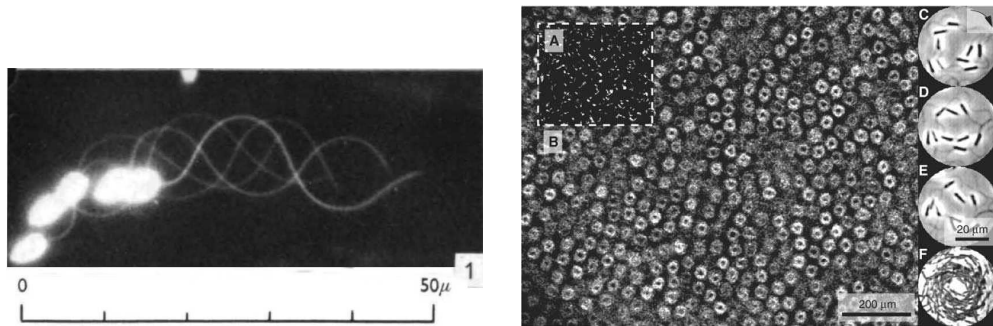


Figure 1.3.: **Left:** Stroboscopic picture of a spermatozoon (sea urchin) swimming from right to left. The bright ellipse is the head, the line is the flagellum. Image from Ref. [16]. **Right:** High-density structures developed by sea urchin spermatozoa. The vortexes are formed by ~ 10 cells. Image from Ref. [17].

steering mechanisms, and the ultimate influence on sperm motility and the ovum fertilization [14, 15].

In the following we consider only the case of *spermatozoa*: a uniflagellated sperm cell, produced by, e.g., humans, bulls and sea urchins and for this reason we employ the words *sperm* and *sperm cells* with the same meaning of *spermatozoa*.

The stroboscopic picture of a swimming sea urchin sperm (Fig. 1.3(left)) shows that the swimming thrust is a consequence of the bending wave that propagates downward the flagellum ($\approx 30 - 80 \mu m$ in length and $\approx 1 - 2 \mu m$ in size, $\approx 10 - 60 Hz$ [2, 14]). The flagellum pushes the cell body or head ($\approx 5 \mu m$) containing the highly packed DNA and some cytoplasm. The connection between cell body and flagellum differs from species to species. In the case of sea urchin the connection resembles a free joint, while in the human spermatozoon the flagellum is stiffly connected to the body. The portion of flagellum that is nearer to the body is said *midpiece* [12]: in the human spermatozoon, it is surrounded by mitochondria, it is then thicker and does not bend as much as the remaining length (Fig. 1.2).

The single isolated spermatozoon does not trustfully represent the swimming conditions as sperm cells are often released in bulks. The ensuing cooperative behavior is a very fascinating aspect of sperm motility, and a manifestation of self-organization in nature. Theoretical and numerical investigations showed that hydrodynamics and steric interaction lead to the formation of clusters [18, 19], similarly to other models

of self-propelled rods and spheres [20]. It is possible to describe the collective behavior also with Vicsek-like models, that means reducing each organism into few stereotyped, effective degrees of freedom. In this case the self-organization is formulated as a critical phenomenon [21]. Steric and mechanical interaction, and effective behavior are just the first guesses to describe the fascinating interactions due to the bigger number of (relevant) degrees of freedom of the real biological ensemble. Some species, indeed, developed *ad-hoc* features: e.g. the sperm cells of wood mouse, *A. Sylvaticus*, have a hook used to anchor cells in trains of cells belonging to the *same* male mate. Probably thanks to the hydrodynamic interaction between cells belonging to the same cluster, they travel at higher velocities than the isolated sperm and, it is believed, it strengthens the chances than one of the sperms of the cluster fertilizes the ovum [22, 23].

In Fig. 1.3 another example of cooperation is shown: when sea urchin spermatozoa (*S. Droebachiensis* and *S. Purpuratus*) swim at high density (≈ 2500 cells/mm²) the cells self-organize in vortexes on a hexagonal lattice [17]. The relevance of the observation is clear when the attention is shifted from models with few “effective” degrees of freedom [21], to the actual physical and biological mechanisms of pattern formation. Depending on the context, pattern formation mechanisms may involve different processes: from the diffusion of chemical species [24–26] to advection fluxes, and (at least in ecology) non-local terms due to, e.g., roots spreading [27]. In Ref. [17] it is proposed, *for the first time*, that the underlying mechanism forming the vortexes be the hydrodynamic interaction between the organisms, that couples to the flagellar dynamics thanks to some yet-unknown mechanisms.

Let’s inspect the single flagellum more carefully, then, to understand how this mechanism may work. At the flagellum core we find the *axoneme* (Fig. 1.4), $\approx 0.2–0.5\mu\text{m}$ in diameter [1, 14], surrounded by a soft “skin” of proteins. The axoneme provides the biomechanical stability to the, otherwise soft, surrounding proteins and hosts the molecular motors [14]. The axoneme comprises 9 microtubule-doublets around a pair of central microtubules [28] and dynein arms on the outer filaments that generate shear forces between the filaments, ultimately generating the bending moments [29–31]. The axoneme is not unique of spermatozoa as it is a highly preserved structure,

1. Introduction

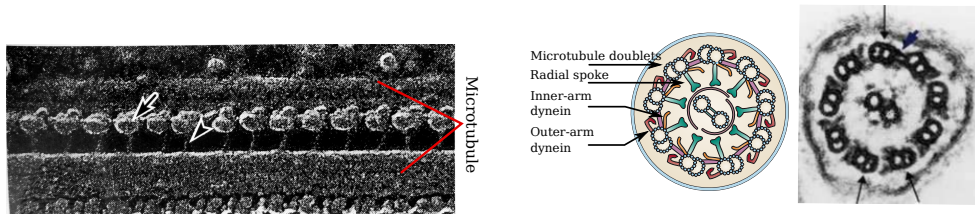


Figure 1.4.: **Left:** Longitudinal section of two microtubules show the position and packing of the dyneins. The stalks (simple arrow) are separated by $\approx 24nm$. Image from Ref. [1], **Right:** Illustration and cross-section of the 9+2 morphology of the axoneme (*Chlamydomonas*, $\times 218.000$). The short arrow indicate the beak-like protrusion of the dynein arms. Images from Refs. [34, 36]

found also in cilia [32] and in the trypanosome [33, 34]. Curiously, cilia are believed to form metachronal waves as consequence of hydrodynamic interaction [35], even though there are some peculiar differences with the spermatozoa.

The axoneme is the common biomechanical structure between cilia and spermatozoa. Since it plays a nodal role for the beating, it may be responsible for the self-organized swimming as well. The axoneme allows the generation of bending torques throughout the flagellum. It was soon realized, indeed, that since the beating amplitude does not decrease at one side despite the strong dissipation of the surrounding fluid, energy must be provided all along the flagellum length [29, 37]. The mechanism generating the beat pattern draws a lot of attention since the early works in Ref. [38]. It is well accepted that the bending forces are due to sliding forces generated between adjacent microtubules by the dynein arms (Fig. 1.4) [37–39]. Because of the very fast beating frequency and wave velocity ($\approx 1\text{ mm/s}$), it is not possible to describe the wave as the effect of a biochemical signal. It is instead proposed that the beating pattern itself is due to a self-organization of molecular motors. Fig. 1.3 can then be seen as a self-organized motion of self-organized beating patterns!! From this point of view, the problem of active beating and self-organized swimming is a unique system to investigate physics models of interacting organisms whose behavior is not predefined but the result of the dynamics of internal degrees of freedom and external forces.

Models of active beating are then required to distinguish the effect of pure mechan-

ical forces, from active ones. Developments in the ability to manipulate and interact with the single cell [40–42], allow investigating whether cooperative behaviors can be understood as the result of mechanical forces (e.g. hydrodynamics or steric interaction), of behavioral or signaling responses, or of others yet-unknown mechanisms. In the latest works two main approaches have been proposed to model the beating pattern in terms of either molecular-motor traits [43–45] or mechanical properties of the filament bundle [46, 47]. But, at the moment of writing, no active model has been used to investigate the response to external perturbations.

The overarching theme of our investigation is the relation between elasticity and dynamics of semiflexible filaments, their hydrodynamic interactions and active motion. Bearing in mind that we do not want to discuss how an idealized system reproduces the observed behaviors, but rather how a realistic system really works, we approach the investigation from different sides in the spirit of *Divide et Impera*.

In this thesis we initially present some original results about the hydrodynamic interaction of one, two and three sedimenting filaments. The dynamics of sedimentation is simpler than that of the beating, and allows developing some basic understanding on the relation between elasticity and hydrodynamic forces and on the quantification of filament shapes.

As we want to understand the hydrodynamic cooperation between spermatozoa, we focus on the design of a simulation model that closely reproduces the dynamics of a pinned (human) spermatozoa near a surface, and so the driving forces and the generated flow field. Inspection of high-speed recording of human spermatozoa led us to a new exciting observation: a novel mechanism to control the swimming direction of spermatozoa via higher harmonic components of the beating frequency. At the same time we are left with a new minimalistic model of “realistic” beating of human spermatozoon, driven by predefined forces. Appropriate parameters are, thus, estimated directly from the experimental recordings, without micro-manipulation techniques [48].

Finally, to go beyond the predefined-forces model, we present a novel approach to model the self-organized beating pattern. The idea is to develop a simple mesoscopic model: simple enough to be implemented in more complex simulations with full

1. Introduction

hydrodynamics and simple enough to allow theoretical investigations on the biomechanical structure of the axoneme. With the keen idea to start simple and generic, we have been inspired by the models of non-linear chemistry and reaction-diffusion equations [24]. The resulting framework represents an alternative approach not (yet) bounded to a specific biomechanical model of molecular motors, it highlights the difference between some of the proposed models, and it allows a systematic theoretical investigation of the axonemal response to controlled perturbations².

As always in physics, we understand a physical process via our models and theories, their underlying assumptions and limitations. In the next chapter we recall some background concepts widely used throughout this thesis:

1. Hydrodynamics at low-Reynolds number and of immersed slender objects,
2. Dynamics for semi-flexible inextensible filaments,
3. Dynamics of elastic filaments interacting with fluid,
4. Dynamics of a model axoneme.

²Private communication with experimental groups in TU Delft and DAMTP highlighted a similar interest, and some (very) early results with *Chlamydomonas* look promising.

2. Filaments, Elasticity, and Hydrodynamics

2.1. Hydrodynamics

Since we are interested in microswimmers, we are naturally concerned also of the movement of bodies in a fluid. Any movement of the immersed body propagates to elements of volume of the fluid, whose resistance itself allows the swimmer to move. We present in this section some theoretical approaches to understand and model the equations of motion of both the fluid and the swimmer, with particular regard to slender bodies.

Navier-Stokes equation

An incompressible fluid can be described by the velocity field \mathbf{u} , the constant density ρ and the energy $k_B T$. The dynamics of an element of fluid in position \mathbf{r} subject to a pressure field \mathbf{p} and external force field \mathbf{f} is determined by the energy and momentum conservation equation complemented with the incompressibility constrain:

$$\begin{aligned} \rho \left(\frac{\partial \mathbf{u}}{\partial t} + \mathbf{u} \cdot \nabla \mathbf{u} \right) &= -\nabla \mathbf{p} + \eta \nabla^2 \mathbf{u} + \mathbf{f}_{\text{ext}} \\ \nabla \cdot \mathbf{u} &= 0 \end{aligned} \quad (2.1)$$

The first equation is the Navier-Stokes equation.

On the left-hand side of the Navier-Stokes equation the material derivative describes the acceleration and convective transport of the element of mass. Note that the convective term is the only non-linear term. On the right-hand side the term

$\eta\nabla^2\mathbf{u}$ describes the momentum exchange between layers of fluid with different velocities. The coupling term η is the (dynamic) viscosity: a phenomenological property of the fluid that cannot be deduced by the conservation laws. Given appropriate boundary conditions and external forces Eq. (2.1) can, in principle, be solved. They pose, however, an incredible problem that has not found a general solution yet.

Low-Reynolds number and Scallop theorem

In nature we find organisms that move in different fluids, like air or water, and at different velocity and length scales like sea whales, birds, spermatozoa, and bacteria. We can imagine assigning a characteristic length scale L and velocity scale v_0 at each creature and to rescale the Navier-Stokes equation accordingly; obtaining

$$Re \left(\frac{\partial \mathbf{u}'}{\partial t'} + \mathbf{u}' \cdot \nabla' \mathbf{u}' \right) = -\nabla' p + \eta' \nabla'^2 \mathbf{u}' + \mathbf{f}'_{\text{ext}} \quad (2.2)$$

where prime indicates the new dimensionless quantities.

The quantity $Re = \rho v_0 L / \eta$ is the Reynolds number: its value spans few orders of magnitude from the 10^{-5} of bacteria to the 10^4 of medium-size fishes [8]. Its importance resides on the fact that it defines the relative importance between the inertial forces of the fluid and the viscous forces. At high Reynolds number the motion of a body transfers momentum to the surrounding fluid, that is then convected, and slowly dissipated. On the contrary, at low Reynolds numbers there is no transport of momentum nor an inertial (delay) time between the application of the forces and the fluid response. There may be several characteristic length and velocity scales in a given system and corresponding different Reynolds number. This is not an issue as long as the Reynolds number is not confused as an absolute property of the system but, rather, of the observables of interest. For example: if one is interested on the dynamics of the single sperm cell, an appropriate choice of length and velocity can be the body length and velocity; on the contrary, if the details of fluid field near the flagellum are of interest, probably the beating amplitude and frequency provide more insight.

In this work we focus on the dynamics of the full body of spermatozoa, whose

Reynolds number is typically small and the left-hand side of Eq. (2.2) can be neglected. The remaining equation is called Stokes equation; it is a linear equation, with no explicit time derivative:

$$\nabla p - \eta \nabla^2 \mathbf{u} = \mathbf{f}_{\text{ext}} . \quad (2.3)$$

Thus, the mathematical formulation of the fluid past a microorganism poses a simpler problem than that for larger creatures; however, giving away the linearity and the inertial forces affects quite a lot the physics with some counter-intuitive effects [7].

First: In this Aristotelian world all forces are instantaneously balanced [10, 49]: when a microswimmer's flagellum or cilia halts, the body velocity vanishes in nanoseconds because all the momentum transferred to the fluid has been (almost) instantaneously dissipated.

Second: Eq. (2.3) is symmetric under time inversion because the time derivative is gone. This signifies the velocity \mathbf{u} and pressure \mathbf{p} fields follow instantaneously the external force $\mathbf{f}_{\text{ext}}(t)$ that the swimmer imposes on the fluid. As consequence, the dynamics for $\mathbf{f}_{\text{ext}}(-t)$ will be exactly the reverted dynamics. From the perspective of a microswimmer, this really complicates life. Most of the propulsion mechanisms in nature employ a cyclic motion, e.g. walking, flying, fish swimming are all based on the same cyclic pattern of movements repeated over and over. The same approach applied by a simple microswimmer with 1 d.o.f. would not work: the forces generated in the first half cycle would balance the forces in the second half cycle. At the best, the creature would oscillate, with no net center-of-mass displacement [50]. This is called the "Scallop theorem" [7]. Microswimmers must have a time-irreversible propulsion and a mechanism that involves more than one degree of freedom. From a theoretical point-of-view the simpler of such model-swimmers can be realized with two degrees of freedom [51]. Real microswimmers, however, developed refined and sophisticated mechanisms. For the microswimmers we are concerned with, we highlight that ciliated cells and sperm cells flagella actively bend their shape, and in doing so they develop periodic patterns that break the left-right or top-bottom symmetry, thus generating the propulsive force.

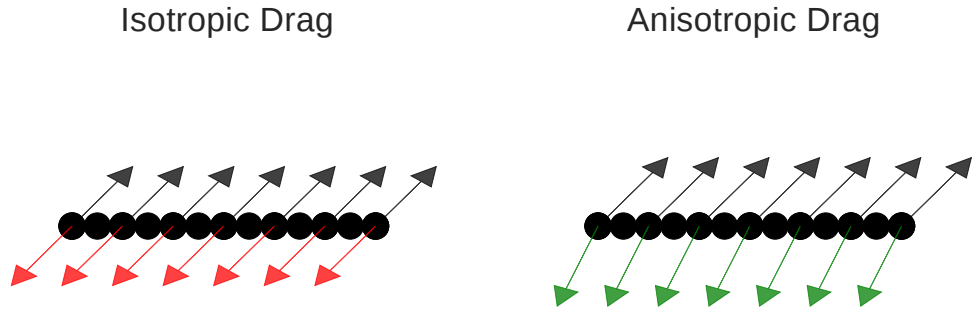


Figure 2.1.: Illustration of the resistive force theory applied to a rod composed of beads. The rod moves in the direction of the gray arrows. If the drag is isotropic (**left**) then the viscous drag (red arrows) is parallel to the velocity. An anisotropic drag (**right**) develops a drag force (green arrows) that is not parallel to the direction of the velocity but more oriented in the normal direction.

2.2. Swimming with a semi-flexible filament

How does the motion of an extended slender body generates the forces to self-propel in a viscous fluid? We present some theoretical concepts proposed to describe the interaction between moving slender objects in a fluid beginning with a phenomenological description in the first subsection, to continue then with a more theoretical description in the following.

Resistive-force theory

Let's consider a stiff rod of length L dragged by a force \mathbf{f} in a viscous fluid. It moves faster when pulled along its longitudinal direction rather than when dragged along its normal direction. We can say that the friction coefficients depend on the direction the body is moving with respect to some body-axes; in the particular case of a straight rod two directions are defined (Fig. 2.1):

$$\begin{aligned} \mathbf{u}_{\perp} &= \xi_{\perp}^{-1} \mathbf{f}_{\perp} && \text{Perpendicular,} \\ \mathbf{u}_{\parallel} &= \xi_{\parallel}^{-1} \mathbf{f}_{\parallel} && \text{Parallel.} \end{aligned} \quad (2.4)$$

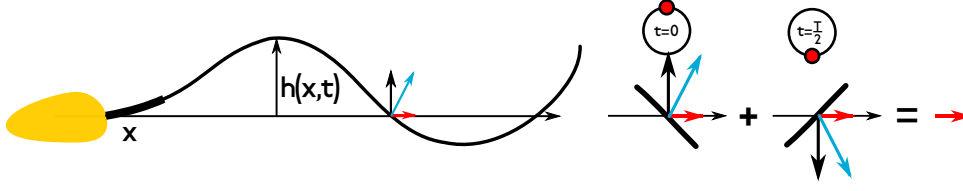


Figure 2.2.: Illustration of resistive-force theory applied to a beating flagellum with period T . At the beginning ($t = 0$) a part of the flagellum is moving upwards (black arrow). The flagellum is locally approximated by a rod, whose drag force (blue line) is not directed along the direction of the velocity, but it has a bigger component normal to the flagellum. A force along the \hat{x} direction (red arrow) is so generated. After half a period the flagellum comes back, but because it is moving with wave-like motion, its local orientation is inverted too, and so are the forces. Nonetheless, the force component parallel \hat{x} (red line) still points in the same direction and sums up to the previous one.

One of consequences of the anisotropic drag is that the drag-force is not parallel to the velocity, but it is more intense along the normal direction to the rod (Fig. 2.1). This simple observation allows explaining how the periodic motion of the spermatozoon generates a net thrust: let us assume that the motion of a small segment of the flagellum (Fig. 2.2) is, essentially, along the y direction. In the absence of anisotropic drag the force in the first half period is $\mathbf{f}_1 = \xi u_1 \hat{y}$, equal and opposite to the force generated in the second half a period $\mathbf{f}_2 = \xi u_2 \hat{y} = -\xi u_1 \hat{y}$ (Fig. 2.2, black arrows), where ξ is the drag coefficient and $u_{1,2}$ is the velocity of the small segment. The anisotropic drag, instead, projects part of the resistance force along the positive \hat{x} direction; thus the forces generated in the two half periods have the same net contribution along the swimming direction (Fig. 2.2, red arrows).

Gray and Hancock [5] showed and verified experimentally that the swimming velocity is indeed due to the imbalance between perpendicular and parallel drag of the flagellum (Fig. 2.2):

$$\mathbf{u} = -\frac{1}{2} \left(\frac{\xi_{\perp}}{\xi_{\parallel}} - 1 \right) A^2 \omega k \left(\frac{1}{1 + h a k / 2\pi} \right), \quad (2.5)$$

where the flagellum is described by a single traveling wave $y(t, s) = A \sin(kx - \omega t)$

2. Filaments, Elasticity, and Hydrodynamics

propagating from negative to positive x , $h\xi_{\parallel}$ is the head drag coefficient and a the characteristic size of the head. This equation highlights few important aspects:

1. a traveling wave propagating along a slender filament can cause a net force on the microswimmer and the velocity is proportional to the drag anisotropy $\xi_{\perp}/\xi_{\parallel} - 1$.
2. the force pushes in the opposite direction with respect to the wave velocity. The sum of the forces on the fluid and on the body being, indeed, zero.

This is a very intuitive conclusion and calculations based on anisotropic drag, said “resistive-force theory”, have been successful also in describing the motion of other swimmers, e.g. *E. Coli* [10]. One way to measure experimentally the drag coefficients is by fitting Eq. (2.5) to the swimming velocity: for bull sperm it yields $\xi_{\parallel} = 0.69 \pm 0.62 \text{ fNs}\mu\text{m}^{-2}$ and $\xi_{\perp}/\xi_{\parallel} = 1.81 \pm 0.07$ [52].

Thus, we have seen that a rod has two main drag coefficients and this can explain the mechanism of swimming for slender bodies. Usually, however, the coefficients ξ_{\perp} and ξ_{\parallel} are not known for arbitrary shapes and it is natural to wonder how to estimate theoretically the perpendicular and parallel drag in complicate, possibly not-constant, shapes. In the most general case, every slender shape that moves in a fluid exerts forces the fluid itself and the effective drag-coefficient will be due to the continuously changing contributions of the distant parts of the body. In general then, it is not possible to define a “perpendicular” or “parallel” direction only. This make the problem very complicate but from a theoretical point of view, it is desirable to “squeeze” the non-local hydrodynamic interaction to a description in terms of local drag-coefficients. The treatment of these questions, specialized to slender objects, is the subject of the “*Slender-body theory*” [10, 49, 53, 54].

Stokeslets and Slender-Body Theory

The motion of a viscous fluid past a swimming microorganism of shape $S(t)$ obeys the momentum-balance equation [8]:

$$\begin{aligned}\nabla p - \eta \nabla^2 \mathbf{u} &= 0 \\ \nabla \cdot \mathbf{u} &= 0.\end{aligned}\tag{2.6}$$

Usually, swimmers are impenetrable to the fluid flow, hence Eq. (2.6) is complemented with the boundary condition that the flow adheres to the surface $S(t)$ and has the same velocity. Despite the innocent aspect of Eq. (2.6), this problem can be solved only in few lucky cases. We need an alternative approach to understand the propulsion of extended objects.

A more convenient way is to tackle the problem from the opposite point of view: a swimmer applies forces on the fluid, whose velocity and pressure fields p and \mathbf{u} are given by the Stokes equation. By linearity, the flow generated by any complex distribution of forces can be written as a sum of “fundamental flows” generated by point forces along the moving surface [8, 10].

The fundamental solution of Stokes equation (Eq. (2.3)) with external force given by $\mathbf{f}\delta(\mathbf{r})$ and boundary condition given by zero velocity at $|\mathbf{r}| = \infty$ is called “stokeslet”. The pressure and velocity fields read:

$$p(\mathbf{r}) = \nabla \cdot \left[-\frac{\mathbf{f}}{4\pi r} \right]\tag{2.7}$$

$$\begin{aligned}\mathbf{u}(\mathbf{r}) &= H(\mathbf{r}) \mathbf{f}, \quad \mathbf{u}(|\mathbf{r}| = \infty) = 0 \\ &= \frac{1}{8\mu\pi r} (\mathbb{1} + \hat{\mathbf{e}}\hat{\mathbf{e}}^T) \mathbf{f}\end{aligned}\tag{2.8}$$

where $r = |\mathbf{r}|$ is the distance from the point-force, $\hat{\mathbf{e}} = \mathbf{r}/r$ and $H(\mathbf{r})$ is the Oseen tensor. Eq. (2.8) shows that the velocity field is made of a component *parallel* to \mathbf{f} , equivalent to the velocity generated by a sphere of radius r moving with the same velocity, and a *radial* component given by the dyadic product that modifies the first one with a second-order surface-harmonic [10].

2. Filaments, Elasticity, and Hydrodynamics

We can finally write the flow field generated by a distribution of forces as superposition of stokeslets with force densities $\mathbf{f}\delta(\mathbf{r}(s))$ along a curve whose centerline is parametrized by the curvilinear coordinate s as [8, 10]:

$$\mathbf{u}(s) = \frac{\mathbf{f}}{4\pi\mu} + \int_{|\mathbf{r}(s)-\mathbf{r}(s')|>\delta} ds' H(\mathbf{r}(s), \mathbf{r}(s'))\mathbf{f}(\mathbf{r}(s')) \quad (2.9)$$

where the cut-off $\delta \approx \frac{1}{2}\sqrt{\epsilon}a \sim 1.36a$ accounts for the finite radius a of the distribution.

The general solution of Eq. (2.9) is not known, but it is readily computed for the simple case of a rod parallel to the \hat{x} axis, with radius a and length $L \gg a$. Each point along the filament experiences a drag force that depends its distance from the middle point:

$$\begin{aligned} \mathbf{u}_{\parallel}(x) &= \frac{\mathbf{f}_{\parallel}}{8\pi\mu} \left(1 + \log \frac{4x(L-x)}{a^2}, 0, 0 \right) \\ \mathbf{u}_{\perp}(x) &= \frac{\mathbf{f}_{\perp}}{8\pi\mu} \left(0, -2 + 2 \log \frac{4x(L-x)}{a^2}, 0 \right), \end{aligned} \quad (2.10)$$

as long as x is far from the filament ends (in 0 and L). The drag coefficients are finally found integrating along the rod to obtain

$$\begin{aligned} \xi_{\parallel}^{\text{rod}} &= \frac{4\pi\mu L}{\log(L/a) + \alpha} \\ \xi_{\perp}^{\text{rod}} &= \frac{2\pi\mu L}{\log(L/a) + \beta}. \end{aligned} \quad (2.11)$$

Note that:

1. The constants α and β depend on the boundary conditions and the aspect-ratio. To first order, however, they are constants: $\alpha = 0.84$, $\beta = -0.20$ [1, 50, 55]
2. Eq. (2.10) shows a logarithmic dependence on the distances from the cylinder ends. Phenomenologically, this means that the drag increases towards the ends and it is minimum at the midpoint
3. When $L/a \gg 1$, the ratio between the perpendicular and parallel velocity is almost two

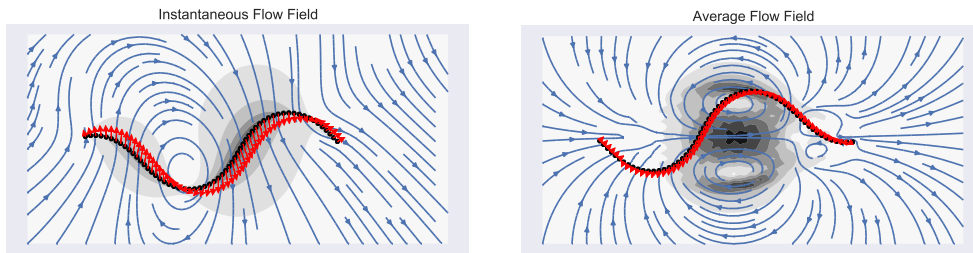


Figure 2.3.: Instantaneous and average flow field generated by a filament moving with assigned curvature $C(s, t) = C_0 \sin(\omega t + qs)$. Given the size and velocity of each point, the flow field is obtained from Eq. (2.9). The black points represent the filaments, the red arrows are the instantaneous local velocities and the blue lines are the stream lines.

4. In the limit of infinitely long filament, the terminal velocity diverges. This is a well know paradox. However, in practical cases one always deals with finite lengths and the problem has no relevance.

This method shows that we can, at least formally, reproduce the hydrodynamics features of extend slender object by discretizing them as spherical beads of radius a .

Concluding remarks on swimming slender bodies

Thus, we have seen that the simplification introduced by imposing a force on the fluid instead of boundary conditions allows rewriting the flow generated by a moving slender body in the simpler form of Eq. (2.9), and that using Slender-body theory and the fundamental solutions of the Stokes equation it is possible to estimate the resistive-force drag-ratios of a thin rod. For more complex objects the solution of Eq. (2.9) becomes prohibitively complicated, even more so if we consider the time-changing shape of, for example, a beating flagellum or cilium. In Fig. 2.3 we visualize the computed flow-field generated by a wave-like filament.

To overcome the difficulties introduced when applying Eq. (2.9) to biological cases, one may be tempted to approximate the curved shape as a series of short rods. This has the advantage of removing any non-local term, by precomputing them in the anisotropic drag. In this way, however, the choice of the rod-length determines also the cut-off length for the hydrodynamic interaction; the value of the rod length and

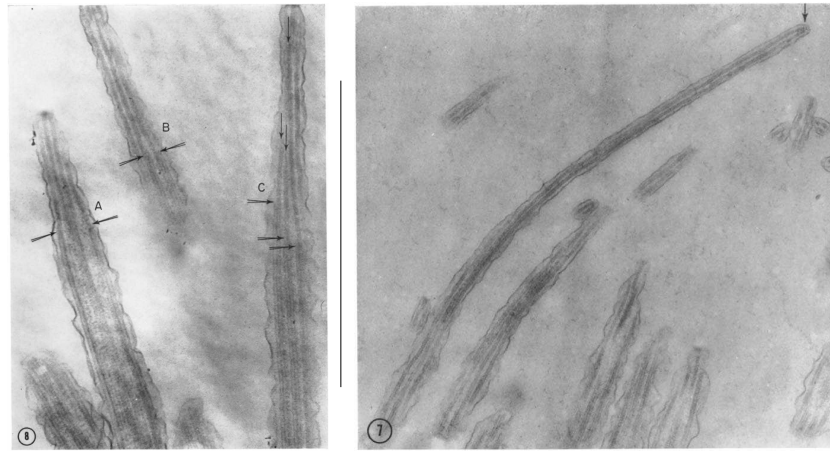


Figure 2.4.: Lateral view of cilia tips. Note the microtubule-doublers that form the axoneme. Arrows indicate the probable ending points. From Ref. [28].

radius should not be regarded anymore as geometrical quantities, but as effective parameters that require to be fine tuned in order to reproduce the experimental data. Interestingly, it turns out that to match the experimental data, the value of L should be replaced by the wavelength of the beating flagellum (see Ref. [5, 10, 54] for further details). A different approach is to neglect completely the Slender-body theory and to fit the swimming velocity against the drag coefficients as done in Ref. [52].

In more complex geometries, as well as in the case of interacting sperm, it is not correct to precompute the long-range terms. It is in this case that simulations really show all their power [18].

In the previous discussion of hydrodynamics at low Reynolds number and slender bodies we implicitly assumed that the shape of the body is given. This may be the case for some systems, but it is not the most general one. In general, bodies are not infinitely stiff and when fluid flow exerts some forces on them, their reaction can include a deviation from the expected shape. Before discussing this problem, we present in the next section some theoretical models and observations on flexible slender-bodies.

2.3. Semi-flexible filaments

Polymers are ubiquitous in microbiological context: the most famous examples being DNA and proteins [56]. Recently [57], interest has grown on another class of polymer assemblies: actin, intermediate filaments, and microtubules; they are called *semi-flexible filaments* to highlight that the bending energy is enough to out-compete the entropic forces. Their relevant role in cellular mechanics is well accepted [1, 57, 58]: on the contrary to the previous class of soft-polymers, this new class has a striking structural difference: they can sustain loads and exert forces. Their contribution on the formation of cellular cytoskeleton is well known, and recent investigations are highlighting their contribution to the formation many other structures, e.g. *lamellipodia* and *podosomes* [59, 60]. Often these biomechanical structures are not formed by a single filament alone, but by many filaments aligned in cross-connected bundles with improved stability and higher buckling threshold [57, 61].

The axoneme, clearly, belong to the category of bundles of filaments (Fig. 2.4). In this thesis we assumed that the bundles are weakly cross linked: this means that the effective bending rigidity is simply the sum of stiffnesses of individual filaments. In the opposite case of cross-linked bundles the effective bending rigidity depends on the deformation [62]. In theoretical physics the standard model of a continuous semi-flexible polymer is the Worm-like chain [56]. In the remaining of this section we briefly present its equilibrium and dynamical traits.

When the position $\mathbf{r}(s)$ of the filament is parametrized by the curvilinear coordinate s along the filament centerline, the potential energy is readily written as the sum of two contributions: a term that penalizes the bending, and a term that penalizes the stretching [63]:

$$\begin{aligned}
 G &= G_{\text{bending}} + G_{\text{stretching}} \\
 &= \frac{\kappa}{2} \int ds \left[(\partial_s^2 \mathbf{r})^2 - (\partial_s^2 \mathbf{r} \cdot \hat{\mathbf{t}})^2 \right] + \\
 &\quad + \frac{\sigma}{2} \int ds [|\partial_s \mathbf{r}| - 1]^2, \tag{2.12}
 \end{aligned}$$

where $\hat{\mathbf{t}} = \partial_s \mathbf{r} / |\partial_s \mathbf{r}|$ is the unit tangent vector, κ is the bending modulus, and σ is

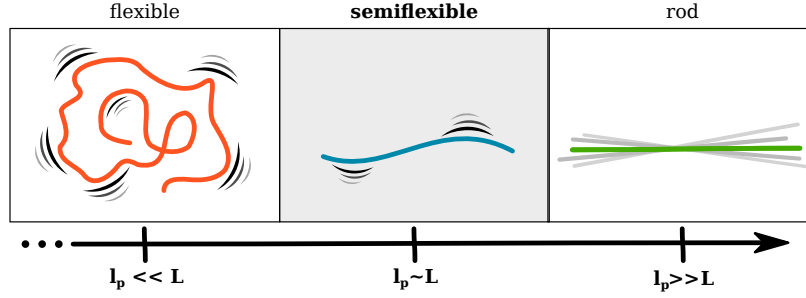


Figure 2.5.: Illustration of classification of polymers in terms of their persistence length at equilibrium. **(Left:)** The polymer is said flexible and usually modeled as a Rouse chain and thermal energy dominates the conformations. **(Right:)** The polymer is stiff, thermal energy is not enough to strongly affect the polymer conformation. **(Middle:)** The polymer is said semi-flexible: the thermal energy and bending rigidity compete. The conformations are mostly straight, but deviations are visible.

the “stretching” modulus.

The interpretation of the potential energy is simple: the *second* integral vanishes when the tangent vector has velocity 1, hence when there is not stretching, the *first* integral vanishes when there is no bending. Note that the second contribution to the bending energy is due to the parametrization of the filament (see Ref. [63] for a detailed explanation). Biological filaments are essentially inextensible. With a parametrization that embeds this constrain there is no need for the corresponding energy terms. Such parameterization, in 2D, is given by the curvature $C(s)$:

$$\mathbf{r}(s) = \mathbf{r}_0 + \int_0^s ds' \begin{pmatrix} \cos \psi(s') \\ \sin \psi(s') \end{pmatrix} \quad (2.13)$$

where $\psi(s) = \int_0^s ds' C(s')$ is the angle between the curve and the \hat{x} axis. It is easily verified that, since $|\partial_s \mathbf{r}| = 1$ and $\partial_s^2 \mathbf{r} = C \cdot \hat{\mathbf{n}}$, the potential energy simplifies to:

$$G_\psi = \frac{\kappa}{2} \int ds (\partial_s^2 \mathbf{r})^2. \quad (2.14)$$

The bending modulus can be related to the material property and geometry as:

$$\kappa = EI \propto Ea^4, \text{ [Energy} \times \text{Length]} \quad (2.15)$$

where E is the Young's modulus, I the area moment of inertia and a the filament radius. The moment of inertia is $\frac{\pi}{4}a^4$ for a cylindrical section, for other sections it has different prefactors but, as long as $a \ll C^{-1}$, it is always proportional to a^4 .

When the filament is in equilibrium with a thermal bath, the ratio between the bending modulus κ and the thermal bath energy¹ $k_B T$ defines the *persistence length* $l_p = \kappa/k_B T$. Intuitively, the persistence length is the length over which the polymer appears straight despite the fluctuations (Fig. 2.5):

$$\langle \hat{\mathbf{t}}(s) \cdot \hat{\mathbf{t}}(0) \rangle \sim e^{-|s|/l_p}. \quad (2.16)$$

Note that the intuitive (and geometrical) interpretation has a very precise meaning only at equilibrium and for polymers whose relaxed state is straight [56]. Given the definition of the persistence length, the gyration radius reads [1]:

$$\langle \mathbf{R} \cdot \mathbf{R} \rangle = \left\langle \int_0^L ds \mathbf{t} \cdot \int_0^L ds \mathbf{t} \right\rangle = 2l_p^2 \left(e^{-L/l_p} - 1 + L/l_p \right). \quad (2.17)$$

We move now to the introduction of basic concepts to model the dynamical behavior of semi-flexible filaments. From Eq. (2.14) we derive the equations of motion of an inextensible filament in a viscous fluid via the least-work principle [63, 64]:

$$\begin{aligned} \partial_t \mathbf{r} &= \left(\xi_{\perp}^{-1} \hat{n} \hat{n}^T + \xi_{\parallel}^{-1} \hat{t} \hat{t}^T \right) \cdot \frac{\delta G_{\psi}}{\delta \mathbf{r}} \\ &= \xi_{\perp}^{-1} \hat{n} \partial_s^4 \mathbf{r} \cdot \hat{n} + \xi_{\parallel}^{-1} \hat{t} \partial_s^4 \mathbf{r} \cdot \hat{t}, \end{aligned} \quad (2.18)$$

where $\delta G_{\psi}/\delta \mathbf{r}$ is the functional derivative of the potential G_{ψ} with respect to the filament configurations \mathbf{r} . Eq. (2.18) has to be complemented with boundary conditions

¹ $k_B T = 4.1 \text{ pN nm}$ at 24° C .

2. Filaments, Elasticity, and Hydrodynamics

that, for free ends read

$$\partial_s^2 \mathbf{r} \big|_{s=0,L} = \partial_s^3 \mathbf{r} \big|_{s=0,L} = 0. \quad (2.19)$$

Note that Eq. (2.18) is not linear because \hat{n} and \hat{t} themselves depend on the configuration \mathbf{r} . An approximated equation in terms of small deviations from the rest state provide very useful insight. It is, in principle, possible to expand either the tangent angle or the displacement from the rest line. Let begin with the tangent angle $\psi = \psi_0 + \epsilon\psi_1 + \epsilon^2\psi_2 + o(\epsilon^3)$, where ϵ is a small positive parameter. Small tangent angles correspond to an almost straight configuration, hence $\psi_0 = 0$. Substituting Eq. (2.13) in Eq. (2.18), using the fact $\partial_t(\partial_s \mathbf{r}) = \partial_t \psi \hat{\mathbf{n}}$ and collecting by equal orders in ϵ , we obtain (for the first two orders):

$$\begin{aligned} 0 &= 0 + \epsilon^2 \left[\xi_{\perp}^{-1} (\psi_1 \partial_s^3 \psi_1) + \xi_{\parallel}^{-1} (-3\partial_s \psi_1 \partial_s^3 \psi_1 - 3(\partial_s^3 \psi_1)^2) \right] \\ -\kappa^{-1} \partial_t \psi &= \epsilon \xi_{\perp}^{-1} \partial_s^4 \psi_1 + \epsilon^2 \xi_{\perp}^{-1} \partial_s^4 \psi_2. \end{aligned} \quad (2.20)$$

Expanding the configuration in small normal deviations $h = (\mathbf{r} - \mathbf{r}_0) \cdot \hat{\mathbf{n}}$ [57, 64](Fig. 2.2):

$$\begin{aligned} \mathbf{r} &= \mathbf{r}_0 + \int_0^x ds \begin{pmatrix} \cos \psi(s) \\ \sin \psi(s) \end{pmatrix} \underset{\psi \rightarrow 0}{\approx} \mathbf{r}_0 + \begin{pmatrix} x \\ h(x) \end{pmatrix} = \\ &= \mathbf{r}_0 + \begin{pmatrix} x \\ \epsilon h_1(x) + \epsilon^2 h_2(x) + \dots \end{pmatrix}. \end{aligned} \quad (2.21)$$

and inserting Eq. (2.21) in Eq. (2.18), yields:

$$\partial_t \begin{pmatrix} x_0 \\ h \end{pmatrix} = -\kappa \begin{pmatrix} \epsilon^2 (\xi_{\perp}^{-1} - \xi_{\parallel}^{-1}) \partial_s^4 h_1 \partial_s h_1 \\ \epsilon \xi_{\perp}^{-1} \partial_s^4 h_1 + \epsilon^2 \xi_{\perp}^{-1} \partial_s^4 h_2 \end{pmatrix} \quad (2.22)$$

Equations 2.20 and 2.22 highlight some important aspects of the dynamics of an elastic body in a viscous fluid:

- To first order in the deviation from the straight line, the bending energy and

the perpendicular drag are the only terms that determine the dynamics,

- The inextensibility is a second order correction (see second line of Eq. (2.20)),
- Net forces along the swimming direction are generated by the second (and higher) order terms (Eq. (2.22)).

It is very instructive to spend some time on the linear dynamics, valid for “small” deviation from the rest configuration (see also Ref. [65] for further comments.) As shown by Eq. (2.22), the dynamics of small deviations is determined by the bending energy and perpendicular drag only and Eq. (2.18) reduces to the much simpler:

$$\xi_{\perp} \partial_t h = \kappa \partial_s^4 h. \quad (2.23)$$

Despite the seemingly limited range of validity, this equation is at the basis of the experimental measurement of the persistence length of biological filaments [57, 66]. Equilibrium measurements are based on the fluctuations-spectrum; indeed, a filament in equilibrium in contact with a thermal bath (ie. this means that Eq. (2.23) is complemented with white noise that satisfies the FDT theorem) fluctuates with power-spectrum:

$$\langle h_q(t) h_q(0) \rangle = \frac{2}{\kappa} \frac{k_B T}{L} \frac{1}{q^4} e^{-\omega(q)t} \quad (2.24)$$

where $q = 2\pi n/L$ is the wave vector of the Fourier modes and $\omega(q) = \kappa q^4 / \xi_{\perp}$. This approximation is valid when the end effects can be neglected (e.g. for fluctuations with short wavelength).

On the contrary to equilibrium measurements, it is possible to measure the persistence length by observing the response to controlled perturbations (see Ref. [66] for the details). In this case it is more convenient to introduce the proper normal modes of Eq. (2.23) in dimensionless units by measuring space in units of the filament length $s = L\alpha$ from the filament middle point and time in units of the relaxation time $t = \tau \frac{\xi_{\perp} L^4}{\kappa}$. We obtain:

$$\partial_{\tau} h(\tau, \alpha) = \partial_s^4 h(\tau, \alpha). \quad (2.25)$$

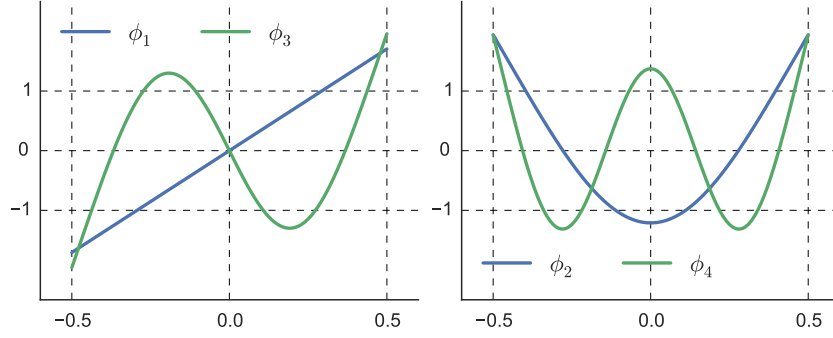


Figure 2.6.: Odd (**left**) and even (**right**) modes of the biharmonic operator with free boundary conditions at the sides.

Separation of variables is our best tools to construct a solution:

$$h(\alpha, \tau) = \sum_n \chi_n(\tau) \phi_n(\alpha),$$

where ϕ_n are the eigenfunctions of the biharmonic operator ∂_s^4 for $-1/2 < \alpha < 1/2$:

$$\begin{aligned} \phi_n(\alpha) &= a_n \cos(q_n \alpha) + b_n \sin(q_n \alpha) \\ &\quad + c_n \cosh(q_n \alpha) + d_n \sinh(q_n \alpha), \end{aligned} \quad (2.26)$$

with the eigenvalues q_n and factors a_n, b_n, c_n, d_n that depend on the boundary conditions [66–68]. In the case of free ends, if the origin of the arclength is in the middle of the filament, the parity of the modes becomes evident:

$$\begin{aligned} \phi_n(\alpha) &= \left(\frac{\cosh(\zeta_n \alpha)}{\cosh(\zeta_n/2)} + \frac{\cos(\zeta_n \alpha)}{\cos(\zeta_n/2)} \right), \quad n \text{ even} \\ \phi_n(\alpha) &= \left(\frac{\sinh(\zeta_n \alpha)}{\sinh(\zeta_n/2)} + \frac{\sin(\zeta_n \alpha)}{\sin(\zeta_n/2)} \right), \quad n \text{ odd}, \end{aligned} \quad (2.27)$$

where $\zeta_n = (n - 1/2)/\pi$ and $\tau_n = \left(\frac{\pi(n-1/2)}{L} \right)^4$. We plot the first 4 modes in Fig. 2.6.

Note that the Fourier modes are *not* a normal mode decomposition of Eq. (2.25). This means that, on the contrary of the normal modes given in Eq. (2.27), each Fourier mode will not display a single relaxation time. Nonetheless, the correct normal modes

can be approximated by the Fourier ones when the wavelength is small compared to the filament length or the problem allows discarding the dynamics at the filament ends [69].

2.4. Coupling Hydrodynamics and Elasticity

We introduce here some theoretical background on the motion of a slender deformable filaments inside a viscous fluid. We have seen in Eq. (2.10) that the viscous drag is not evenly distributed along a filament, being stronger at the edges than at the center. Classical slender body theory assumes the rod to be infinitely stiff and not deformable, hence the effective drag coefficients are obtained averaging the drag forces along the filament (Eq. (2.11)). This hypothesis is no longer valid when the body can deform, as it is in the case of semi-flexible filaments: the filament bends to comply to the uneven distribution of drag forces. The example of the elastic filament is a particular case of a more general behavior of deformable objects moving relative to a fluid (e.g. in Ref. [70] the sedimentation of a red blood cell was studied): the viscous drag that develops on the body's surface is not, in general, evenly distributed, hence objects deform to comply to the force; at the same time the new body shape generates new drag forces the body has to comply to; until a equilibrium configuration that balances drag forces and body forces is reached.

The dynamics of the position of a segment of the filament at position $r(\alpha, \tau)$ is determined by [67]:

$$\begin{aligned} \partial_\tau \mathbf{r}(\alpha, \tau) = & \int_{-1/2}^{1/2} d\alpha' \frac{1}{\gamma} \mathbf{I} \delta(\mathbf{r} - \mathbf{r}') [D(\alpha') \mathbf{r}' + \mathbf{f}'] + \\ & \int_{-1/2}^{1/2} d\alpha' H(\mathbf{r}, \mathbf{r}') [D(\alpha') \mathbf{r}' + \mathbf{f}'] \end{aligned} \quad (2.28)$$

where \mathbf{f} is the external force density, $\gamma = 3\pi\eta$ is the friction per unit length, D is the biharmonic operator $D = -\partial_\alpha^4$ that accounts for the bending energy, and $H(\mathbf{r}, \mathbf{r}')$ is the Oseen tensor [67, 71]. Eq. (2.28) has been written to enhance the similarity between its terms, but it can be split into its elementary contributions. Let us begin by noticing that each integral is the sum of two contributions: a term proportional

to the external field \mathbf{f} , that is equivalent to Eq. (2.9), and a term proportional to the bending rigidity $\partial_\alpha^4 \mathbf{r}$. Each term, in turn, can be seen as a contribution of a local term (first line) and a non-local term (second line).

Comparing Eq. (2.18) and Eq. (2.28) we recognize that the r.h.s. of the *first line* describes the elastic and external forces acting directly on position \mathbf{r} . The *second line* couples the local dynamics with the fluid flow generated in points far from \mathbf{r} .

The tensor $H(\mathbf{r}, \mathbf{r}')$ is the Oseen tensor:

$$H(\mathbf{r}, \mathbf{r}') = \frac{\Theta(|\mathbf{R}| - b)}{8\pi\eta\|\mathbf{R}\|^3} [\mathbf{I}\mathbf{R}^2 + \mathbf{R}\mathbf{R}^T] \quad (2.29)$$

where $\Theta(x)$ is the Heaviside function, b is the filament radius and $\mathbf{R} = \mathbf{r} - \mathbf{r}'$. With this formulation, the cutoff length is implemented directly in the definition of the tensor.

Decomposing the position \mathbf{r} on the modes of the biharmonic operator as done for Eq. (2.25) the equation of motion for the modes is

$$\partial_\tau \chi_n = \sum_l (H_{nl} + \delta_{nl}) \left[-\chi_l \frac{\gamma}{\tau_l} + \mathbf{f}_l \right] \quad (2.30)$$

where $D\phi_l = -1/\tau_l\phi_l$ and H_{nl} is the interaction matrix:

$$H_{nl} = \int_{-1/2}^{1/2} d\alpha d\alpha' \phi_0(\alpha) H(\mathbf{r}, \mathbf{r}') \phi_l(\alpha').$$

In the absence of hydrodynamic interactions, the modes do not mix and each mode relaxes with a unique relaxation time τ_n . Eq. (2.30) shows that the hydrodynamic matrix H_{nl} mixes the modes and their relaxation times. When the external force \mathbf{f} is uniform (as is the case of gravity), the force couples only to the zero-th mode because $\mathbf{f}_{l \neq 0} = 0$ – the coupling between higher modes and the external force is due to the hydrodynamic matrix. Since the 0 – th mode is the center of mass position, in the absence of long-range hydrodynamics, the filament simply translates along the gravitational field and the other modes relax with their unaltered characteristic time. In presence of hydrodynamics, instead, the filament bends upward [72] because the

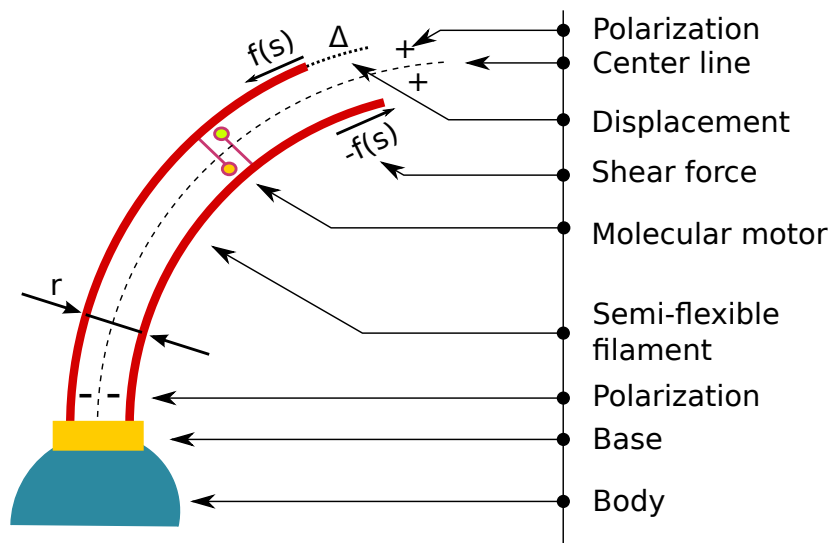


Figure 2.7.: Sketch of the 2D axoneme. The sliding filaments (red) are like two rails, at fixed distance r . The molecular motors are attached at one side, and pull the opposite filament towards the $+$ sign. The base (yellow) hinders the sliding, and connects the filaments to the sperm body.

hydrodynamic matrix couples the external uniform field to the higher modes that are, thus, excited.

2.5. Active Axonemes

The 9+2 structure of the axoneme hosts dynein motors between adjacent double-microtubules (Fig. 1.4, Fig. 2.4, and Fig. 2.7). Since the beating amplitude does not decrease, energy has to be provided throughout the flagellum length [37, 73]. It was soon realized that the sliding forces generated between the microtubules can indeed bend the filament and generate a traveling wave [37–39].

The question is, then, about the feedback mechanism between the filaments and the molecular motors. In the very first model a simple curvature-feedback between the viscous and elastic torques, and the active torques is proposed to model the beating pattern of sea urchin (see Refs. [30, 31, 37–39, 74, 75]). In the most recent developments the attention is turned to the actual mechanics that may generate the

traveling wave: proposed mechanism are the linear response function of molecular motors to the sliding velocity [44] or the interdoublets separation due to the bending [46]. In both cases, the underlying idea is to map the cylindrical arrangement of the axoneme to two planar and parallel filaments with shear forces in between (Fig. 2.7).

In Ref. [64] it is assumed that the free energy of two sliding semi-flexible filaments is

$$G = \int_0^L ds \frac{\kappa}{2} C^2 + f\Delta + \frac{\Lambda}{2} (\partial_s \mathbf{r})^2 \quad (2.31)$$

where κ is the bundle bending rigidity, $\Delta = \int_0^s ds' aC(s') + \Delta(0)$ is the relative sliding between the facing filament, f are the internal stresses, and λ is a Lagrange multiplier to constrain the filament length. The equation of motion of the filaments is, after Fourier transformation of time,

$$i\omega\xi_{\perp}\tilde{h} + \kappa\partial_s^4\tilde{h} - \sigma\partial_s^2\tilde{h} = r\partial_s\tilde{f} \quad (2.32)$$

where σ is the tangent stress at the first order in h and vanishes for clamped or fixed head and free tail, and for freely swimming sperm. The shear forces \tilde{f} are not known but it is argued that, near the Hopf bifurcation between relaxation dynamics and oscillatory dynamics, the details are not relevant and the shear force can be written as a linear relation between force and sliding $\tilde{f} = \chi\tilde{\Delta}$ where χ is the linear response-function of a (symmetric) two-state brownian-ratchet-like model of molecular motors [44, App. C] [76]:

$$\chi = K + i\lambda\omega - \rho\Omega k \frac{i\omega/\alpha + \omega^2/\alpha^2}{1 + \omega^2/\alpha^2} \quad (2.33)$$

and $\Delta \approx r(\partial_s h - \partial_s h|_0)$. The equation of motion is then:

$$i\omega\xi_{\perp}\tilde{h} + \kappa\partial_s^4\tilde{h} - \sigma\partial_s^2\tilde{h} = r^2\chi\partial_s^2h \quad (2.34)$$

and linear stability analysis shows that active traveling waves are, indeed, stable

solutions. The parameter Ω describes the concentration of ATP, or of Ca^{2+} when Calcium determines the motors activity, and α is a characteristic ATP cycling rate.

The proposed model does not suit the needs of complex bead-spring simulations, hence in chapter 6 we discuss a computational model based on the force-velocity equation obtained in Ref. [76] for two-state molecular motors model, and present an alternative model not bounded to a specific biomechanical hypothesis.

3. Models and Methods

3.1. Molecular dynamics simulations

We simulate filaments, like Actin or microtubules, and bundles, like the spermatozoon flagellum, as Worm-Like Chains. A filament of length L is composed of $N+1$ beads at distance $b = L/N$. The proper shape, elasticity and stiffness are modeled as internal forces between the beads. Every bead follows the law of classical mechanics:

$$\begin{aligned} \frac{d\mathbf{r}_i}{dt} &= \mathbf{v}_i \\ \frac{d\mathbf{v}_i}{dt} &= \mathbf{f}_i/m \quad \text{for } i \in [0, 1, \dots, N] \end{aligned} \quad (3.1)$$

where $\{\mathbf{r}_i, \mathbf{v}_i\}$ is the system configuration, m is the bead mass and $\mathbf{f}_i = \mathbf{f}_i(\{\mathbf{r}_i, \mathbf{v}_i\}, t)$ are the forces acting on the i -th bead.

In the following works we can identify two different classes of non-conservative forces: dissipative forces and active forces. The *active forces* may have different origins, in our case they are the torques that bend the filament to mimic the spermatozoon active beating. These forces can be seen also as energy sources. The dissipative forces originate from the interaction between the body and the fluid, and drain energy away from the system.

We investigate systems that are, essentially, inertialess: $d\mathbf{v}_i/dt \simeq 0$. Numerically, however, it is more convenient to integrate Eq. (3.1) (with inertia then), selecting a mass and viscous drag such that the inertial relaxation time-scale be the fastest time-scale involved: we choose $\gamma/m \approx 10^2$, where γ is a representative value of the viscous damping.

Once the forces (next subsection) and the integration scheme (following subsection) are specified, the equations of motion can be integrated.

3.1.1. Forces

To simulate an actively beating filament, four types of forces are present between the beads:

Bond forces Filaments are made of a constant fixed number of beads N , at distance b . The distance is constrained by a harmonic potential:

$$U_{\text{bond}} = \frac{k_b}{2} \sum_i^{N-1} (|\mathbf{r}_{i+1} - \mathbf{r}_i| - b)^2. \quad (3.2)$$

Bending forces adds stiffness to the chain of beads by constraining the angle θ_i between two consecutive bonds $\mathbf{R}_i = \mathbf{r}_{i+1} - \mathbf{r}_i$:

$$U_{\text{bending}} = \frac{\kappa}{2b^3} \sum_{i=0}^{N-2} (\mathbf{R}_{i+1} - \mathbf{R}_i)^2. \quad (3.3)$$

The forces on each monomer are computed via the usual variational principle:

$$-\mathbf{F}_i = \frac{\delta U_{\text{bending}}}{\delta \mathbf{r}_i} = \quad (3.4)$$

$$= \frac{\kappa}{2} \frac{\delta}{\delta \mathbf{r}_i} \sum_{j=i-2}^{i+2} (\mathbf{R}_{j+1} - \mathbf{R}_j)^2. \quad (3.5)$$

In the second line we highlighted that the force on each bead comes from 5 contributions, indeed [77]:

$$\mathbf{F}_i = \begin{cases} \mathbf{r}_{i\pm 2} - 4\mathbf{r}_{i\pm 1} + 6\mathbf{r}_i & \text{for } 2 < i < N - 3 \\ \mathbf{r}_{i\pm 2} - 2\mathbf{r}_{i\pm 1} + \mathbf{r}_i & \text{for } i = 0 \text{ and } i = N - 1 \\ \mathbf{r}_{i\pm 2} - 2\mathbf{r}_{i\mp 1} - 4\mathbf{r}_{i\pm 1} + 5\mathbf{r}_i & \text{for } i = 1 \text{ and } i = N - 2 \end{cases} \quad (3.6)$$

Bending torques mimic the internal forces/torques generated (e.g. by molecular motors) throughout the filament. In 2D simulations we can simulate the bending torque with a torque dipole between the nearest bonds of each bead (Fig. 3.1). Torque dipoles apply no net torques nor net forces, coherently with the real ones.

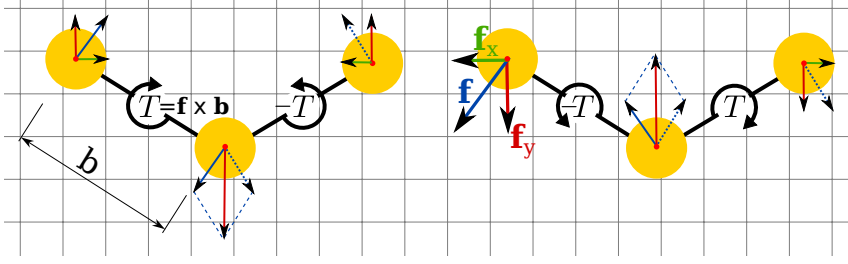


Figure 3.1.: Illustration of the implementation of the torque dipole.

Hydrodynamic interaction The hydrodynamic interaction can be modeled in different ways. In most cases, we are not interested in the computationally expensive direct integration of the Navier-Stokes equation and simplified approaches can be used. In previous works MPC[78] was used to reproduce the hydrodynamics at long scales and arbitrary boundary conditions [18, 79]. However, with the idea in mind to understand the minimum system, we use resistive force theory and slender body theory. The theoretical details are presented in the previous chapter, here we focus on the implementation:

Resistive-force theory Of the two techniques, this is the most straightforward.

The force on each bead depends on the local tangent and normal directions:

$$\mathbf{f}_i = - (\xi_{\perp} \hat{\mathbf{n}}_i \hat{\mathbf{n}}_i^T + \xi_{\parallel} \hat{\mathbf{t}}_i \hat{\mathbf{t}}_i^T) \mathbf{v}_i \quad (3.7)$$

At each bead the local tangent vector is $\hat{\mathbf{t}}_i = \mathbf{r}_{i+1,i-1}/|\mathbf{r}_{i+1,i-1}|$ where $\mathbf{r}_{i+1,i-1} = \mathbf{r}_{i+1} - \mathbf{r}_{i-1}$, the normal $\hat{\mathbf{n}}$ direction is the tangent vector rotated by $\pi/2$ CCW. At the filament end, the tangent is approximated by the bond direction.

The ratio between the two drag coefficients depends on the physical system (e.g. filament radius or wavelength). For spermatozoa we used the value measure in measured in Ref. [52] for swimming bull sperm near a substrate: $\xi_{\perp}/\xi_{\parallel} = 1.81$ and $\xi_{\parallel} = 0.69 \text{ fN}\mu\text{m}^{-2}\text{s}$.

Oseen tensor is implemented computing the background flow field \mathbf{u}_i in the position of bead i generated by all the other beads. The flow field is then

used to compute the effective drag force. The implementation is very similar to Eq. (2.8)[80]:

$$\begin{aligned} \mathbf{F}_i^{\mathbf{H}}(t) &= -\gamma_0 (\mathbf{v}_i - \mathbf{u}_i) \\ &= -\gamma_0 \left(\mathbf{v}_i + \frac{3}{4} \frac{a}{\gamma_0} \sum_{j \neq i} [\mathbb{1} + \hat{\mathbf{r}}_{ij} \hat{\mathbf{r}}_{ij}^{\mathbf{T}}] \frac{\mathbf{F}_j^{\mathbf{C}}}{r_{ij}} \right) \end{aligned} \quad (3.8)$$

where $\gamma_0 = 6\pi\eta a$ is the drag coefficient of a bead with radius a . The radius of the beads determines the aspect ratio of the filament. We used $a = b/2$, called Shish-Kebab model, fixing the aspect ratio to $1/(N - 1)$. Finally, note that the cutoff distance (δ in Eq. (2.9)) is determined by the bond length (here $\delta = b$).

3.2. Data Analysis

The theoretical investigation of microswimmers is bounded by our quantitative knowledge of the different observables. In the last 50 years of research we have seen a growing amount of detailed studies from the pioneeristic works of Gray and Hancock [5] till the latest manipulations by Pelle and Brokaw [48] and Friedrich and Jülicher [52].

Here we present some tools that we used to dissect the experimental recordings of a pinned spermatozoon. The problem can be stated as follows: “*How do we characterize and quantify the evolving shape of an organism?*” The problem is far from being restricted to the community of micro-swimmers. In general, the best experimental data of micro-organisms/cells is made of a high-resolution and high-framerate recording and we want to extract automatically, as much quantitative information as possible, and classify it in a meaning-full way. The original data being, essentially, just a collection of pixels.

In particular, we show how we adapted a technique used to study the behavior *C. Elegans* [81] called “Principal modes decomposition”, or “Whitening transformation” depending on the scientific community of origin.

The protocol we applied for the flagellum can be summarized as follows:

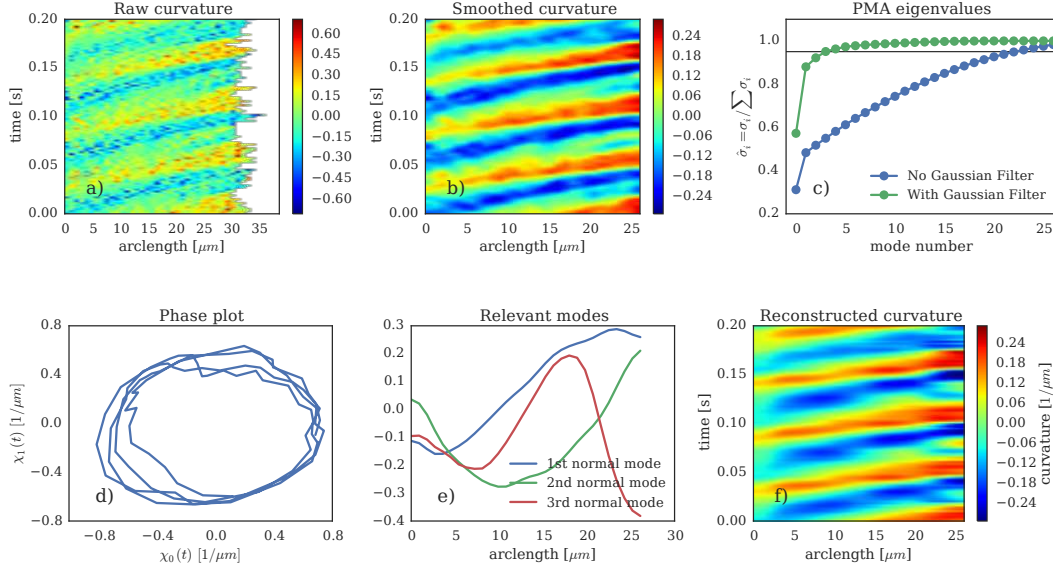


Figure 3.2.: The different passages involved in the analyses of the raw experimental data. From left to right, and top to bottom: From the tracked position of the flagellum $\mathbf{r}_i(t)$ we compute the curvature **(a)**, the curvature is cut to the last common point and filtered with a Gaussian kernel of width $\sigma = (1/500 \text{ s}, 0.9 \mu\text{m})$ **(b)**, the raw curvature is decomposed into the normal modes **(e)** and the importance of the modes is compared with respect to the modes of the filtered data **(c)**, plot of the “phase plot” of the amplitude of the first two modes **(d)**, and of the new curvature reconstructed from the first three normal modes only **(f)**.

1. The flagellum is tracked by $N(t)$ points by our collaborators. The number of points and the expected initial position of the flagellum change from frame to frame, but for all experiments the tracking initial point is at about $7\mu\text{m}$ from the pinning point and tracks the following $\approx 30\mu\text{m}$ down the flagellum.
2. We map the shape of the flagellum to its curvature. In this way we remove the informations about the position and orientation in the lab-frame. The curvature $C(i, t)$ at point $1 \leq i \leq N - 1$ is computed as [82]:

$$C(i, t) = 4 \frac{\Delta}{abc} \quad (3.9)$$

Where $a = |\mathbf{a}|$, $b = |\mathbf{b}|$, $c = |\mathbf{c}|$, $\Delta = \frac{1}{2} |\mathbf{a} \times \mathbf{b}|$, and

$$\mathbf{a} = \begin{pmatrix} x_{i-1} - x_i \\ y_{i-1} - y_i \end{pmatrix}, \quad \mathbf{b} = \begin{pmatrix} x_{i+1} - x_i \\ y_{i+1} - y_i \end{pmatrix}, \quad \mathbf{c} = \begin{pmatrix} x_{i+1} - x_{i-1} \\ y_{i+1} - y_{i-1} \end{pmatrix}.$$

In Fig. 3.2(a) we plotted the result of this operation. Observe that the curvature is very noisy and, as explained in the previous point, the number of points changes from frame to frame. In general it is possible select the region of arclength that is always tracked. In Fig. 3.2(b) we the curvature is also smoothed to compare the effect of a simple Gaussian filter to the results given by our protocol (panel f).

Of course, different ways to quantify a shape allow addressing different questions. For example: in the case of slender bodies, the curvature contains all the information about the organism shape, but its position and orientation in the space are lost, hence we should no infer informations about the motion of the body's center of mass. An alternative choice is the tangent angle, as in Ref. [81].

3. The auto-correlation matrix of the curvature is computed as

$$M(s, s') = \langle C(s, t)C(s', t) \rangle_t,$$

with eigenvalues σ_i and eigenvectors \hat{e}_i . The number of eigenvalues and eigenvectors is finite and discrete because the arclength s is discretized.

4. The eigenvalues σ_i are positive, because $M(s, s')$ is a correlation matrix and provide a measure of the amount of information encoded in the corresponding eigenvector. The eigenvectors are then sorted accordingly to their eigenvalue from bigger to smaller. In Fig, 3.2(c) we plotted the relative contribution of each mode $\hat{\sigma}_i = \sigma_i / \sum_j \sigma_j$ (see notes for an explanation of the difference between the two lines).
5. The interpretation of the physical meaning of the empirical modes is not trivial. Comparing of the relative contributions of each mode in the case of raw or

filtered curvature (pane c), we understand that higher modes can be seen as high frequency Fourier modes.

6. We expect/hope that the biological behavior is described by few modes. Interpreting high n modes as, essentially, high frequency mode, we find that the first 3 eigenvalues (Fig. 3.2(e)) describe more than 95% of the (biological) signal (panel c).

This is the case for most of the experiments that we analyzed (Fig. 3.4).

7. The eigenmodes are orthogonal and the input data can be projected on them to obtain the amplitude of the i -th modes $\chi_i(t)$ of each mode at time t : $\chi_i(t) = \int ds \hat{e}_i(s)C(s, t)$. This decomposition is similar, in spirit, to the method of the “separation of variables” used to solve certain PDEs.
8. In the case of periodic motion, there is a couple of equally important modes $\hat{e}_{1,2}(s)$ whose amplitudes are periodic in time with the frequency of the motion and in phase quadrature. If the modes $\hat{e}_i(s)$ themselves represent a sinusoidal-like function, the resulting superimposition represents a traveling wave. The plot of $\chi_1(t)$ vs $\chi_2(t)$ is called “phase plot” (Fig. 3.2(d)) and recalls the standard phase-reduction approach [83, 84].

We exploit this feature to measure the time-dependent frequency of the spermatozoon $\omega(t)$ with the resolution of one period using a Poincaré map[85].

9. From the first three modes and amplitudes we compute a filtered curvature that contains only the three chosen spatial modes, filtering away the irrelevant information (Fig. 3.2(f)): $C_{new}(s, t) = \sum_i^3 \chi_i(t)\hat{e}_i(s)$.

With this protocol we obtain then:

- Normal modes (Fig. 3.4(b and c))
- Frequency from Poincaré map (Fig. 3.2(d))
- Clear power spectrum (Fig. 3.3)

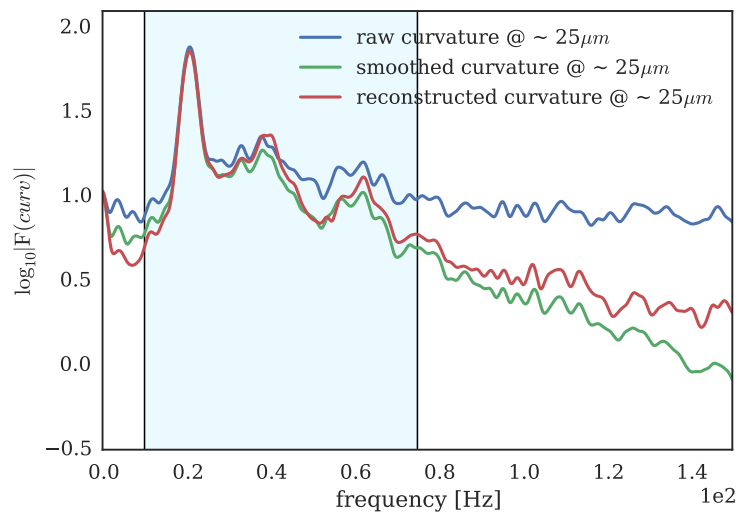


Figure 3.3.: Power spectrum of the curvature at $\sim 25\mu m$ of the flagellum of a beating sperm imaged at 500 fps. The three lines corresponds to the case of raw curvature, the smoothed curvature with Gaussian kernel of variance $1/500s$ and $0.9\mu m$ and, to them curvature computed from the first three normal modes. Observe that the peak of the second harmonic is much more clearly identified from the power-spectrum of the reconstructed curvature than of the smoothed data.

Note that the Gaussian filter applied to the curvature spreads the curvature from the tip to the base (as expected), but our protocol allows avoiding this artifact.

In Fig. 3.3 we show that this technique allows enhancing the relevant beating frequencies: comparing the power spectrum of the original raw curvature, the power spectrum of the filtered one and the power spectrum of the reconstructed we see that the red-line has a clearer second and third harmonic peaks than the green or blue ones.

3.2.1. Discussion

The technique we presented seems the ideal to decompose and analyze time series of moving micro-organisms. However, there are few side effects that must be kept in mind to avoid confusion.

Some observations stem from the physics behind the technique, and some from the biological context of application:

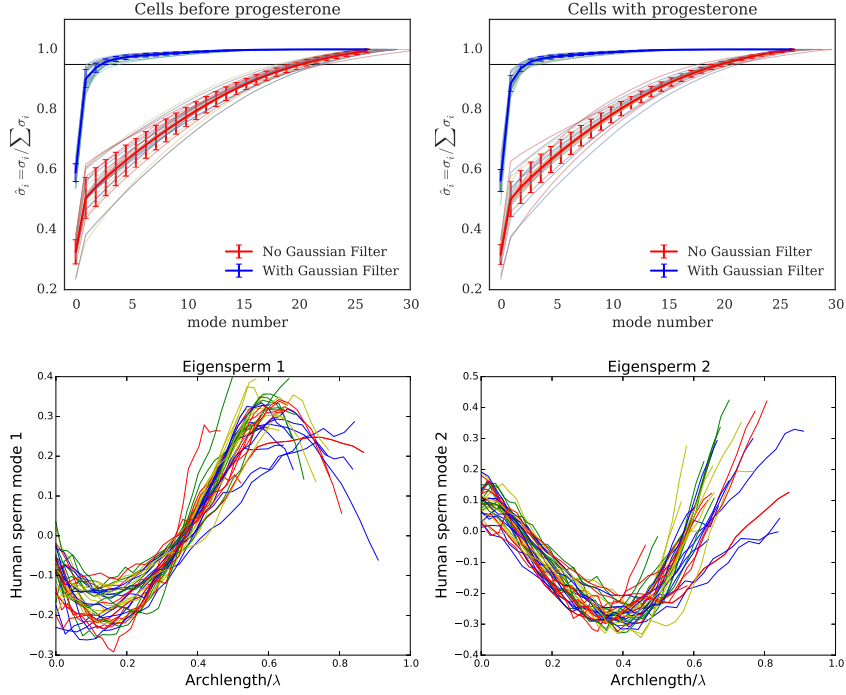


Figure 3.4.: **Top:** The two panels show the plot of $\hat{\sigma}_i$ in the case of raw and smoothed curvature (red and blue, respectively) and for normal cells and cells excited after the release of caged progesterone (**left** and **right**, respectively). Observe that the plots have a rather small variance: especially the blue lines show that in all the analyzed experiments three modes account for about 95% of the signal. **Bottom:** Plot of the first two eigenmodes $\hat{e}_i(s)$ for all experiments rescaled by the wavelength. Observe that, within the current precision, all sperms have, essentially, the same eigenmodes.

Phase between modes Because the flagellar beating is periodic the first two eigenmodes are, approximately, equally important. This means that the curvature can be approximated by the sum of two standing waves in phase quadrature: $C(s, t) \approx \chi_1 \hat{e}_1(s) \exp(i\omega t + i\psi) + \chi_2 \hat{e}_2(s) \exp(i\omega t + i\pi/2 + i\psi)$. The value of the phase ψ is arbitrary, and the protocol does not specifies it. This means that the output from different datasets may look different, even when the only real difference is the phase ψ . In Fig. 3.4(bottom), the phase is fitted to maximize the similarity to a reference mode, in this way we removed the degeneration.

In practice then, we know that three modes are enough to recover the important

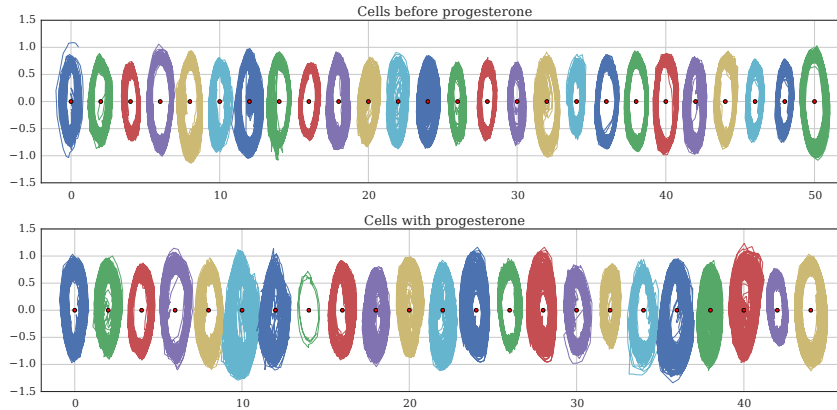


Figure 3.5.: Phase plot of the first two modes before and after the release of caged progesterone (**top** and **bottom**, respectively). The origin of each “cycle” is translated by 2 at every dataset, and the corresponding origin is indicated by the red dot. Note that, while many spermatozoa have a clear “limit cycle” around the origin associated to the beating modes, this is not the case for all of them.

part of the spatial structure of the input data, while the higher modes account only for finer spatial frequencies.

Behavior The correlation matrix $M(s, s') = \langle C(s, t)C(s', t) \rangle_t$ averages over the time window of the experiment as alternative to the ensemble average. The problem is that the system we are investigating is not ergodic.

The length of this window must be chosen appropriately: over long time-windows we should expect that the organism changes its behavior, while on short time-scales we observe the body conformations needed to move. In Ref. [81] a detailed account on the application of the technique to both behavioral and conformational studies is found.

3.3. Spectrogram

In many applications the Fourier transform alone is not enough to identify the important components of a signal. Sound analysis is one case in which the frequency

changes during time. The beating frequency, too, is not constant [86]¹: there are oscillations or fluctuations around a mean value, or drifts due to random noise, biological/chemical origin or other, still unknown, reasons.

In previous studies [87], the phase plot is used to determine the time dependent frequency from the phase velocity. This is not the recommended way [85] nor it is suitable to our data as many sperm cells have not a clear phase plot (Fig. 3.5). In particular, there is not always a clear limit cycle for the entire duration of the experiment.

One method to compute the time dependent frequency is the so-called “spectrogram”, that is intuitively simple: the power-spectrum is computed on a sliding window of size W . The time window W determines the FFT resolution (the wider W the better) and the spectrogram time resolution (the shorter W the better). An example can be seen in Fig. 5.8 with $W = 20$ periods.

3.4. Filament Modes

In chapter 4 we study the sedimentation of one, two and three filaments sedimenting in a viscous fluid. To characterize the numerically obtained filament conformations the shapes are projected on the normal modes ϕ_n to obtain the amplitude vector

$$\chi_n(t) = \int_{-L/2}^{L/2} ds \mathbf{r}(s, t) \phi_n(s). \quad (3.10)$$

Each component of the vector χ_n indicate the importance of the mode in Cartesian directions. For example, the mode amplitude $\chi_{2,z}$ of the 2nd mode, see Fig. 2.6, measures how much the filament is bent along the \hat{z} direction into a V -like shape and corresponds to the dominant term when a single filament sediments in a weak external field.

Note that the mode amplitudes are not invariant under transformations of the reference system. For rotating filaments, for example, we measure the out-of-plane

¹The frequency variance in a single *Chlamydomonas* is about 2 Hz, as we measure for human spermatozoa (Fig. 5.5).

3. Models and Methods

bending $\chi_{2,\perp}$ in the reference system of the filament as

$$\chi_{2,y} + i\chi_{2,x} = \chi_{2,\perp} \exp(i\omega t),$$

which also defines a rotation frequency ω in the “lab” reference system.

4. Conformations, hydrodynamic interactions, and instabilities of sedimenting semi-flexible filaments

In this chapter we present novel results on the sedimentation of semi-flexible filaments [88]. The methods are described chapter 3.

4.1. Introduction

Semi-flexible filaments are fundamental constituents of micro-biological systems, where microtubules and actin filaments serve as scaffolds for cellular structures and as routes to sustain and guide cellular transport systems [1]. Microtubules are also the main structural elements of cilia and sperm flagella, where their relative displacement and deformation due to motor proteins gives rise to the flagellar beat and hydrodynamic propulsion [44, 64]. Microtubules and flagella can be seen as elastic filaments interacting with their own flow field. The ability to visualize, assemble, and manipulate biological and artificial semi-flexible polymers [66, 89–91] poses new fundamental questions on the dynamics of filaments when elastic and hydrodynamic forces compete.

The dragging of stiff rods through a viscous fluid has been studied in detail [92]. A single rod does not reorient, but falls with its initial orientation. A more complex dynamical behavior can be expected and is indeed observed for semi-flexible filaments when the curvature or stretching elasticity competes with the hydrodynamic interactions [93–95]. Single dragged semi-flexible filaments bend into a shallow V shape to balance the higher drag at both ends [72] and their end-to-end vector aligns

perpendicularly to the external field [95]. For strong drag, higher modes have been found to be excited after turning on the field; this generates W -shapes initially, which then relax back into horseshoe-like U shapes [72]. Here, the dynamics seems to be constrained to the plane initially defined by the direction of the external field and the filament itself. However, these investigations address the problem from a deterministic point of view, and little attention has been paid to the dynamic stability of the resulting shapes. In all cases, the dragged and deformed semi-flexible filament initially defines the settling plane, but the stability of the filament's planar shape has not been investigated as function of the external field or the relative position of possible neighboring filaments.

Here, we focus on the full three-dimensional shape of one, two, and three semi-flexible filaments sedimenting in a homogeneous external field. We incorporate the hydrodynamics into the equations of motion for the filament shape via the Oseen tensor, valid in the limit of zero Reynolds number. As a result of our numerical and analytical analysis, we find that the deformations confined to a plane become unstable with respect to normal perturbations at a threshold value B_1^* of the strength B of the external field, which is *smaller* than the threshold B_2^* where initial, transient W shapes become excited, see Fig. 4.1. Thus, with increasing strength of the external field, two instabilities and transitions to new sedimentation modes are predicted. The first transition is from a stable planar U -shape with little bending to a stationary horseshoe-like U -shape with out-of-plane bending. The second transition at stronger fields excites a metastable W shape, also with out-of-plane bending, which then “relaxes” into a non-stationary asymmetric U -shape. As result, there exist two families of shapes, where the elastic forces are balanced by a conformation-dependent drag.

We consider next the interaction between two filaments in an external field. Indeed, while the dynamics of an isolated filament is an indispensable knowledge needed to understand the case of $n > 1$ interacting filaments, many situations are characterized by elastic slender objects interacting via the generated flow field: cilia [35, 91], sperm [17, 23], and *E. Coli* bundles [6, 96] are probably the most relevant from a biological point of view.

It is known that the sedimentation behavior of colloids can be quite complex.

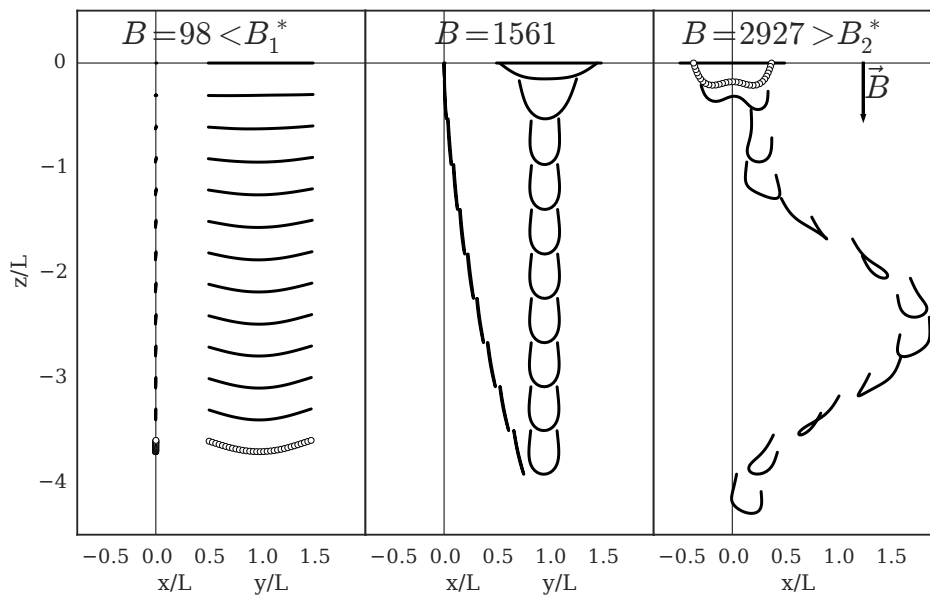


Figure 4.1.: Snapshots from simulations of single filaments dragged by the external homogeneous field $B = mgL^2/\kappa$, where L is the filament length, g the external field, and κ the bending stiffness. **Left:** For weak field ($B < B_1^*$) the filament bends into a V-shape (in dots), dominated by the $\chi_{2,z}$ mode. **Center:** As the field strength increases, higher modes with an out-of-plane component are excited, and the filament drifts sideways. **Right:** For even stronger fields ($B > B_2^*$) further symmetries are spontaneously broken, and the filament rotates following a helical trajectory.

The interaction of sedimenting particles has been studied in considerable detail for spherical colloids [97, 98]. Two particles sediment together, but don't follow the direction of the external field, and move instead under an angle with respect to it. For more particles, many different dynamical behaviors can be found, in particular periodic motions where particles “dance” around each other [98].

For dragged semi-flexible filaments, the dynamical behavior is even more complex [94]. In particular, we show that two filaments (Fig. 4.1) attract each other, repel each other, or spin around the field depending on the intensity of the external field.

We focus here on the stability of the sedimentation plane for different field intensities and on the origin of the relative velocity. In particular, we want to see whether the velocity difference is due to different shapes or to the broken up-down symmetry. For even more filaments, the dynamics become unsteady at much weaker external field strength than expected from the two-filaments case.

4.2. Results

4.2.1. Deformation and Dynamics of Single Filament

The filament is initially oriented along the x axis of the reference frame. After a certain time, the dragged filament reaches a stationary shape and velocity. Examples of conformational sequences for various field strengths are displayed in Fig. 4.1. We characterize the shapes via Eq. (3.10) in terms of the mode amplitudes. In Fig. 4.2, the most important stationary amplitudes are presented. Below a critical field $B_1^* \simeq 1200$, the filament shape is governed by planar modes (green and black lines), where $\chi_{2,z}$ dominates and, thus, the characteristic V -shape appears.

In simulations restricted to a two-dimensional plane, or in three-dimensional simulations without noise [72], the filament dynamics is localized in the xz plane and filaments bend into a planar W -shape for fields $B > B_2^* \approx 1800$. In contrast, in our three-dimensional simulations with weak noise, we find that the planar filament conformations are metastable for $B_1^* < B < B_2^*$, and also modes along the y axis are excited. We characterize the out-of-plane filament shape and dynamics by the mode

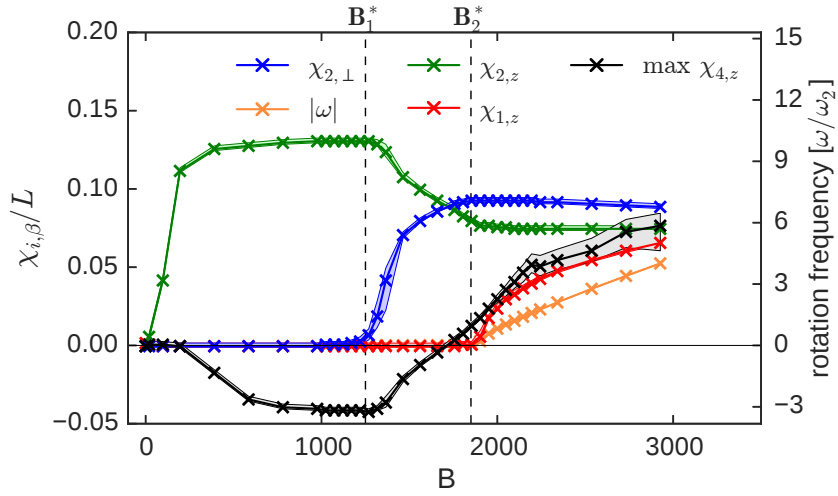


Figure 4.2.: Stationary mode amplitudes of a single semi-flexible filament as function of the external field B . The shaded areas indicate the 66% confidence interval. When $B < B_1^*$, only planar modes are excited, and the filament stays in the plane defined by its initial orientation and the orientation of the applied field, here the xz plane. For $B > B_1^*$, an out-of-plane mode $\chi_{2,\perp}$ is excited. For $B > B_2^*$, the out-of-plane component $\chi_{2,\perp}$, the bending component $\chi_{2,z}$ saturates, and the amplitude $\chi_{4,z}$ becomes important (visualized in Fig. 4.1). In black crosses indicate the maximum value of $\chi_{4,z}$ before it decays. The resulting shape is asymmetric and spirals around the z axis with frequency ω/ω_2 (light-blue symbols), with ω_2 the frequency of the second mode (Eq. (4.1)).

amplitude $\chi_{2,\perp}(t)$, where

$$\chi_{2,\perp}(t) = \chi_{2,x}(t) + i\chi_{2,y}(t) = |\chi_{2,\perp}|e^{i\omega t}. \quad (4.1)$$

In the stationary state, an U shaped and deck-chair-like conformation is assumed with out-of-plane bending (Fig. 4.1). The filament orientation is fixed and $\chi_{2,\perp} = \chi_{2,y}$ (blue line in Fig. 4.2). Since its shape is asymmetric, the filament drifts sideways while settling in the external field.

When $B \gtrsim B_2^*$, the mode $\chi_{4,z}$ becomes important at early times, leading to a temporary W shape (Fig. 4.2). The trajectory for $B \simeq 3000$, displayed in Fig. 4.1, shows the initial W , which later turns into an asymmetric U shape, in which one arm is longer than the other. The appearing shape is stable; however, because of its asymmetry, the mode amplitude $\chi_{1,z}$ is non-zero and the filament rotates around the z axis with frequency ω , see Fig. 4.2 (light-blue line), which we determined via Eq. (4.1).

In contrast, in the deterministic dynamics of previous studies [72], the W shape was found to decay only into the stable and symmetric planar horseshoe shape.

4.2.2. Conformations and Dynamics of Two Interacting Filaments

Relative Velocity of two Filaments

For an analytical description of interacting filament, we adopt a continuum model. The equation of motion of the point $\mathbf{r}^\nu(s, t)$ ($-L/2 \leq s \leq L/2$) along the contour of filament ν is given by [67]

$$\partial_t \mathbf{r}^\nu(s, t) = \sum_\mu \int_{-L/2}^{L/2} ds' \mathbf{H}(\mathbf{r}^\nu(s) - \mathbf{r}^\mu(s')) \mathbf{f}^\mu(s'), \quad (4.2)$$

where \mathbf{f}^μ is the external force density and the index ν indicates the various filaments. As before, the hydrodynamic tensor $\mathbf{H}(\mathbf{r}^\nu(s) - \mathbf{r}^\mu(s'))$ comprises the Oseen tensor and the local friction. The force density \mathbf{f} comprises bond, bending, and gravitational

forces. In the limit of a rather stiff filament, it can be written as

$$\mathbf{f}^\nu(s) = l_p k_B T \left(\frac{1}{l_p^2} \frac{\partial^2}{\partial s^2} - \frac{\partial^4}{\partial s^4} \right) \mathbf{r}^\nu(s) + \mathbf{f}_G^\nu(s), \quad (4.3)$$

with the persistence length l_p [68, 99]. In the following, we will neglect the bond term, i.e., the term with the second derivative and focus on bending stiffness only.

As described in Sect. 2.3, the expansion

$$\mathbf{r}^\nu(s, t) = \sum_{n=0}^{\infty} \boldsymbol{\chi}_n^\nu(t) \phi_n(s) \quad (4.4)$$

in terms of the eigenfunctions ϕ_n of the biharmonic operator leads to the equations of motion for the mode amplitudes

$$\partial_t \boldsymbol{\chi}_n^\nu = \sum_{\mu} \sum_{l=0}^{\infty} \mathbf{H}_{nl}^{\nu\mu} \left[-\frac{\gamma}{\tau_l} \boldsymbol{\chi}_l^\mu(t) + \mathbf{f}_{lG}^\mu \right]. \quad (4.5)$$

The matrix representation of the hydrodynamic tensor is

$$\mathbf{H}_{nl}^{\nu\mu} = \int_{-L/2}^{L/2} ds ds' \phi_n(s) \mathbf{H}(\mathbf{r}^\nu(s), \mathbf{r}^\mu(s')) \phi_l(s'). \quad (4.6)$$

We derive now an equation for the relative velocity between the centers of mass of two filaments. We restrict our analysis to the case of small bending amplitudes, that is equivalent to consider small external fields, and filaments of identical shape.

Since $\int_{-L/2}^{L/2} \phi_n(s) ds = \sqrt{L} \delta_{n,0}$ for the exact eigenfunctions, the difference in the center-of-mass velocity $\Delta \mathbf{v}_{cm} = \mathbf{v}_{cm}^1 - \mathbf{v}_{cm}^2$ of two isolated filaments is given by

$$\begin{aligned} \Delta \mathbf{v}_{cm} &= \frac{1}{L} \int_{-L/2}^{L/2} ds \partial_t [\mathbf{r}^1(s, t) - \mathbf{r}^2(s, t)] \\ &= \frac{1}{\sqrt{L}} \partial_t [\boldsymbol{\chi}_0^1(t) - \boldsymbol{\chi}_0^2(t)]. \end{aligned} \quad (4.7)$$

4. Sedimenting Filaments

Substitution of Eq. (4.5) yields

$$\begin{aligned} \sqrt{L}\Delta\mathbf{v}_{cm} = & \sum_n \mathbf{H}_{0n}^{11} \left[-\frac{\gamma}{\tau_n} \boldsymbol{\chi}_n^1 + \mathbf{f}_{nG}^1 \right] - \sum_n \mathbf{H}_{0n}^{22} \left[-\frac{\gamma}{\tau_n} \boldsymbol{\chi}_n^2 + \mathbf{f}_{nG}^2 \right] \\ & + \sum_n \mathbf{H}_{0n}^{12} \left[-\frac{\gamma}{\tau_n} \boldsymbol{\chi}_n^2 + \mathbf{f}_{nG}^2 \right] - \sum_n \mathbf{H}_{0n}^{21} \left[-\frac{\gamma}{\tau_n} \boldsymbol{\chi}_n^1 + \mathbf{f}_{nG}^1 \right]. \end{aligned}$$

The first two terms on the right-hand side account for self-interactions of the individual filaments, the other two terms of the hydrodynamic interactions between the filaments.

We simplify our considerations by assuming identical shapes of the filaments, i.e., we set $\boldsymbol{\chi}_n^1 = \boldsymbol{\chi}_n^2 := \boldsymbol{\chi}_n$. Moreover, for the constant external force the relation applies $\mathbf{f}_{nG}^\nu = \mathbf{f}_{0G}^\nu \delta_{0n}$ independent of the particular filament. Hence, its contribution vanishes, which yields

$$\Delta\mathbf{v}_{cm} = \frac{1}{\sqrt{L}} \sum_{n=1}^{\infty} (\mathbf{H}_{0n}^{21} - \mathbf{H}_{0n}^{12}) \frac{\gamma}{\tau_n} \boldsymbol{\chi}_n. \quad (4.8)$$

We are primarily interested in the distance dependence of the relative center-of-mass velocity. Hence, we additionally neglect the dyadic term in the hydrodynamic tensor (2.29). Moreover, the local friction term vanishes in Eq. (4.8), and the hydrodynamic tensor can be written as

$$\mathbf{H}_{0n}^{\nu\mu} = \frac{1}{8\pi\eta} \int_{-L/2}^{L/2} \frac{\phi_n(s)\phi_0(s')}{|\mathbf{r}^\nu(s) - \mathbf{r}^\mu(s')|} ds ds'. \quad (4.9)$$

Using the eigenfunction expansion Eq. (4.4), we obtain

$$\begin{aligned} \mathbf{r}^\nu(s) - \mathbf{r}^\mu(s') &= \Delta\mathbf{r}_{cm}^{\nu\mu} + \sum_{n=1}^{\infty} \boldsymbol{\chi}_n (\phi_n(s) - \phi_n(s')) \\ &= \Delta\mathbf{r}_{cm}^{\nu\mu} + \boldsymbol{\Xi}(s, s'). \end{aligned} \quad (4.10)$$

With this definition, we obtain for $\Delta\mathbf{H}_{0n}^{12} = \mathbf{H}_{0n}^{21} - \mathbf{H}_{0n}^{12}$

$$\begin{aligned} \Delta\mathbf{H}_{0n}^{12} &= \frac{1}{8\pi\eta} \int_{-L/2}^{L/2} ds ds' \phi_n(s) \phi_0(s') \\ &\times \left[\frac{1}{|\Delta\mathbf{r}_{cm}^{21} - \boldsymbol{\Xi}(s, s')|} - \frac{1}{|\Delta\mathbf{r}_{cm}^{21} + \boldsymbol{\Xi}(s, s')|} \right]. \end{aligned} \quad (4.11)$$

In the limit $d = |\Delta\mathbf{r}_{cm}^{21}| \gg |\boldsymbol{\Xi}(s, s')|$, Taylor expansion yields

$$\Delta\mathbf{H}_{0n}^{12} = \frac{1}{4\pi\eta} \int_{-L/2}^{L/2} ds ds' \phi_n(s) \frac{\boldsymbol{\Xi}(s, s') \cdot \Delta\mathbf{r}_{cm}^{21}}{d^3} \phi_0(s'), \quad (4.12)$$

and hence,

$$\begin{aligned} \Delta\mathbf{v}_{cm} &= \frac{1}{4\pi\eta\sqrt{L}} \frac{1}{d^2} \\ &\times \sum_{n=1}^{\infty} \frac{\gamma}{\tau_n} \boldsymbol{\chi}_n \int_{-L/2}^{L/2} ds ds' \phi_n(s) \frac{\boldsymbol{\Xi}(s, s') \cdot \Delta\mathbf{r}_{cm}^{21}}{d} \phi_0(s'). \end{aligned} \quad (4.13)$$

Substituting $x = s/L$ and setting $\gamma = 3\pi\eta$ [67], yields

$$\begin{aligned} \Delta\mathbf{v}_{cm} &= \frac{3}{4} \frac{L^2}{d^2} \\ &\times \sum_{n=1}^{\infty} \frac{1}{\tau_n} \frac{\boldsymbol{\chi}_n}{\sqrt{L}} \int_{-1/2}^{1/2} dx dx' \phi_n(x) \frac{\boldsymbol{\Xi}(x, x') \cdot \Delta\mathbf{r}_{cm}^{21}}{d} \phi_0(x'). \end{aligned} \quad (4.14)$$

Thus, the relative velocity decreases quadratically with the distance between the filaments. There is evidently no velocity difference when $\Delta\mathbf{r}_{cm}^{21}$ is perpendicular to $\boldsymbol{\Xi}(s, s')$. In particular, there is no force between two specifically aligned rods as long as their director $\boldsymbol{\chi}_1$ is perpendicular to $\Delta\mathbf{r}_{cm}^{21}$.

Weak Field - Relative Velocity

As shown in Sec. 4.2.1, the stationary shape of a single filament in weak fields $B < B_1^*$ is of V -shape, which breaks the bottom-top symmetry. This is sufficient to generate an effective attraction between sedimenting filaments with the same shape. To characterize this interaction, we compute the relative velocity Δv between the

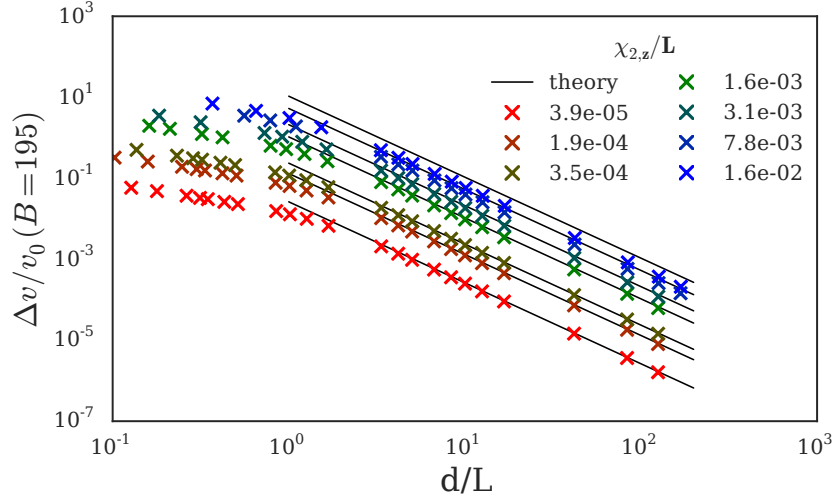


Figure 4.3.: Simulations of two filaments with the same imposed shape, kept constant during the simulation ($B = 195$). The shapes are created with the given $\chi_{2,z}$. The filaments lie in the same plane, parallel to the external field. The relative velocity Δv scales as d^{-2} . The black lines correspond to the prediction of Eq. (4.16), save for a common factor $\delta \approx 1.03 \times 10^{-6}$. The theory describes correctly the trend on d , and the trend on $\chi_{2,z}$ holds up to $\chi_{2,z} = 8 \times 10^{-3}$.

centers of mass of two filaments of equal shape along the sedimentation direction. The filaments remain localized in the xz plane and are separated by a distance d . As shown in Fig. 4.3, the relative velocities exhibit a significant dependence on the filament separation. We especially find that $\Delta v \sim d^{-2}$ for distances larger than the filament length.

For the considered filament geometry,

$$\mathbf{r}^1(s, t) = (\chi_{1,x}(t)\phi_1(s), 0, \chi_{2,z}\phi_2(s))^T \quad (4.15)$$

and $\mathbf{r}^2(s, t) = \mathbf{r}^1(s, t) + d\mathbf{e}_z$, the general expression for the velocity difference (Eq. 4.14) yields

$$\Delta v_{cm} \sim \chi_{2,z}^2 \frac{L^2}{d^2} \quad (4.16)$$

in the limit $d \rightarrow \infty$. Evidently, the filaments attract each other due to the top-bottom

asymmetry of their shapes. In the simulations, the filament shapes are determined initially by imposing the amplitude $\chi_{2,z}$, which is then kept fixed. The simulation results of Fig. 4.3 are in agreement with our theoretical prediction down to roughly the filament length. The d^{-2} power law is indeed a universal scaling, unaffected by the filaments shape and external field. The dependence of Δv on $\chi_{2,z}$ (Eq. (4.16)) is also verified for very small bending.

Weak Field – Stability

We now relax the imposed shape constraint and consider collective effects for two filaments, which are initially straight, oriented along the x axis and displaced along the z axis by a distance d (cf. Fig. 4.4(a)). For easier comparison with Ref. [72, 94], we employ the dimensionless number $\Delta = (A_{\text{upper}} - A_{\text{lower}})/(L/2)$ to quantify the bending asymmetry, where $A_{\text{upper, lower}}$ is the total z extension of the upper/lower filament. As indicated in Fig. 4.5, the filament curvature changes with time and the upper filament is bent stronger than the lower one. Figures 4.5 (a),(b), show the curvature asymmetries Δ and the relative velocities for various external field strengths. Δ decreases with increasing distance d , indicating more similar shapes at larger distances. Hydrodynamic interactions lead to an attraction of the two filaments ($v_{\text{upper}} > v_{\text{lower}}$), in agreement with the imposed-shape approximation studies of the last section. Indeed, the constant-shape approximation still gives the correct $(L/d)^2$ power-law dependence for $d/L \gg 1$, while the magnitude of the deformation, $\chi_{2,z}^{(eff)}$, has to be fitted. When the filaments approach each other, the generated flow field depends on the details of their shapes that, in turn, depends on the external field, hence we expect a non-universal behavior. Note that in contrast to Ref. [94], we find that the *upper* filament bends more than the lower filament (see also Fig. 4.4).

The planar configuration of a filament is also stable with respect to filament rotations around the field axis, see Fig. 4.4 (b). Filaments that are initially displaced along the z axis (as in the previous case) and rotated with relative orientation angle θ around the external field axis spin until the relative angle vanishes, as illustrated by Fig. 4.5 (c). Also in this case, the *upper* filament drifts and rotates faster than the lower one, see Fig. 4.5 (d). The relative velocity is essentially the same as in the

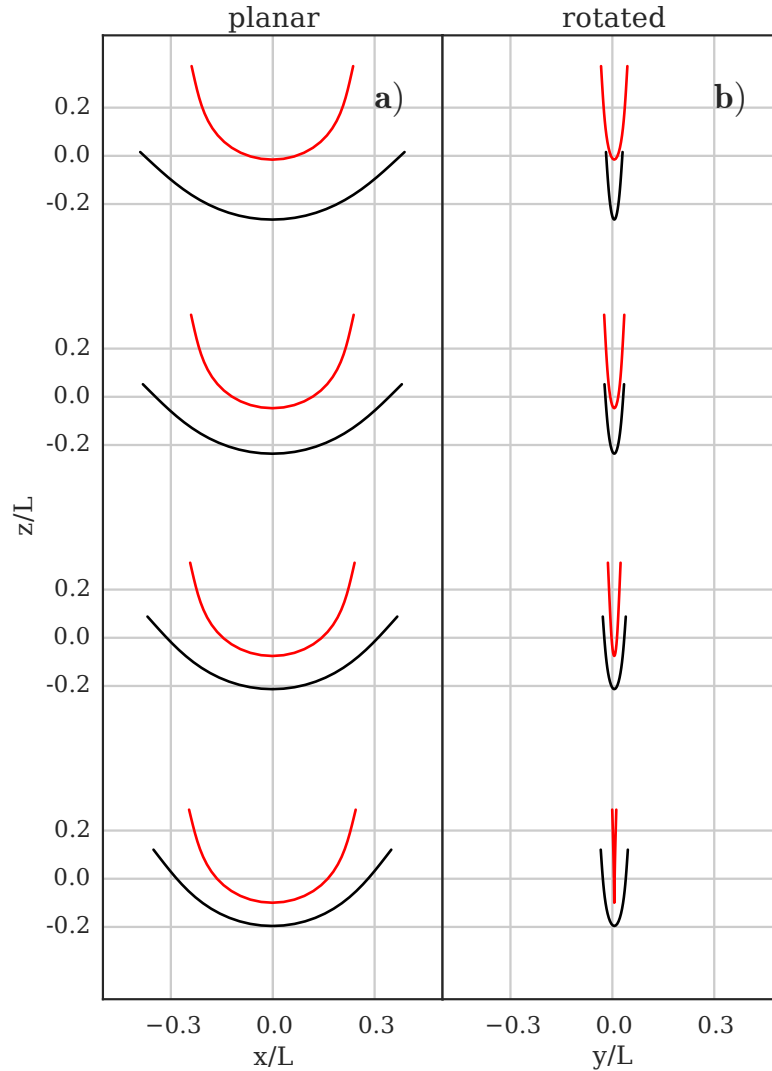


Figure 4.4.: Snapshots of two-filament conformations for $B = 195$, in time intervals Δt . **(a)** Co-planar sedimentation. Note that the upper filament is more bent than the lower filament, and $d_{min}/L = 0.13$. Axes to scale, z position translated. **(b)** The two filaments approach each other after initialization in a rotated configuration. Both filaments spin around the z axis, with the upper filament spinning faster (Fig. 4.5 (c-d)).

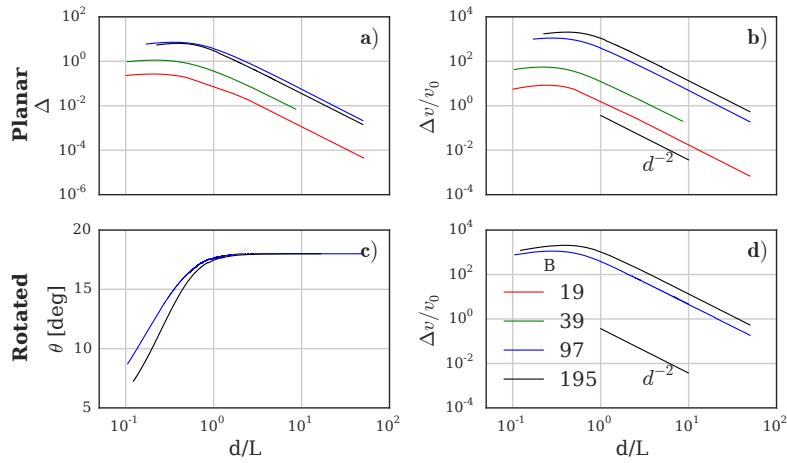


Figure 4.5.: a)-b) Bending asymmetry Δ and relative velocity Δv of two filaments as function of the filaments distance for $L/b = 30$. The two filaments are in the same plane, parallel to the external field and parallel to each other. Each color corresponds to a different external field B , as indicated. The velocity v_0 is the terminal velocity given by the resistive force theory for a rod. When $d/L \gg 1$, the relative velocity scales as d^{-2} . Note that filaments attract, i.e. time progresses from right to left. c)-d) Rotation angle θ and relative velocity Δv of two initially rotated filaments around the field axis by $\theta = 18^\circ$. The relative velocity is essentially unaffected by this change. Notably, the filaments spin toward each other decreasing the relative angle.

planar case.

Thus, two filaments sedimenting in weak fields relax toward a stable planar configuration one behind the other. The shape of the filaments is dominated by the second mode, pointing downwards, as shown in Fig. 4.4. This mode dominates and it breaks the mirror symmetry of the hydrodynamic interactions even for filaments of the same shape. Note that, in contrast to the single filament case, the system does not reach a stationary state velocity or shape, since the upper filament is always faster than the lower filament until the filaments touch each other.

Strong Field

For strong fields, we consider two filaments, which are initially displaced by $6L$ along the field direction. We measure the shape eigenvalues when the distance is $5L$, in the quasi-stationary regime, and find that the eigenvalues exhibit the same behavior as those of a single filament. This means that for $B > B_1^*$ the dynamics of each filament is dominated by the local flow field and not by the interactions with the other filament. Indeed, we find no correlations between the orientations of the out-of-plane components of the two filaments for $B > B_1^*$: the two filaments can by chance bend out-of-plane and drift in arbitrary directions.

When $B > B_2^*$, the filaments undergo the same transitions as a single filament: each of them reaches the same stationary shape and rotation velocity as an isolated filament. We find no correlations between the rotation directions of the two filaments: some filaments spin in the same direction, others in opposite directions, with no preference. This highlights the relevance of hydrodynamic interactions between two filaments for external fields weaker than B_1^* . Stronger fields reduce the effects of hydrodynamic interactions and the emergent behavior is the same as that of an isolated filament.

4.2.3. Three Filaments

Given the complex dynamics of two interacting filaments, it is interesting to consider also the collective behavior of several filaments. We find in simulations of systems with more than two filaments an intriguing collective dynamic behavior even for very

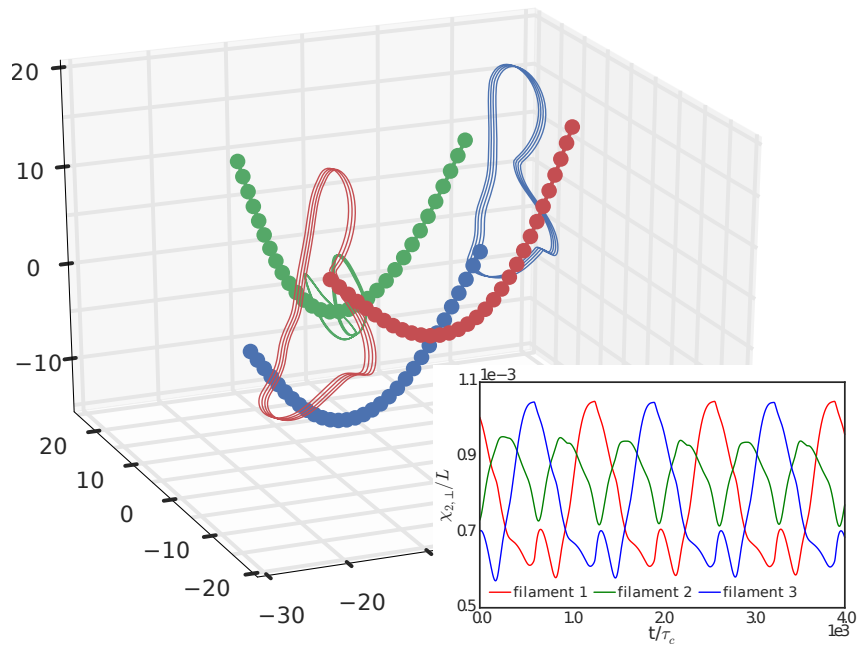


Figure 4.6.: Three semi-flexible filaments and trajectory of one bead (thick line), for the external field $B \simeq 60 \ll B_1^*$. In this case, the filaments form a bundle, but the relative positions change periodically. **Inset:** plot of $\chi_{2,z}$ for the three filaments. Since they have the same period and constant phase shift, this is the result of a cooperative behavior.

weak fields ($B \simeq 60$) and in the absence of noise.

We focus here on the case of three filaments, see Fig. 4.6. For most (randomly chosen) initial configurations, the nearest two filaments form a bundle that settles faster than the third filament that is then left behind. However, we find also some initial configurations where all three filaments attract each other and form a bundle. In this case, the relative positions are not stationary; instead, the filaments follow a periodic trajectory, see Fig. 4.6 (inset). In the inset of Fig. 4.6, we show also that the shapes of the three filaments are not stationary. The mode amplitude $\chi_{2,z}$ of each filament changes periodically, with a constant phase shift between them.

Our results for one and two filaments indicate that triggering of a time-periodic bifurcation requires strong fields. However, the three-filaments results suggest that systems with more filaments display a very complex dynamics even for weak fields due to complex hydrodynamic interactions.

4.3. Discussion and Conclusions

We have investigated the dynamics and stability of semi-flexible filaments exposed to an external homogeneous field and interacting only via hydrodynamic fluid fields. Due to the competition between hydrodynamic interactions and bending stiffness, the appearing dynamical behavior is richer than for entropy-dominated polymers or interacting rods.

We have shown that, for weak fields $B < B_1^*$, co-planar configurations of two filaments are stable upon perturbations that rotate the shapes relative to each other around the field axis. With simulations of fixed shape filaments, we have highlighted that a V - or U -shape is sufficient to break the hydrodynamic symmetry at low Reynolds numbers, leading to a relative velocity that scales with distance as $(L/d)^2$. Hence, the difference in drag coefficients between filaments is not necessary to explain the faster settling velocity of the upper filament.

For external field strengths exceeding the critical value B_1^* , the hydrodynamic interactions bend the filament out of its principal plane. Simulations of a single bent filament show that the hydrodynamic forces balance the elastic force, stabilizing

the out-of-plane shape. The resulting trajectory is a drift in the direction of out-of-plane bending, superimposed to the settling motion. This is a novel result, not to be confused with the previously reported metastable W -state [72] that is excited when $B > B_2^*$. A careful analysis of the eigenmodes indicates that the decay of the metastable state does not, in general, lead to the reported planar horseshoe shape, but also excites an average rotation mode with respect to the field axis ($\chi_{1,z}$) and our out-of-plane bending mode $\chi_{2,\perp}$. The filaments spin then around the field axis.

Finally, we have demonstrated that three filaments display an unexpected periodic dynamics even at field strengths far weaker than B_1^* . This is in contrast to the dynamics of a pair of filaments that either displays a monotonic dynamics that relaxes the attractive force (when B is weak) or a dynamics dominated by the single-filament (when $B > B_1^*$).

The interesting external fields B are in the range $10^1 \lesssim B \lesssim 10^4$. We can estimate these parameters for biopolymers like actin or microtubules. Actin has a persistence length of $l_p \simeq 17\mu m$, an average length $L \simeq 20\mu m$, and the bending rigidity $\kappa \simeq 60 \times 10^{-3} pN\mu m^2$ [1]. The external gravitational field, corrected for buoyancy, is about $G \approx 10^{-7} \frac{pN}{\mu m}$, which implies $B_{gravity} \simeq 10^{-2}$. Microtubules, on the other hand, are stiffer, longer, and heavier with $l_p \sim 1mm$, $L \sim 100\mu m \ll l_p$ and $G \approx 10^{-6} \frac{pN}{\mu m}$ [57]. This yields the effective field strength $B_{gravity} \simeq 10^{-1}$. An experimental test of our predictions is therefore within reach of modern centrifuges with accelerations of about 10^3g .

5. Flagellar Beat of Pinned Human Sperm

The hydrodynamic interaction between spermatozoa is due to the flow generated by the motion of their body, similarly to the interaction between semi-flexible filaments studied in the previous chapter: the main difference, in this case, is that the flow field is generated by the active beating pattern of the flagellum and not by the passive relaxation of the filament to the external forces. Therefore, a quantitative understanding of the beating pattern of spermatozoa is of primary relevance to design models that reproduce the flow field and give some insight in the spermatozoa coordination (cf. also Refs [18, 19]).

Here we present the analysis of the experimental recording of pinned human sperm (in collaboration with research center CAESAR, Bonn). The sperm cells, as most microswimmers, are known to be attracted to surfaces. The experimental setup uses this feature to fix the sperm cell within the microscope field-of-view. In the particular experimental setup we are interested in, the spermatozoa get incidentally pinned as it swims over a selected functionalized area. Movies at 500 fps record continuously 7 s to ≈ 3 minutes, corresponding to 10^2 to 5×10^3 beating cycles, and the flagellum is tracked. In the following the tracking mesh has a resolution of $0.9 \mu\text{m}$. In Fig. 5.1 we show one frame (inverted colors) which is overlaid with the (red) tracking and the corresponding simulation (blue). The shaded lines correspond to past frames, and the dashed lines to the average flagellum shape. The observation of the experimental data alone gives information about the kinematics of the beating (as in Ref [52]) but no informations about its dynamics.

Here, we intend to devise also a model that can reproduce the experimental beating pattern by simulating the flagellum as a semiflexible filament and imposing an

appropriate bending torque. To this end, we need to define a set of observables that trustfully represent the beating pattern: we found that the best options are the frequency ω and the first two normal modes of the curvature \hat{e}_1 and \hat{e}_2 . The model represents the spermatozoon body and flagellum as a semi-flexible filament, activated by local bending torques, as described in the chapter 3. By carefully matching the simulated and experimental geometry we propose that, despite the evident nonlinearities and asymmetries of the real beating (Fig. 5.1), the bending torques have the simple, inviting, form of a traveling wave.

In the process of developing the model, we realized that all sperms in our dataset rotate around their pinning point (Figs. 5.9 and 5.11). It is known that sperms swim in circles, probably to enhance the chemotactic mechanism [100, 101], hence the rotation itself is not a surprise. One proposed mechanism is that the rotation be caused by the average curvature of the flagellum [52, 100] or a bent neck [102]. We find that another, new, mechanism is possible. In the analysis of the power spectrum of the beating frequency it is common to observe higher harmonic peaks. We show analytically that higher harmonics contributions lead to a net torque around the pinning point, that is compatible with the simulations driven by torques with two harmonics and the experimental data. We highlight that the average curvature can be a byproduct of higher harmonics, and need not to be present in the driving forces.

Our dataset comprises $N = 38$ human sperms from 3 donors, of these, $N = 22$ sperms from 2 donors were imaged before and after the release of caged progesterone to study the effects of the hormone.

5.1. Quantitative description of sperm beating

In Fig. 5.2 we show a representative plot of the curvature, that is then processed as explained in chapter 3. The curvature is invariant under Galilean transformation of the reference system, hence it is perfectly suited to study the shape of an object, independently from its orientation in space. Hence, we study the curvature as proxy for the real shape.

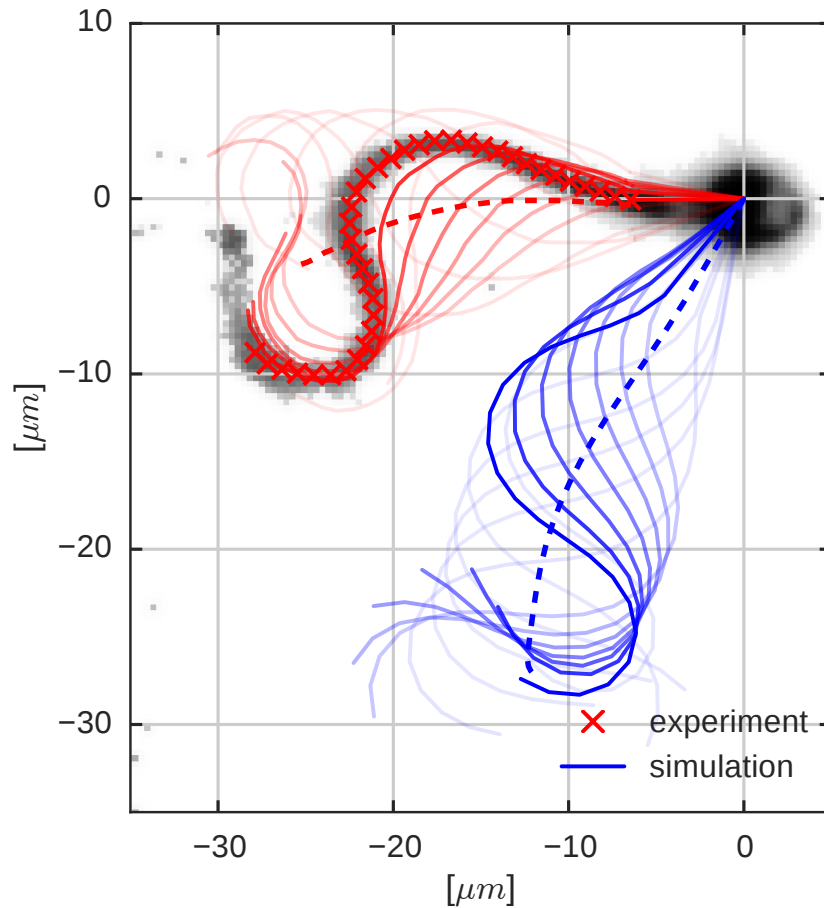


Figure 5.1.: Stroboscopic view of experimental tracking (red) and simulation with a semi-flexible filament and anisotropic drag-force (blue) - time is represented by the fading lines. The dashed lines represent the average shape in one period. The simulations match the wavelength, frequency and principal modes of the experimental data. The local bending torque is given by two traveling waves with frequencies ω_0 and $2\omega_0$ and mean zero. The rotation around the pinning point and the average curvature emerge naturally by this simple model (dashed line).

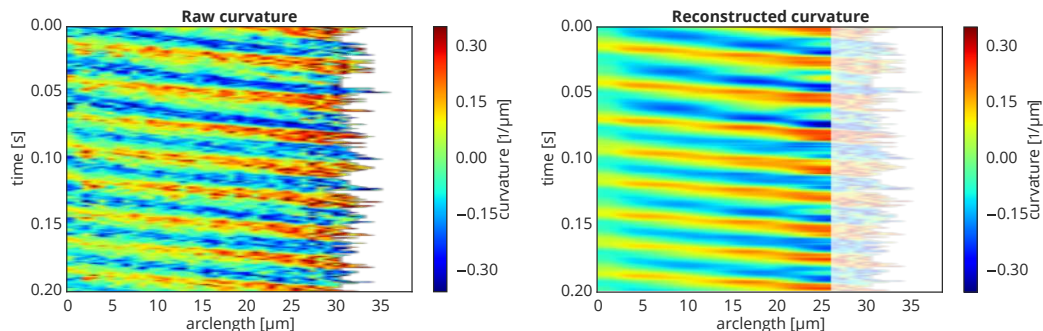


Figure 5.2.: (left) Unprocessed curvature of a beating flagellum measured from the tracking points. The number of points is not constant, hence some lines are longer than others. (right) The “reconstructed” curvature (see Methods) from three most important normal modes of the beating pattern (accounting for $\approx 95\%$ of the signal), effectively filtering the noise and highlighting the biological features. In transparency we show the data that is not possible to analyze with the proposed protocol.

We find that the curvature envelope increases towards the end of the filament (Fig. 5.3), with slope $\rho = 0.0057 \pm 0.0025 \mu m^{-2}$ both for normal sperm cells and after the release of the progesterone. The normal modes allow a direct inspection of the beating shape. In Fig. 3.4 we show that three modes always contain $\approx 95\%$ of the signal whatever the beating parameters and experiment type (with or without progesterone). In previous analysis a similar observation was done for *C. Elegans* and allowed investigating behavioral changes due to external stimuli. In our case, we are not (yet) interested in behavioral changes. However, we exploit the reduction of the relevant conformational space to the first three modes to assume that the biological behavior can be projected on the basis of the empirical mode. The same plot (Fig. 3.4) shows that the first two modes (the ones connected to the periodic beating) carry $\approx 80\%$ of the signal. In Fig. 5.4 we show the first two eigenmodes for both types of experiment (with and without progesterone). Surprisingly, rescaling the arclength by the wavelength of each experiment we obtain a unique couple of modes that is independent on the sperm cell and beating parameters (like, e.g.: frequency or curvature amplitude). This is a new point of view on the kinematic of the sperm beating that shows quantitatively the similarity of beating patterns of different cells.

As we discussed in methods, the curvature computed from the first three modes

has a lower noise-to-signal ratio and we can compute the Fourier transform with good precision even on short time-windows. This is important for the following analysis: since the frequency changes over time it is not possible to measure a power spectrum at once, but we need to perform the power spectrum on a sliding window. The result is called “spectrogram” (Fig. 5.8). The standard deviation of the measured frequency $\omega(t)$, then, does not indicate a measure error but the natural fluctuation of the signal. In Fig. 5.5(left) we compare the beating frequency of each different cell before and after the release of the progesterone. The scatter plot shows that, in average, the beating frequency of the normal sperm is faster. We also see that the standard deviation of the single (isolated) normal sperm is approximately 2 Hz , smaller than the standard deviation of the sample 5 Hz . The progesterone makes the beating frequency more unstable, indeed the standard deviation of single cell is approximately 4 Hz , the double of the case without hormone, and comparable with the sample std. dev. ($\approx 6.5\text{ Hz}$). In the right panel we performed a similar analysis for the wave velocity $c = \omega/k$: we find that the wave velocity is about $c = 1100 \pm 170\ \mu\text{m/s}$. The wave velocity is smaller after the release of progesterone, suggesting that as the wave-velocity decreases, the wave-vector is not affected. A preliminary confirmation can be seen in the plot of the eigenmodes (Fig. 5.4), that shows no appreciable differences between the modes of cells with and without progesterone. As before for the beating frequency, the standard deviation of the phase-velocity of a single normal sperm cell ($80\ \mu\text{m/s}$) is smaller than the one of the sample ($170\ \mu\text{m/s}$).

From the frequency and wave velocity we compute the dispersion relation $\omega(k)$. In principle we expect the frequency and wave-vector to be statistically independent. However, the plot of the average frequency and wave-vector (Fig. 5.6) shows that there may be a (linear) dispersion relation. At the moment of writing we cannot measure the dispersion relation with the precision of each beating of each cell: what Fig. 5.6 suggests a possible statistical relation detected from the population of sperms in our sample.

We turn now our attention to the steering mechanism that is responsible for the rotation around the pinning point (Fig. 5.1). Because of its intrinsic importance and the novelty of the main result, we present the work in a separate section. We will

5. Flagellar Beat of Pinned Human Sperm

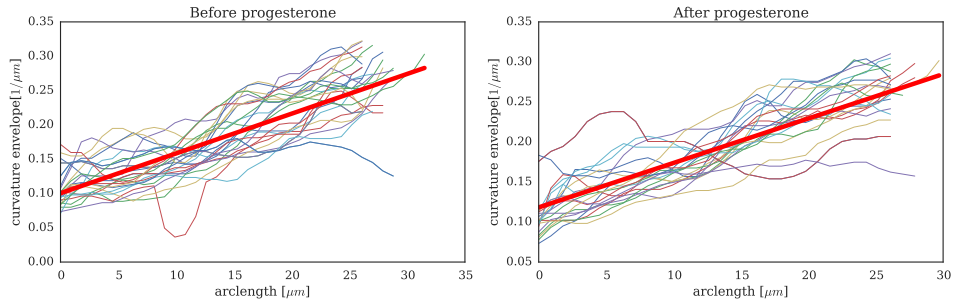


Figure 5.3.: Average envelope of the curvature for normal spermatozoa (**left**) and doped spermatozoa (**right**). The curvature increases linearly towards the end, with slope $\rho = 0.0057 \pm 0.0025 \mu\text{m}^{-2}$ for both cases.

then conclude the chapter with a brief discussion of the active and dissipated work.

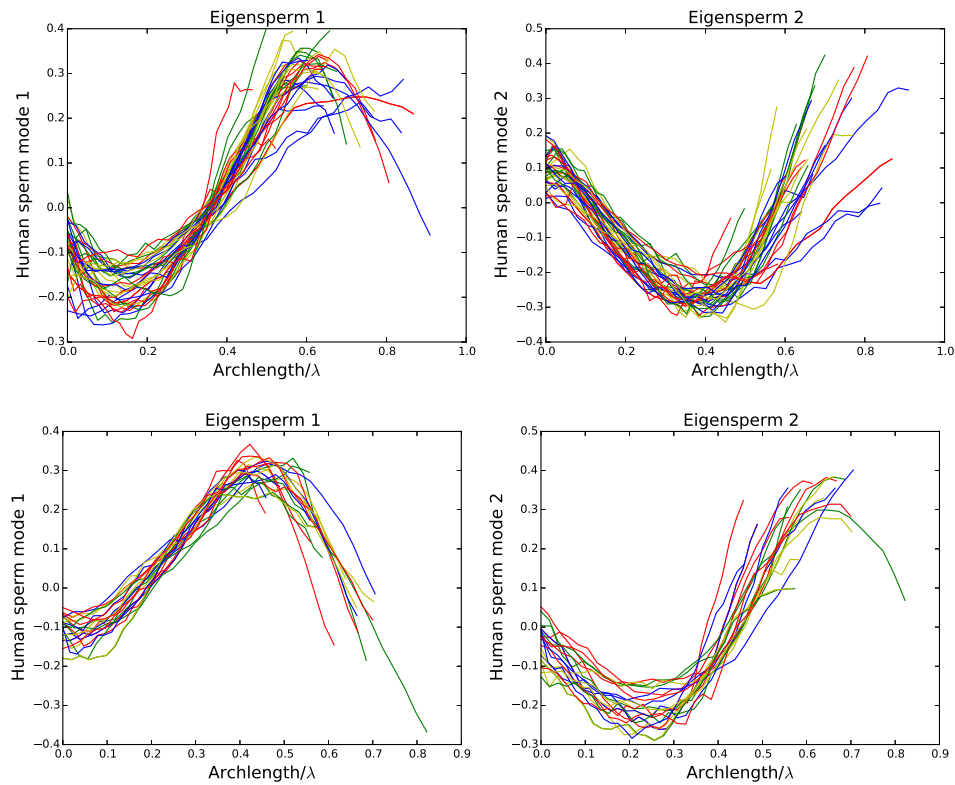


Figure 5.4.: (Top) Normal human sperm, (Bottom) Human sperm with progesterone. We show here that the first two eigenmodes of human sperms are similar between all experiments when the arclength is rescaled by the wavelength (λ). This suggests that the qualitative differences observed in the raw-movies can be simplified to a more general behavior.

5. Flagellar Beat of Pinned Human Sperm

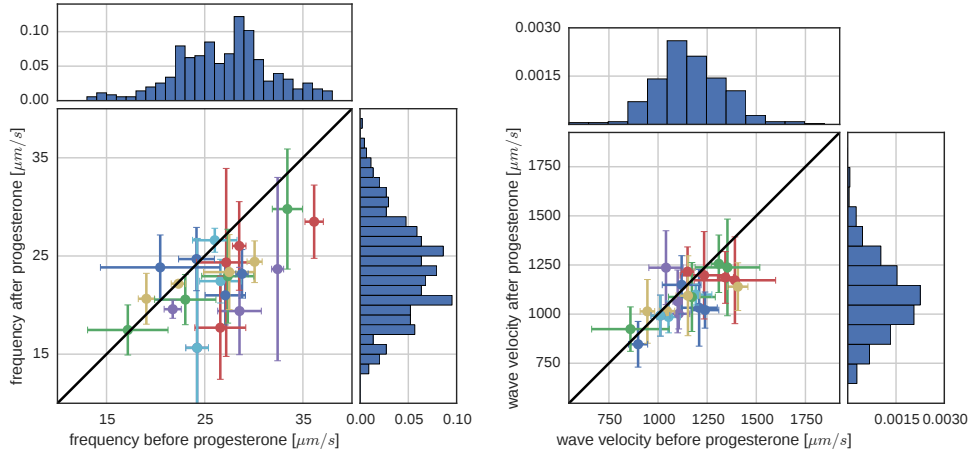


Figure 5.5.: (Left) Frequency distribution after the release of progesterone *versus* the frequency before the release. In the *central* plot we plotted the average and standard deviation of the frequency. Note that the frequency after the release of progesterone is smaller than the frequency before. Observe that the standard deviations of the single cell is $\approx 2 Hz$ (normal cell) and $\approx 4 Hz$ (with progesterone). In both cases, the sample standard deviation is $\approx 6 Hz$ (*side and top*). (Right): Same analysis for the wave velocity.

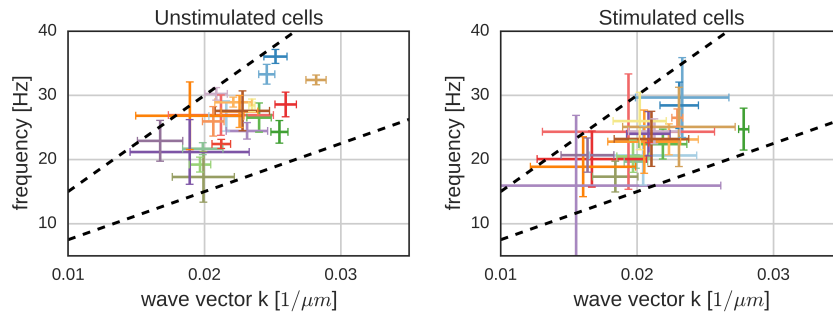


Figure 5.6.: Dispersion relation $\omega(k)$. In principle, each sperm cells should be free to choose any frequency independently from its wave-vector. However, the correlation shown in the plots indicates that there may be a (linear) dispersion relation. The dashed lines correspond to phase velocities $0.750 mm/s$ and $1.500 mm/s$, corresponding approximately the lower and upper bound of the observed velocity in Fig. 5.5.

5.2. Steering with Higher Harmonics

Analyzing the power-spectrum of the curvature we noticed that most sperms have a pronounced component at twice the beating frequency (Fig. 5.7). At the same time we realized that modeling the rotation velocity with a predefined curvature does not reproduce some experimental observations. Here we discuss our findings on the role of higher harmonic component as an effective steering mechanism. The manuscript is in preparation (see Ref [103]).

Introduction

For a swimming microorganism, steering in response to environmental cues is as important as propulsion, because only by a combination of the two a target can be reached, thereby making the distinction between success and death. In particular, this applies to spermatozoa; on their way to the *ovum* they sense the rheology and the concentration gradients of the medium [101], and use the integrated information to reach their target. The chemical-sensing mechanism is rather established [104]: spermatozoa swim in circles, and the local density of signal determines if the trajectory is more or less bent [100].

One proposed steering mechanism is by a curved body [52, 79].

Is this the only way to control the trajectory at low-Reynolds numbers?

With high-speed recording (500 to 1000 fps) of pinned human sperm cells we found that the beating pattern is characterized by the higher frequencies, typically peaked around integer ratios of the fundamental one (Fig. 3.3). Hence, we call them “the higher harmonics of the sperm beating”. The immediate effect of these components is that at each point of the flagellum the curvature is not symmetrically oscillating like a sine wave, but has an asymmetric shape with a steeper side (Fig. 5.7(center)). The spectrogram of the curvature allows measuring the different components of the Fourier spectrum during the experiment: we found that the second harmonic is almost always present and it strongly correlates with the rotation velocity around the pinning point (Fig. 5.7(bottom)).

This observation raises many questions both on the physics of microswimmers and

5. Flagellar Beat of Pinned Human Sperm

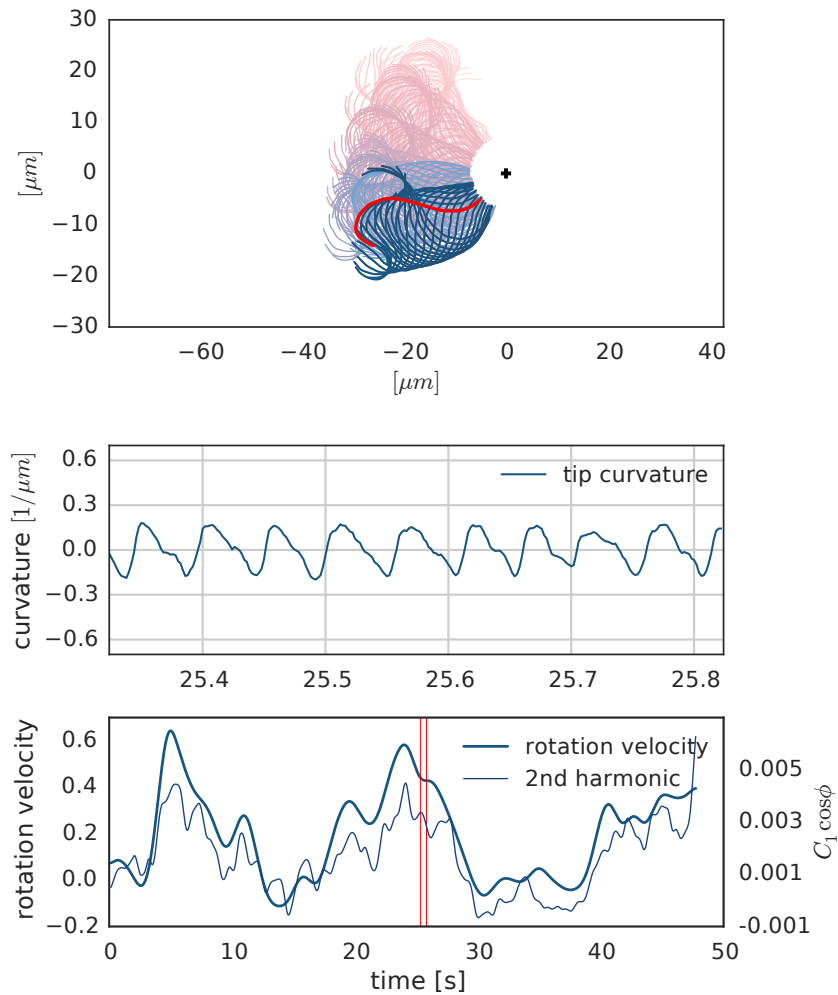


Figure 5.7.: Rotation around the pinning point from high-speed microscopy of the beating pattern. **Top:** Trajectory of the flagellum of a human sperm. The sperm cell is rotating around its head. **Center:** Curvature at $25\mu\text{m}$ from the initial tracking point (compare also with Fig. 5.2). **Bottom:** Plot of the rotation velocity (thick line) and of the second harmonic (thin line) during the experiment. The central plot corresponds to the time window represented by the two red lines.

on the biology of spermatozoa. We address here the following three:

- Can a simple superposition of traveling waves with increasing harmonic frequencies generate a force perpendicular to the flagellum?
- Is the rotation that we observe in the experimental data a consequence of the higher components?
- How do sex-related hormones (e.g. progesterone) affect the beating spectrum and rotation?

5.2.1. Resistive-Force Theory

It is well known that a reciprocal motion does not generate a net propulsive force on any microswimmer [7]. Spermatozoa solve this issue with a traveling wave from the body to the tip: it breaks the front-back symmetry and provides the net thrust in the forward direction (\hat{x} in the following). However, along the perpendicular direction the wave-like motion is periodic and reversible: intuitively, we expect no net force whatever the Fourier spectrum.

We can easily estimate the parallel (f_x) and the perpendicular (f_y) forces in the “small amplitudes” approximation [5]. We recall that, in this approximation, the flagellum lies along the \hat{x} direction. The \hat{y} direction defines the shape: in this case a superposition of two traveling waves with amplitudes y_0 and y_1 respectively

$$y(s, t) = y_0 \sin(ks - \omega t) + y_1 \sin(ks - 2\omega t + \phi),$$

where k is the wave vector and s is the arclength. Note that the amplitude of the second harmonic has to be smaller than $y_1 \leq 0.3y_0$ to have a smooth sawtooth profile.

In the framework of resistive-force theory [49], the slender shape of the flagellum experiences an anisotropic drag-force

$$\mathbf{f}(s, t) = -\xi_{\perp} \mathbf{v}_{\perp} - \xi_{\parallel} \mathbf{v}_{\parallel} \quad (5.1)$$

where $\mathbf{v}(t, s)$ is the velocity of the filament at arclength s at time t , and ξ_{\perp} and ξ_{\parallel} are the drag coefficients in the perpendicular and tangential directions. Inserting the

shape $y(s, t)$ in the force, the net-propulsive and perpendicular forces per period are given by

$$f_x(s) \approx k\omega (\xi_{\perp} - \xi_{\parallel}) (y_0^2 + 2y_1^2) \quad (5.2)$$

$$f_y(s) \approx k^2\omega (\xi_{\perp} - \xi_{\parallel}) y_1 y_0^2 \cos(ks + \phi). \quad (5.3)$$

Undoubtedly, having higher harmonics allows to go faster ($f_x \propto y_0^2 + 2y_1^2$), but not straight: the force perpendicular to the flagellum f_y is, in general, not zero.

In experiments, we have access to the rotation velocity around the pinning point that, by force balance, is due to the net torque around the pinning point $T(s) \approx s f_y(s)$. A straightforward integration gives:

$$\frac{\Omega}{\omega} \underset{2\pi/k \rightarrow L}{\propto} y_1 \sin(\phi). \quad (5.4)$$

It is then clear that, while a single frequency cannot generate thrust perpendicular to the flagellum, a simple linear superposition will. Hence, flagellum shapes defined by the first and higher harmonics can be an effective mechanism to control the swimming direction of slender micro-swimmers. We call $y_1 \sin \phi$ the “second harmonic intensity”.

5.2.2. Derivation of the Net Normal Force

We show here how to obtain Eq. (5.4) proceeding in two ways: we initially show how to proceed in the case the shape of the flagellum can be described in terms of the small deviations $y(s, t)$, we then redo the calculations imposing a given curvature, without restriction on the actual shape.

The intentions of this (sub)section is mainly pedagogical and is not essential to the understanding of the remaining of the chapter: while the first approach is quite simple, it is based on a *a priori* approximation that the shape has small amplitudes. The second approach, instead, computes the final observables without approximations on the shape until the very end, when the limit of small curvature is finally taken. This allows comparing the two results gaining insight on the errors done by reasoning along the lines of the first approach.

Nearly Straight Filaments

We describe the flagellum as a filament between 0 and 1 along the \hat{x} axis. For small bending, the \hat{x} direction can be confused with the arclength $s \approx \hat{x}$ and the shape of the flagellum is given as a deviation from the straight line $y(s, t)$:

$$y(s, t) = y_0 \sin(\omega t - ks) + y_1 \sin(2\omega t - ks + \phi), \quad (5.5)$$

where y_0 is the amplitude of the dominant harmonic and y_1 is the amplitude of the second harmonic. The resistive force is :

$$\mathbf{f}(s, t) = -\gamma_{\parallel}(\mathbf{v} \cdot \hat{\mathbf{t}})\hat{\mathbf{t}} - \gamma_{\perp}(\mathbf{v} \cdot \hat{\mathbf{n}})\hat{\mathbf{n}} \quad (5.6)$$

where the velocity $\mathbf{v}(s, t)$ of the element of filament in position s is:

$$\mathbf{v}(s, t) = \begin{pmatrix} 0 \\ \partial_t y(s, t) \end{pmatrix} \quad (5.7)$$

and the tangent and normal vectors read

$$\mathbf{t}(s, t) = \frac{1}{N} \begin{pmatrix} 1 \\ \partial_s y(s, t) \end{pmatrix}, \text{ and } \mathbf{n}(s, t) = \frac{1}{N} \begin{pmatrix} -\partial_s y(s, t) \\ 1 \end{pmatrix} \quad (5.8)$$

with normalization $1/N^2 = 1/(1 + (\partial_x y)^2) \approx 1 - (\partial_x y)^2$. Inserting Eqs. (5.7), and (5.8) in Eq. (5.6) we obtain the instantaneous force density on the body:

$$\begin{aligned} f_x(x, t) &= -(\xi_{\perp} - \xi_{\parallel}) \partial_t y \partial_x y, \\ f_y(x, t) &= -(\xi_{\perp} - \xi_{\parallel}) \partial_t y (\partial_x y)^2. \end{aligned} \quad (5.9)$$

Substituting the filament shape $y(s, t)$ and averaging over time we obtain the expression for Eqs. (5.2).

The forces in the \hat{y} direction is, in average, not null and can thus generate a net

torque:

$$\begin{aligned} T_a &= \frac{\omega}{2\pi} \int_0^L ds \int_0^{\frac{2\pi}{\omega}} dt s \times f_y(s, t) = \\ &= (\xi_{\perp} - \xi_{\parallel}) \omega y_1 y_0^2 (kL \sin(kL + \phi) + \cos(kL + \phi) - \cos(\phi)) \end{aligned} \quad (5.10)$$

$$\stackrel{\approx}{\lambda \rightarrow L} (\xi_{\perp} - \xi_{\parallel}) 2\pi \omega y_0^2 y_1 \sin(\phi) . \quad (5.11)$$

Note that the torque is proportional to the higher harmonic component, thus if $y_1 = 0$ the torque would be 0 – besides the possible complications generated by a non-trivial wavelength (Eq. (5.10)), the sign of the torque is essentially due to the sign of $y_1 \sin(\phi)$ as we find in both the experimental data (Fig.5.10) and the simulations (Fig.5.12).

The torque generated by the second harmonic T_a is balanced by the torque generated by the perpendicular viscous drag T_v . Here, we estimate the viscous torque as the torque at one end of a straight rod rotating with angular velocity Ω :

$$T_v = - \int_0^L ds \xi_{\perp} \Omega s \times s = -\frac{\xi_{\perp}}{3} \Omega L^3 . \quad (5.12)$$

The sum of the two torques must be zero to satisfy momentum balance $T_v + T_a = 0$ and yields Eq. (5.4):

$$\frac{\Omega}{\omega} \propto y_1 \sin(\phi) . \quad (5.13)$$

Prescribed Curvature

Let's consider a flagellum whose center-line s is described by the curvature $C(s, t)$:

$$C(s, t) = C_0 \cos(ks - \omega t) + C_1 \cos(ks - 2\omega t + \phi) \quad (5.14)$$

where C_0 , and C_1 are the curvature-amplitudes of the two harmonics and $0 < \phi < \pi$ is the second-harmonic phase. The shape $\mathbf{r}(s, t)$ of the flagellum on the plane is given by Eqs. 2.13.

In the framework of resistive-force theory the force-density felt by the flagellum can be rewritten as

$$\mathbf{f}(s, t) = -\xi_{\perp} (\mathbf{1} + \zeta \hat{\mathbf{t}}\hat{\mathbf{t}}^T) \mathbf{v}, \quad (5.15)$$

where $\mathbf{v}(t, s)$ is the velocity of the filament at arclength s at time t . Since the trajectory of the flagellum is periodic, only the term proportional to $\zeta = (\xi_{\parallel}/\xi_{\perp} - 1)$ can contribute to a net force and torque. Inserting Eq. (5.14) in Eq. (2.13) and Eq. (5.15), we find the active torque to be:

$$T_q \propto_{C_0 \rightarrow 0} \zeta C_1 C_0^2 \lambda^3 \left(\frac{\lambda^3}{L^3} \right) f(\lambda/L, \phi) + o(C_0^4) \quad (5.16)$$

where, for simplicity, we assumed the sperm head to be clamped ($\psi_0 = 0$, $\vec{r}(0, t) = \vec{0}$). The function $f(\lambda/L, \phi)$ is a periodic function of ϕ :

$$\begin{aligned} f(\lambda/L, \phi) &= 2k^2 L^2 \sin(kL - \phi) + 3 \sin(kL - \phi) \\ &\quad - 3kL \cos(kL - \phi) + 3 \sin(\phi) \\ &\underset{\lambda \rightarrow L}{\sim} (4\pi \sin(\phi) - 3 \cos(\phi)) \end{aligned} \quad (5.17)$$

where λ is the wavelength. We finally find:

$$\frac{\Omega}{\omega} \propto C_1 (4\pi \sin(\phi) - 3 \cos(\phi)). \quad (5.18)$$

The contribution of higher harmonics contributes to higher orders in C_0 , but they were not seen in the experimental data. Note that odd harmonics generate no net torque.

Comparing Eq. (5.4) and Eq. (5.18) we see that the two approaches lead to the same result in the limits of small amplitude (of course) with $\lambda \approx L$, and $\phi \approx \pi/2$. For us, this is enough because more precise quantitative comparisons to the experimental data do not lead to more physical insights, and would simply be a theoretical exercise.

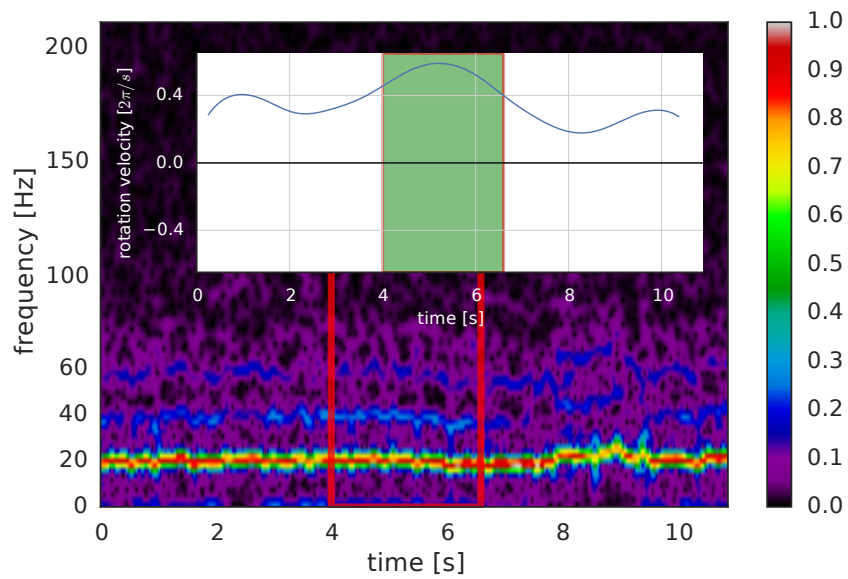


Figure 5.8.: Spectrogram of the curvature at $\sim 25\mu\text{m}$ from the pinning point for one experiment of human sperm (color code by power spectrum, normalized to the max. value). The fundamental mode correspond to $\omega_0 \approx 20\text{ Hz}$ (red and yellow), the higher harmonics can be seen at $2\omega_0$ and $3\omega_0$. In the red window we marked a window of particularly intense second harmonic. **Inset:** Rotation velocity. In the green window we highlighted the same time window as in the main plot: the rotation velocity increases when the second harmonic has the strongest activity.

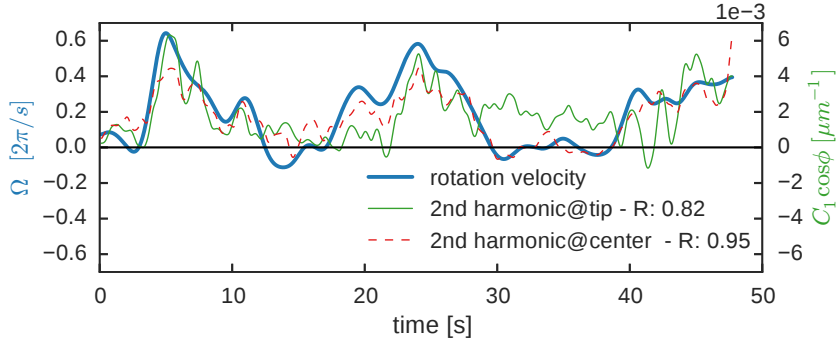


Figure 5.9.: The rotation velocity of a spermatozoon is not constant (thick blue line). In this picture the contribution of second harmonic follows precisely the same dynamics of the rotation velocity (Human sperm). The parameter R measures the correlation between the two signals. The two plots show that the measure point does not strongly affect the measure.

5.2.3. High-speed Microscopy of the Beat Pattern of Human Sperm

Now we want to compare the theoretical prediction (Eq. (5.4)) to the experimental data that we presented in the previous section.

We measure the evolution of the second harmonic amplitude y_1 , and phase ϕ from the spectrogram of the flagellum curvature. In Fig. 5.8 the spectrogram of one experiment is plotted (note that only the amplitude component can be plotted): the second and third harmonics are clearly visible. Observe that at periods with a higher rotation velocity correspond periods with more intense y_1 , this is of course not general, as the plot ignores the information of the phase. Per each experiment we obtain two signals (as shown in Fig. 5.9): the second harmonic amplitude $y_1 \cos \phi$ (thin line) and the rotation velocity Ω (thick line). During the experiment, the sperm cells “decide” if and when to change rotation direction, this means that intensity and sign of both signals are not constant. This natural behavior is exploited to define the correlation coefficient R between the rotation velocity and the second harmonic intensity:

$$R = \frac{E_t(XY)}{\sqrt{E_t(X^2)E_t(Y^2)}} \quad (5.19)$$

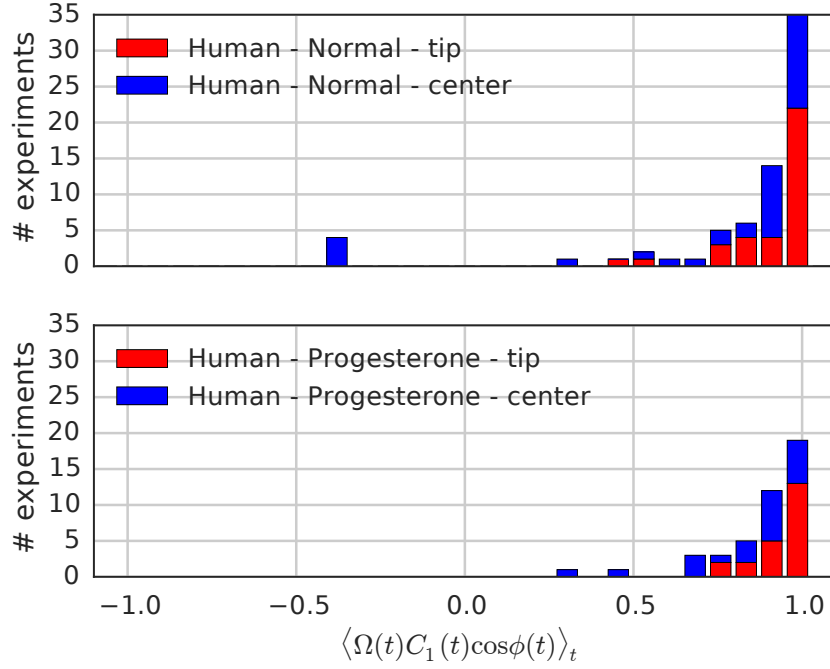


Figure 5.10.: Each experiment is characterized by a correlation coefficient between the rotation velocity Ω and the second harmonic intensity $y_1 \cos(\phi_{\text{eff}})$. The histograms show that both before and after the release of progesterone the second harmonic is strongly correlated with the rotation velocity. The correlation does not change if the measure is done at arlength $25 \mu\text{m}$ (red) or $15 \mu\text{m}$ (blue)

where $X = \Omega(t)$ and $Y = y_1(t) \cos \phi_{\text{eff}}(t)$, and $E_t(\cdot)$ denotes the average value during the experiment. On the contrary to the usual correlation coefficient, X and Y are not centered around their mean values. This choice satisfies the physics intuition that to a constant second harmonic corresponds a constant rotation velocity.

In Fig. 5.10 the histogram of the correlation coefficient shows that there is indeed a strong correlation between the two signals. Cells with progesterone show a slight better correlation, probably because the signal-to-noise ratio of the second harmonic is stronger. We show in Fig 5.11 that, after the release of progesterone, all sperm cells beat with slower frequency than in normal conditions (left panel) but rotate faster around the pinning point (right panel). A direct measure of the second harmonic contribution before and after the release (Fig. 5.11, right panel) highlights that progesterone increases the intensity of the second harmonic, causing the faster

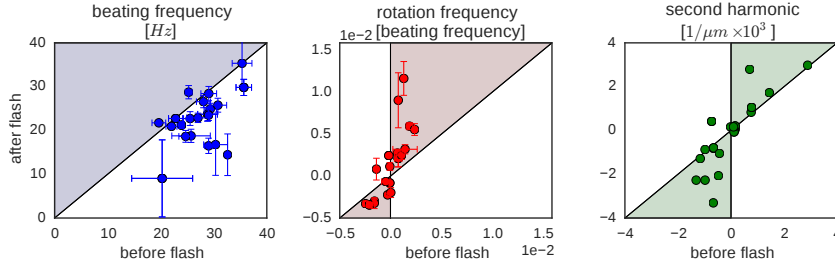


Figure 5.11.: Beating frequency (**left**) and rotation frequency (**center**) before and after the release of caged progesterone. Even if the beating frequency after the release of progesterone is lower than before (**left**), the rotation frequency is bigger (**red**). **Right:** second harmonic intensity with and without progesterone. The second harmonic is more intense after the progesterone release, explaining why the cells rotate faster even if the beating frequency is smaller. **All:** if a point is inside the highlighted cones, its values after the stimuli is bigger than before the stimuli.

rotation velocity.

Note that we want to correlate the rotation velocity with the measured second harmonic amplitude and phase via the linearized theory (Eq. (5.4)). However, the real curvature has more features than the simplified one that we assumed in computing Eq. (5.4): in particular, the expression for the torque becomes much more complex if we allow the curvature envelope to be not constant and let the wave-vector to be very different from the filament length. These simplifications influence the phase ϕ , that is, then, corrected as $\phi_{eff}(t) = \phi(t) + \phi_{correction}$. The correction is determined to maximize the correlation but is expected to be a simple constant that incorporates all the missing information: it is not obvious that such a constant gives also a good overall correlation R because of the non-linear relation between Ω and ϕ_{eff} .

Fig. 5.10 and Fig. 5.11 show that our predictions are, in average, satisfied by the experimental data: there is indeed a good correlation between the measured rotation velocity and second harmonic intensity. A correlation does not imply a causal relation, however. In the next subsection we show how we can reproduce the experimental dynamic of individual experiments by simulating a beating sperm whose bending forces have the measured higher harmonic component.

5.2.4. Simulations of Human Sperm

We find that to reproduce the beating pattern *in silico* the sperm is modeled as a simple semi-flexible filament characterized by a uniform bending stiffness κ . The filament is bend a prescribed bending torques in the form of a traveling wave with two harmonics (Fig. 6.4):

$$T(s, t) = b_d \times A_0 \sin(ks - \omega_0 t) + b_d \times A_1 \sin(ks - 2\omega_0 t + \psi) \quad (5.20)$$

where b_d is the beads distance. The portion of data that correspond to the passive head and midpiece is modeled as a passive semi-flexible filament. The hydrodynamic forces are modeled via anisotropic drag force (Eq. (5.1)). The filament is pinned at one end.

Even if the curvature increases towards the end, there is not need to explicitly model the driving forces in the same way: the asymmetry comes by itself.

Since the beating pattern is not constant and the frequency has a variance of 2 Hz (Fig. 5.8 and Fig. 5.5) the fit is done on windows of 10 to 100 periods that proved to be stable and accurate enough. In each window we measure the frequency ω , length L , phase ψ and pinning-point to flagellum distance, and fit the first two simulated normal modes to the experimental ones to find the wave vector k , the stiffness κ and the torques intensity A_0 . From the rotation velocity around the pinning point we estimate A_1 .

Note that the eigenmodes describe only how the curvature changes along the filament, and bring no information on the actual value of the curvature. For this reason we multiply each mode by it maximum amplitude $\max_t \chi_n(t)$ [μm^{-1}]. The estimated stiffness is in the range of $1nN\mu m^{-2}$, compatible with the stiffness of 10 double microtubules. The amplitude of the main driving torque $A_0 \approx 0.5\kappa$. The current fitting protocol does not allow estimating appropriate errors, yet.

The results of the fit confirm that bending torques with higher harmonics can indeed generate a torque around the pinning point. But this time, the full non-linear solution highlights more features: an average curvature arises spontaneously and

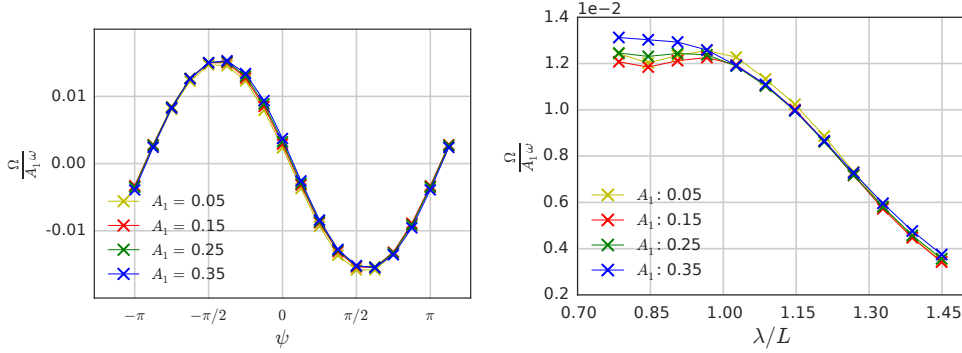


Figure 5.12.: (Left) Simulations of actuated semi-flexible filament with anisotropic drag-force. The rotation velocity scales linearly with A_1 and is modulated by the phase $\cos(\psi + \psi_0)$ - the actual value of ψ_0 depends on all the other parameters. Simulation parameters: $\kappa \sim 1nN\mu m^2$, $A : 0.6\kappa$, $\omega = 28 Hz$, tail $L = 41\mu m$, $\xi_{\perp}/\xi_{\parallel} = 1.81$ and $L/\lambda = 1.26$. (Right) Same parameters of the adjacent plot. The wavelength changes the rotation velocity when it is longer than the filament.

breaks the chirality of the spermatozoon. In the experimental data we observe a similar average curvature (Fig. 5.1). A different visualization of the effect of the second harmonic is shown in Fig. 5.14: each frame is rotated so that the midpiece is parallel to the x axis. When $A_1 \neq 0$ the beating pattern is clearly asymmetric with respect to the x axis.

The simulation allows investigating how the rotation velocity depends on parameters around the experimentally meaningful values of the fit. In Fig. 5.12 we plotted the rotation velocity Ω/ω vs the phase ψ and amplitude A_1 of the higher harmonic contribution; the other parameters (stiffness and frequency and A_0) are the same of the fit. The simulations confirm Eq. (5.4): the linear scaling with A_1 holds also for the biologically important case of “big” amplitudes and the rotation has the expected periodic dependence on the input phase ψ . Figure 5.12 shows that when the wavelength $\lambda < L$, the rotation velocity is essentially independent from the wavelength, while longer wavelengths reduce the rotation velocity.

5. Flagellar Beat of Pinned Human Sperm

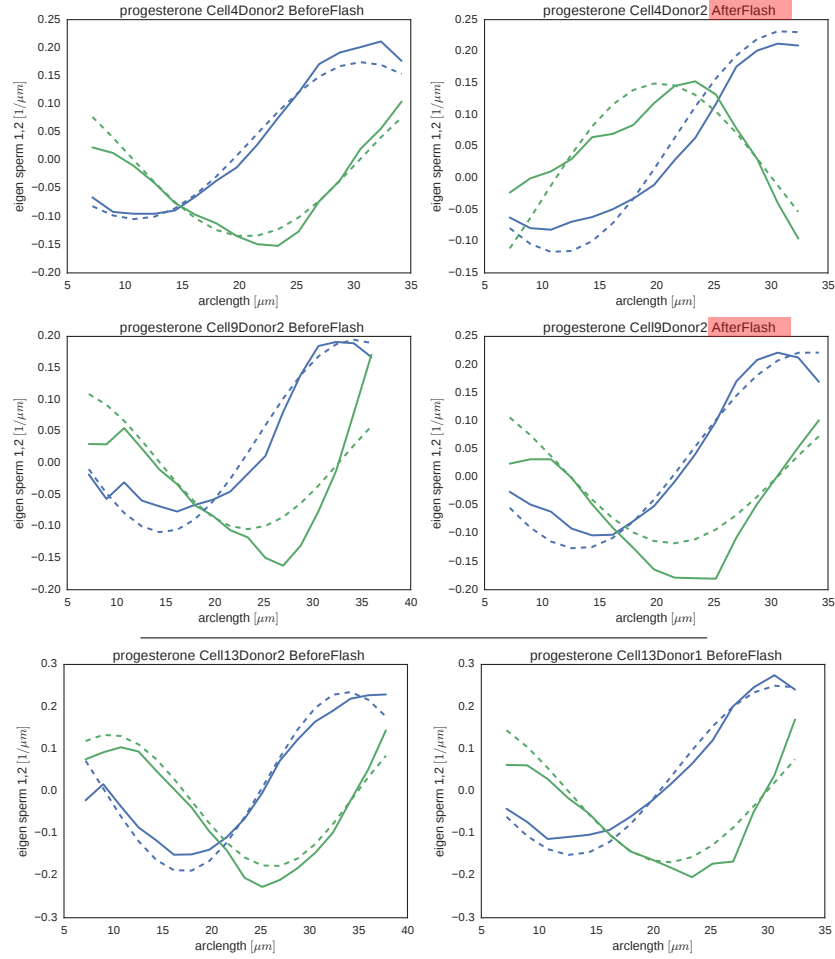


Figure 5.13.: First two experimental eigenmodes (solid lines) and best-fitting eigenmodes (dashed lines) for 6 experiments on 4 different cells. In red we marked the plots corresponding to experiments with progesterone. Note that the modes are multiplied by their maximum intensity $\chi_{1,2}$ respectively. The estimated bending rigidities are $\kappa \approx 1 - 2nN\mu m^2$, and torque strength $A \approx 0.5\kappa$.

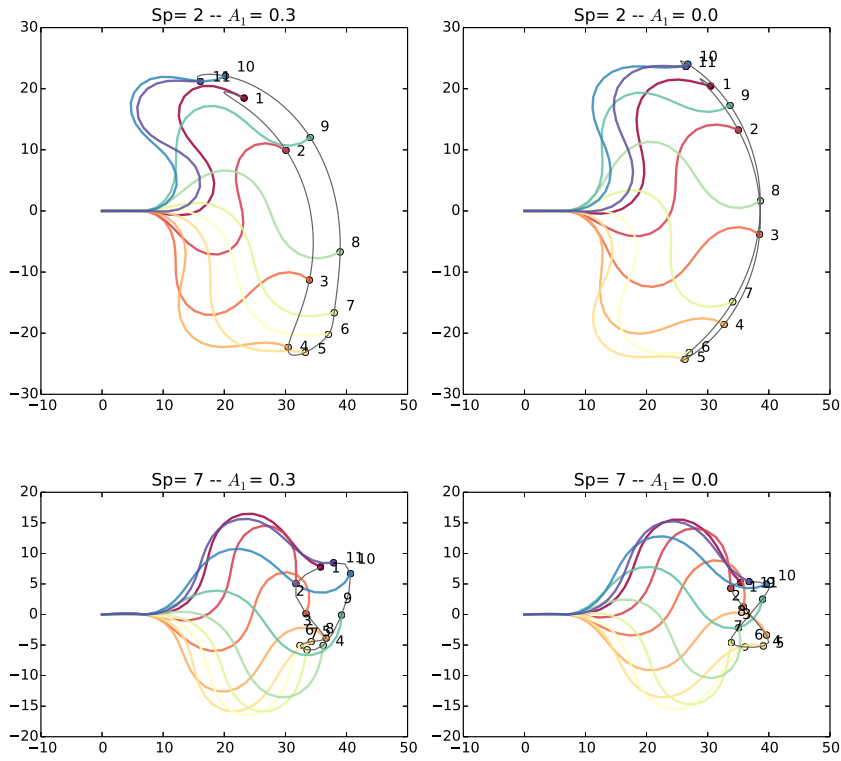


Figure 5.14.: Comparison between flagellar beats for different sperm numbers $Sp = L(\omega\xi_{\perp}/\kappa)^{1/4}$ and second harmonic amplitude A_1 . The shapes are plotted in the reference system of the neck. Without second harmonic the trajectory of the end-point of the flagellum follows an 8-figure. The second harmonic destroys the symmetric 8-figure, and the beating pattern is essentially asymmetric, coherently with the average curvature shown in Fig. 5.1.

Discussion on the fit

Fitting the experimental data can be difficult and tricky at first. We report here some notes and early (mostly failed) attempts. Note that we always work on one cell at a time, and infer no information on the current fit from fits on other cells.

Flagellum length We want to make the most simple and less *ad-hoc* model possible.

However, if the initial determination of the geometry (e.g. length, pinning point position, . . .) is inaccurate, a more complicate model is needed. This happened to us initially, when working on very short datasets that never tracked the flagellum up to its full length. The consequence was that we expected the flagellum to be some $8\mu m$ shorter and needed to include a arclength-dependent torque.

Neck length The sperm cell is not pinned at the flagellum base, but somewhere in the head. We call *neck* the distance between the flagellum base and the pinning point and it is modeled as a passive and straight part of semi-flexible filament that represents part of the head and the midpiece. It shifts the active bending torques by some $7\mu m$ from the pinning point. It is difficult to predict theoretically how this distance affects the dynamics and at the same time to have accurate data in this region. The choice to estimate a neck-length of about $7\mu m$ is more empirical and intuitive than due to quantitative estimates.

Curvature r.m.s. As said, we minimize the r.m.s. from the curvature's eigenmodes.

This is only one of many choices. We also tried to optimize the curvature itself or its variance. The first idea never worked properly because the fit finds multiple minima and it is hard to scan all minima to find the infimum. The second because the variance gives a statistical measure of the signal, and does not filter out the noise, hence the fit always over-estimated the real curvature.

Parameters It is practically impossible to fit all the parameters at once (L , λ , A_0 , κ , A_1 , and ψ). We decided to fit only the parameters that cannot be measured directly.

Initial values Initial values are critical for the success of the fit. Some values, like the neck-distance or the length can be successfully estimated only from the longest available track. Frequency, beating amplitude and wave-vector change quite often, hence they should be measured for the time window that is going to be fitted.

Normal modes The normal modes can be tricked by changes in the behavior. If the behavior is not stationary (e.g.: there are intermittent phases of hyper-activation and normal beating) the normal modes are best determined independently in each phase.

Integration When thinking of fitting, one usually thinks of fitting a function to some data. In our case, however, we fit a simulation. This means that the simulation has to be fast and able to successfully integrate a big volume of the parameters space, as it is hard to forecast the path taken by the fitting algorithm. In our case, this is done integrating with an adaptive time-step algorithm (appendix A).

Fitting The fitting protocol is divided in two steps: a first step estimates κ and A_0 by optimizing the first two normal modes. A second step estimates A_1 and ϕ from the rotation velocity. This approach was devised because the first two normal modes are not heavily affected by the second harmonic, hence the second step does not affect strongly the first one. We usually apply the steps iteratively for a couple of loops.

5.2.5. Summary

Microorganisms need to control their swimming direction as response to endangering situations, feeding or other reasons. It was long believed that spermatozoa control their swimming direction via the average curvature. This is an intuitive mechanism that probably plays a role as steering mechanism, but we have shown that it is not the only one and the real cell may have plenty of other options to control its motion in other ways. The mechanism that we found is less intuitive than a shape anisotropy, but it is not a mere theoretical tool. We have shown that the predicted

theoretical correlation between rotation velocity and second-harmonic intensity is verified experimentally.

To strengthen the correlation to a causal relation between second harmonic and rotation speed we developed a simple simulation of beating sperm that fits the experimental data. This is, *per se*, a novel approach because previous analyses were restricted only to the observable kinematic [52]. The dynamics of the beating can be accurately reproduced once the correct parameters are given. We have shown that driving the filament beating with two harmonics allows fitting not only the shape of the beating, but also the rotation velocity. In the experimental data we measure also an average curvature (Fig. 6.4). *A priori*, we do not know if it is due to an explicit mechanism. However, the simulations that fit the beating shape and rotation velocity show that although the torque has zero average value, an average curvature is spontaneously generated by the higher-harmonics driving.

This observation enhances our confidence that the higher harmonic contribution is indeed the cause of the rotation.

5.3. Dissipation and Work

Part of power generated by the molecular motors of a beating spermatozoon is dissipated into the fluid and we estimated from the tracked flagellum, assuming that the hydrodynamic interaction be described by the resistive-force theory

$$\begin{aligned} D_v(s) &= \frac{1}{T} \int_0^T dt \mathbf{f} \cdot \mathbf{v} \\ &= \frac{1}{T} \int_0^T dt (-\gamma_{\perp} v_{\perp} \hat{\mathbf{n}} - \gamma_{\parallel} v_{\parallel} \hat{\mathbf{t}}) \cdot \mathbf{v}(s), \end{aligned} \quad (5.21)$$

where T is the beating period and s is the arclength. In Fig. 5.15(top) we plot $D_v(s)$ computed by estimating \mathbf{v} , $\hat{\mathbf{n}}$, and $\hat{\mathbf{t}}$ from the data. In our dataset the drag coefficients may have different values, however now we are interested only in the qualitative trend along the arclength. As we show in Fig. 5.15(bottom), the drag ratio influences somehow the trend, that is linear for $\gamma_{\perp}/\gamma_{\parallel} = 1$ but “less” linear $\gamma_{\perp}/\gamma_{\parallel} = 1.81$. Since we do not know the exact drag ratio for human spermatozoa,

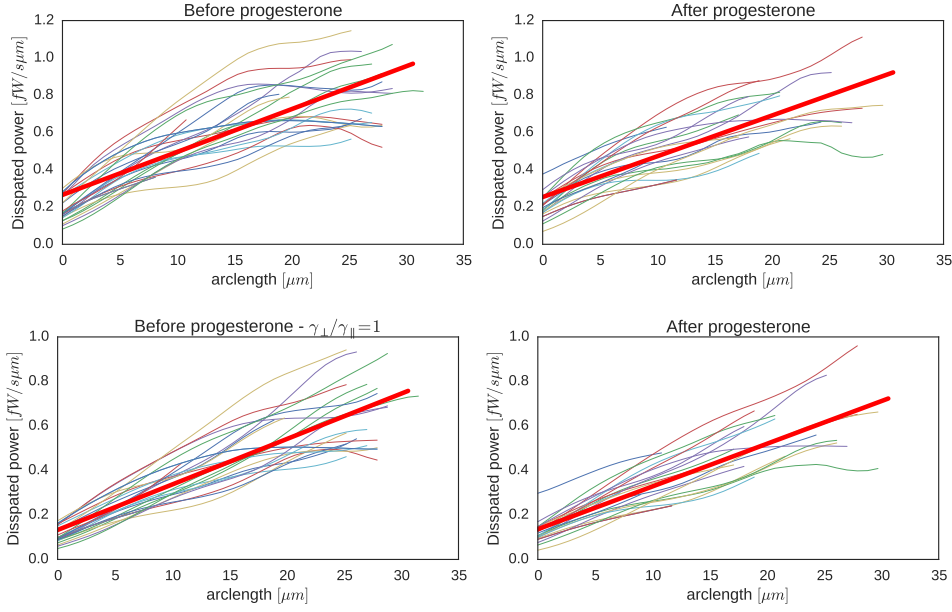


Figure 5.15.: **(Top)** Dissipated power density [$fW/\mu m$] for normal beating spermatozoa (left) and doped spermatozoa (right). The drag ratio is $\gamma_{\parallel}/\gamma_{\perp} = 1.81$. The red thick line is the average interpolating line. **(Bottom)** Dissipated power compute for isotropic drag ratio $\gamma_{\parallel}/\gamma_{\perp} = 1$. Observe that both trend are, essentially, linear.

we conclude that, within the current resolution, the dissipation increases linearly towards the flagellum end and we obtain:

$$D_v(s) = 0.023 \pm 0.007s [fW/\mu m^2] + 0.26 \pm 0.1 [fW/\mu m] \quad (5.22)$$

for both normal beating spermatozoa and doped spermatozoa.

It is interesting that the total dissipated power is $D_v \approx 20fW \approx 4fJ/\text{stroke}$, comparable to the work done by a single cilium in a carpet of cilia [105].

Since we have shown in the previous section that the dynamics of the pinned spermatozoa can be fitted by simple active bending torques

$$T(s, t) = A_0 \sin(\omega t - ks) + A_1 \sin(2\omega t - ks + \phi) . \quad (5.23)$$

We can estimate the (active) work done in the filament by the torques and compare

it to the dissipated power as, in general, it needs not to follow the same linear trend as the dissipated power $D_v(s)$.

The power density is then written as:

$$W_a(s) = \frac{1}{T} \int_0^T dt T(s, t + \tau) \partial_t C(s, t) \quad (5.24)$$

where $C(s, t)$ is the curvature and τ is a delay between the driving forces and their actuation. Since the system is dissipative and the torques are doing positive work on the system, the delay τ is expected to be small, but not necessarily zero.

After Fig. 5.3 and Fig. 5.2 we model the curvature as a traveling wave $C_w(s, t)$ modulated by an envelope $C_e(s)$:

$$\begin{aligned} C(s, t) &= C_e(s) C_w(s, t) \\ &= C_e(s) (C_0 \cos(\omega t - ks) + C_1 \cos(2\omega t - qs + \phi)) \end{aligned} \quad (5.25)$$

The envelope function is linear (Fig. 5.3), as we are interested in comparing the trend, we simplify its form to $C_e(s) = \lambda s + 1$.

Substituting the expressions for the curvature and the torques in Eq. (5.24), we obtain a semi-quantitative description of the work done:

$$W_a(s) = \pi (C_1 A_1 \cos(2\tau\omega) + C_0 A_0 \cos(\tau\omega)) (\lambda s + 1) . \quad (5.26)$$

We find that the power input increases towards the filament tip with the *same linear trend* of the dissipated power $D_v(s)$.

5.4. Concluding remarks

In summary, we have presented:

1. A quantitative description of the beating pattern of pinned human sperm,
2. A new steering mechanism.

The quantitative description of the tracked flagellum shows that, even if the beating

patterns between different cells are qualitatively different, they do have the similar eigenmodes (Fig. 5.24). This may allow, in the future, to classify the beating patterns of different cells based on eigenmodes themselves. We showed that most of the signal of the curvature can be decomposed on three eigenmodes that reproduce approximately 95% of the original data. This allows filtering the fluctuations that are not of biological origin, and to have a clear signal.

The beating frequency of a single cell is not constant and has a standard deviation of approximately $2Hz$, compatible with the standard deviation measured for *Chlamydomonas*[86].

We have shown that the standard deviation of the beating frequency and phase velocity of the single cell is smaller than the standard deviation of the population, and that it is not zero. This means that we can think the frequency as a regular Brownian quantity, fluctuating in a harmonic potential whose stiffness is defines the standard deviation. This detail can be relevant when thinking to the *ensemble* from which one has to sample from to simulate interacting spermatozoa.

We also suggest that the beating frequency and wave vector of human spermatozoa be correlated by a dispersion relation. At the moment, we observed this effect at sample level, and further investigation is required to sharpen the result and verify it on each cell individually.

The higher harmonic components of the beating pattern lead to steering forces. We have shown that the experimental data correlates accordingly to our simple model, and that simulations strengthens the causal relation between higher harmonics and rotation velocity. The simulations highlight also that a spontaneous curvature is generated by the rotating cell even when the driving torque is symmetric and does not model an average bending torque.

We would like to highlight that our numerical model of spermatozoon, built on the principle “the simpler the better”, reproduces the dynamics of the human sperm without fictitious or *ad-hoc* solutions. This may be not the case for the sperm cells of other species, for example: the very different neck-compliance of sea urchin spermatozoa requires a model with complex boundary conditions. Nonetheless, the current model allows a quantitative investigation of the dynamics of single, and the future

5. *Flagellar Beat of Pinned Human Sperm*

interacting, human sperm cells with approaches similar to the case of sedimenting filaments or more complex simulations [18].

Concluding, note that even if the fitting protocol reproduces qualitative and quantitatively the observed eigenmodes, the resulting planar dynamic is still strongly affected by the details of the relative position of the pinning point with respect to the head, and the length of the neck. We think this is understandable as we are fitting a subset of the information (the modes) to infer the full dynamics. In terms of differential equation, when the geometry is not precise, we are effectively simulating a system with boundary conditions that are different than the correct ones. Note also that the current protocol discards the last $\approx 5\mu m$ of the tracked flagellum. This is because tracking the flagellum tip is hard as the contrast goes down. We are currently working to improve our tracking and fitting protocols to be able to systematically measure the dynamics at the flagellum tip and base.

6. Autonomous Flagellar Beating

Autonomous beating means that the flagellum is not driven by a prescribed traveling wave, but rather, the wave is due to the emergent dynamic of a self-organizing mechanism. The emergent dynamics and self-organization are expected to be due to the coupling between the molecular motors and the sliding filaments inside the axoneme. The understanding of autonomous beating is a way to approach the difficult task of describing a system that is, intrinsically, not in its equilibrium condition as it swims in a viscous medium and in the competition to be the “first and only” one.

The flagellum burns ATP, in way is similar to steam engines that burn coal, and the flux of energy generates forces that are dissipated by the internal and external friction. The axoneme, however, is different from steam engines in the scales at which the energy is transformed to work: instead of a great central energy factory, ATP is hydrolyzed at very small scale by each single molecular motor, and the forces generated at the same small scale, create the big coordinated motion described in the previous analysis (chapter 5). We want to understand how the forces generated at small scale can propagate upward to larger scales in a coordinated way. As it is clear that the “out-of-equilibrium”-ness is the key to the answer, it is not, in itself, a sufficient answer.

Here we discuss some early results obtained investigating models for autonomous beating flagella. Our intention is not to discuss a point-like approximations, e.g. like the rowers model for cilia [86, 106, 107], but rather to address the realistic case of an active traveling wave due to sliding forces between parallel filaments of finite length and with asymmetric boundary conditions.

This chapter is divided in two main parts: we initially show the failed results we obtained by directly simulating the sliding model; then we show how we changed approach and tackled the problem from a more generic and top-down point-of-view.



Figure 6.1.: Simulation snapshots of two parallel filaments driven by the force-velocity relation in Eq. (6.1). Each filament is modeled as a semi-flexible filament and the relative sliding is hindered at the base (at the right side). We show that the simulation displays an unexpected buckling instability. In particular near the base of the flagellum the upper filament buckles, instead of releasing the energy by bending the bundle.

6.1. Early Failed Attempts

It is currently believed that the sliding mechanism that causes the bending can be mapped on a system with two planar and parallel semi-flexible filaments as rails (see section 2.5). In our first attempt we simulate¹ directly two semi-flexible filaments, parallel to each other with an adaptive triangulation that allows a smooth parallel sliding and constrained perpendicular displacement (Fig. 6.1 and Fig. 6.2). The stresses between the microtubules are modeled by effective the force-velocity relation of a two-state Brownian-ratchet-like system coupled to an harmonic potential via a common backbone [108]

$$f(v(s)) = \gamma v(s) - \gamma_3 v(s)^3, \quad (6.1)$$

where $v(s)$ is the relative velocity between the filaments at arclength s , and $\gamma > 0$ and $\gamma_3 > 0$ characterize the energy input and the stall force of the molecular motors. In Ref. [108], the backbone driven by Eq. (6.1) and coupled to a harmonic potential undergoes a Hopf bifurcation and displays a (active) periodic motion. The intuitive idea is that as the filaments are allowed to bend and are clamped at one side, the system develops a traveling wave from the base. This, however, never happens in our simulations.

We have seen, instead, that even for very flexible filaments the pushed microtubule buckles near the base (Fig. 6.1), where the active stress is at its maximum. In Fig. 6.2

¹The simulations shown in this section, are thermalized with MPC [102].

we show that even in the case of stiffer filaments, the buckling instability appears before the bending instability, and in all cases no traveling wave is generated in the remaining part of the filament.

After an extensive scanning of the parameters we did not find a parameters set that corresponds to traveling waves. The biggest issue being that there is no general theoretical framework to understand and model mechanical dissipative systems and wave-like self-organized states. Hence, we have no guidance nor intuition to understand what is wrong with the current, bottom-up, approach.

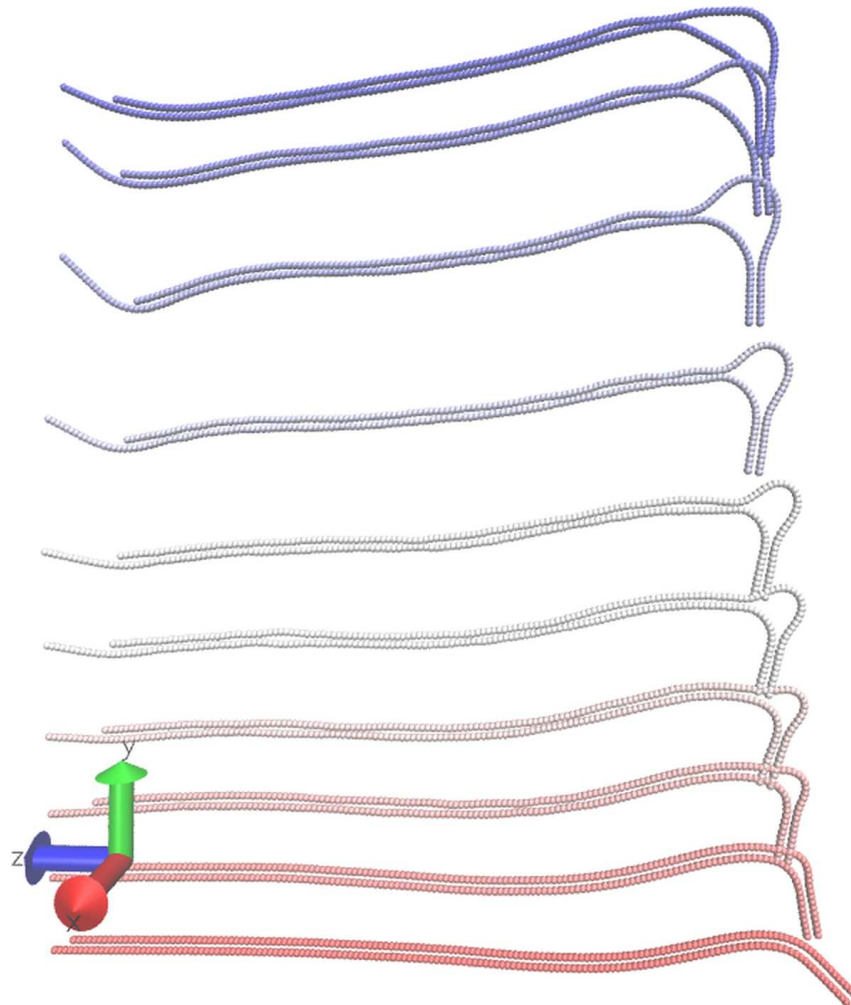


Figure 6.2.: Snapshots of the evolution of the buckling instability at the base (red to blue). The upper filament is pushed towards the base (at the right side) on the contrary to the lower filament that is pulled away. Because of the hindered sliding at the base, the stress is not constant along the filament. In particular the stress accumulates near the base where it is released as a buckling of the upper filament, instead as of a bending of the bundle.

6.2. Dynamic Ginzburg-Landau Approach

We can see the beating axoneme as the result of a unknown pattern-forming mechanism. We want to understand what possible class of models can reproduce the observed beating pattern. To this end, we apply some concepts patten formation in dissipative systems [24] to our mechano-chemical system: the axoneme. The main difference being then mathematical only, as the generic non-equilibrium statistical mechanics developed for chemical reactions is valid for general degrees of freedom, too.

We simplify the problem and describe the flagellum as a single semi-flexible filament driven by generic internal forces, with short-range hydrodynamics and only in the limits of small amplitudes. While this approach is quite minimalistic compared to the other works [44, 46, 75] (see section 2.5), we aim at understanding the key features that more detailed and sophisticated models need to satisfy, with the ultimate target to design simulations of interacting swimmers with full hydrodynamics similar to the works of Refs. [18, 35, 79]. We then study the linear stability of the normal modes, solve numerically for the non-linear terms and begin to address the dynamical response to external perturbations.

Some traits of the model can be expected already from the basis of generic and simple physical considerations. Since we are going to investigate the active periodic motion of the filament in a dissipative fluid, we are interested in models that admit limit cycles for all excited modes [24, 109]. From a thermo-dynamic point of view this means that an energy flux will correspond to the solution. Microscopically, energy, e.g. in the form of ATP molecules, is consumed by the motor proteins and dissipated by both internal dissipation and the viscous forces of the fluid. From the mathematical point of view the instability is due to the positiveness of the eigenvalues of some modes. The model needs to be not linear to cap the growth of the unstable modes.

We distinguish the system in two components: the elastic filament and the active forces. The equation of motion of a semi-flexible filament is discussed in section 2.3; when we include the shear forces $f(s, t)$ we obtain [44, 65]:

$$\xi_{\perp} \partial_t h = -\kappa \partial_s^4 h + \tilde{c}_t \partial_s f, \quad (6.2)$$

6. Autonomous Flagellar Beating

where \tilde{c}_t is a control term that couples the internal shear forces with the filament.

The shear forces are defined by the differential equation:

$$\partial_t f = G(\tilde{\mu}, f, \{\partial_s^n f\}, h, \{\partial_s^n h\}, \{p_i\}), \quad (6.3)$$

where $\tilde{\mu}$ plays the role of the critical parameter, p_i are other parameters, and G is a unknown function of h , f and their gradients. In principle G can have any functional dependence on f and h , however it can depend only on derivatives of h because of translational symmetry. Observing, also, that the wavelength of spermatozoa is long, $\lambda/L \sim O(1)$, as first attempt, we expand G near the critical threshold $\tilde{\mu}_c = 0$, where also the stationary amplitude of f and h is expected to be small. Since we are looking for periodic solutions of h and f , we find an equation that strongly resembles the Ginzburg-Landau model, or the normal form of the Hopf bifurcation [24, 110–112]:

$$\partial_t f = \tilde{D} \partial_s^2 f + \tilde{\mu} f - \tilde{n}_l f^3 + F(h) \quad (6.4)$$

where the parameter \tilde{D} is an interface term and $F(h)$ is the still-unknown control mechanism that couples forces and filament.

Note that, *a priori*, we cannot justify the presence of the interface term \tilde{D} . It models possible small-scale coordination between motors; proposed mechanisms are, e.g., the sliding of the filaments [76], the effective internal hydrodynamic flow [113] or the geometric clutch [47].

We expect that every biological mechanism that generates the sliding stresses has a maximum output force or power: e.g., molecular motors are known to possess a precise stall force [1, 114] and we see in Fig. 5.15 that the dissipated power is roughly the same for all the experimental data we analyzed. The non-linear term $-\tilde{n}_l f^3$ can be thought as a mathematical formulation of these limitations since it limits the internal stresses to the maximum value $f^* = \sqrt{\mu/\tilde{n}_l}$. This is a standard approach that allows thinking in terms of Hopf normal form; in biological systems other non-linear mechanisms may be involved, but there are no standard techniques to study their effects and further investigations are needed gain some understanding.

Few mechanisms have been proposed as control mechanisms between filament

conformation/dynamics and internal forces; here we focus on three of them:

Sliding control	$F(h) = \partial_s h(s, t)$
Sliding velocity control	$F(h) = \partial_t \partial_s h(s, t)$
Curvature control	$F(h) = p \partial_s^2 h$

The polarization parameter p describes the intrinsic polarization of microtubules [1] and enforces the correct symmetry of the equations of motion. Note that in the literature the curvature-control feedback is usually associated to the model proposed in Ref. [38], that is different from our as the curvature feeds back to the bending torques, not to the sliding forces.

In the next section we perform a linear stability analysis for each of the three models to understand which models describe traveling waves, in the subsequent sections, instead, we study the numerical solution of Eq. (6.2) and Eq. (6.4), and finally we study the dynamical response by perturbing the filament position with external forces.

6.3. Linear theory

6.3.1. Eigenvalues and model selection

The equation of motion of a semi-flexible filament (Eq. (6.2)) is written in dimensionless units when length is measured in units of the filament length $x = sL$ and time in units of the elasto-hydrodynamic time $t = \tau \frac{\xi_{\perp} L^4}{\kappa} = \tau \omega_c$. With this choice, the force unit is κ/L^2 and the parameters are $D = \frac{\xi_{\perp} L^2}{\kappa} \tilde{D}$, $\mu = \frac{\xi_{\perp} L^4}{\kappa} \tilde{\mu}$ and $c_t = \frac{\xi_{\perp} L^5}{\kappa^2} p \tilde{c}_t$.

The linear terms allow deep investigation of each proposed model and to select the more convenient. In the same spirit of Ref. [115], we rewrite the linear terms as a linear operator L over the modes $f_q(s)$ and $h_q(s)$:

$$\begin{aligned} \partial_{\tau} \begin{pmatrix} f_q \\ h_q \end{pmatrix} = L \begin{pmatrix} f_q \\ h_q \end{pmatrix} &= \begin{pmatrix} D \partial_s^2 + \mu & F \\ c_t \partial_s & -\partial_s^4 \end{pmatrix} \begin{pmatrix} f_q \\ h_q \end{pmatrix} \\ &= \begin{pmatrix} -D q^2 + \mu & F_q \\ i c_t q & -q^4 \end{pmatrix} \begin{pmatrix} f_q \\ h_q \end{pmatrix}. \end{aligned}$$

6. Autonomous Flagellar Beating

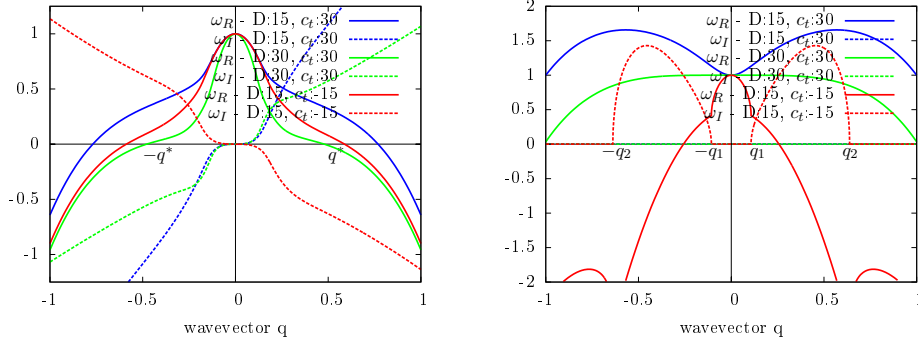


Figure 6.3.: Plot of the real and imaginary part of the eigenvalues ω_q^+ for curvature-control (**left**) and sliding-velocity control (**right**). Same colors correspond to same parameters D and c_t - solid (dashed) lines correspond to the real (imaginary) part ω_R (ω_I). (**Left:**) The green line corresponds to an increased interface coefficient D . In red we decreased and inverted the control parameter c_t to show that the frequency ω_I is a odd function: this means that the wave velocity for positive and negative q has the same direction. Observe that only the modes $|q| < q^*$ are excited. (**Right:**) The imaginary eigenvalue (dashed lines) is either zero for all values of the wave-vector, or for a finite set when $|q| < q_1$ (for some values of the parameters also when $|q| > q_2$). This represents an unwanted, non-periodic behavior.

Where the modes are chosen to simultaneously diagonalize all differential operators in the matrix

$$f_q(s) \approx \exp(iqs), \quad h_q(s) \approx \exp(iqs) \quad (6.5)$$

with $q \in \mathbb{R}$ the wave-vector and $s \in [0, 1]$. This basis have not to be confused with the eigenfunctions of the operator L itself. Eq. (6.2) and Eq. (6.4) are then reduced to the much simpler eigenvalue problem $\omega_q = T_q \pm (T_q^2 - 4D_q)^{1/2}$, where T_q and D_q are the operator trace and determinant respectively. We find convenient to rewrite the eigenvalues as:

$$\begin{aligned} \omega_q &= \omega_q^R + i\omega_q^I \\ \omega_q^R &= T_q \pm \rho \cos \theta \\ \omega_q^I &= \pm \rho \sin \theta \end{aligned} \quad (6.6)$$

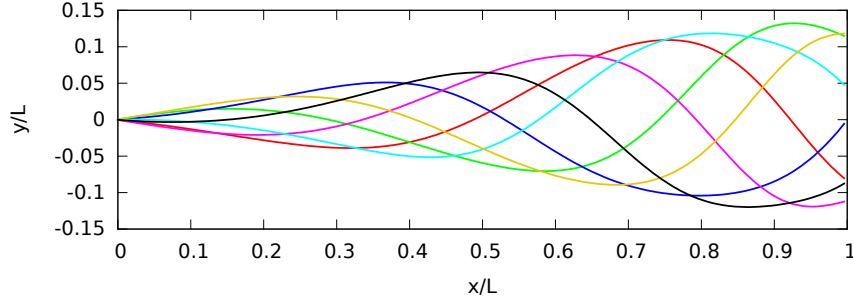


Figure 6.4.: Plot of the beating pattern for $D = 15$ and $c_t = -30$. The wave propagates from left to right as consequence of the symmetry $\omega_I(q) = -\omega_I(-q)$ and $c_t < 0$. If $c_t > 0$ the wave would propagate from right to left, with small differences on the overall shape, but very similar wavelength and frequency.

where $\rho e^{i\theta} = \sqrt{T_q^2 - 4D_q}$ and the superscript R or I stand for real or imaginary part. Depending on the feedback mechanism, the determinant D_q can be either real or complex: in particular, the determinant is complex if $F(h)$ contains only even derivatives. When real, the eigenvalues behave as in regular harmonic oscillator: if D_q is positive the imaginary part is null and the real part is given by the trace only. The angle θ is 0 in the first case, and $\pi/2$ in the second. When D_q is complex, instead, the square root has always both a real and an imaginary part, that translates to θ being continuous in the interval $-\pi/2 < \theta < \pi/2$.

When $c_t = 0$ the dynamics is independent from the functional form of $F(h)$, the eigenvalues are either both negative (if $\mu < 0$) or one negative for all wave-vectors ($Re\omega_q^- \sim_{q \rightarrow 0} -2q^4$) and one positive for $q < q^* \approx \sqrt{\mu/D}$ ($Re\omega_q^+ \sim_{q \rightarrow 0} -q^2D + \mu$). This means that despite the term μf excites all modes, only the modes $q < q^*$ are actually being excited.

To discriminate the fundamental features of each model, we study now only the unstable solutions and set $\mu = p = 1$ and $c_t \neq 0$.

We find that, in the case of sliding-control and sliding-velocity control mechanisms the determinant is real, hence $\omega_q = T_q \pm i\omega_I(q)$: this describes the usual superimposition of two waves, traveling with opposite wave velocities; a spontaneous symmetry-breaking mechanism or the boundary conditions determine which direction prevails [110]. We also find that there are always eigenvalues with positive real

6. Autonomous Flagellar Beating

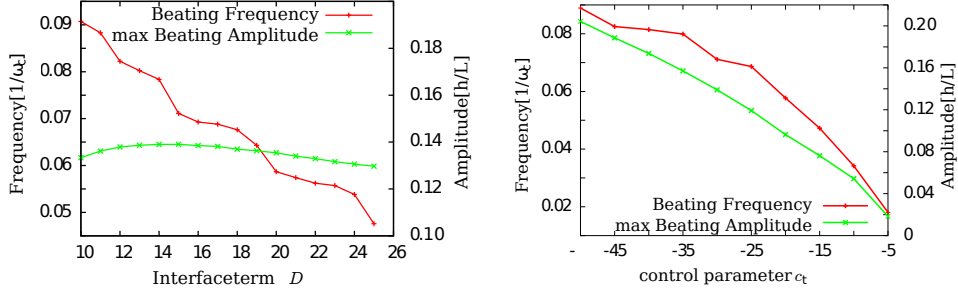


Figure 6.5.: Plot of beating amplitude and frequency for different values the control parameters D (left panel) and c_t (right panel).

part but no imaginary component for small q whatever the choice of the parameters c_t and D (Fig. 6.3(right) for an example). In principle this is not a problem because the modes cannot grow indefinitely as they are constrained by the non-linear term. However, it is not a desirable feature of the model.

For the curvature-control mechanism, on the contrary, we find that the determinant is complex and $\omega_R^-(q) \leq 0$ for all wavelengths. The eigenvalue $\omega_R^+(q)$ is positive when $|q| \lesssim q^*$ (Fig. 6.3)(left). The phase is approximately $\theta \sim_{q \rightarrow 0} -c_t q^3$, hence the frequency $\omega_I(q) = \rho \sin \theta$ is an odd function of both the wave-vector and the parameter c_t . This means that the phase velocity ($v_q = \omega_I(q)/q$) of the modes $+q$ and $-q$ is the same, hence the system can break the left-right symmetry just by changing the sign of the control parameter c_t (or of the polarization p). This is not a spontaneously broken symmetry as the left-right direction is embedded directly in the model by the microtubules' polarization.

Note that, on the contrary of the well-known Complex Ginzburg-Landau equation[111], there is no oscillatory motion associated to the $q = 0$ mode. Another important difference is that, because of the odd-derivative, the Fourier modes are not discrete although the filament has finite length. This mimics the fact the experimental wave-vectors seem not to be dependent on the axoneme length.

6.4. Nonlinear model

We investigate further the curvature-control model as all positive eigenvalues also have a non-trivial imaginary part, meaning that at each unstable mode corresponds a limit cycle, whatever parameters set. Because of the non-linear term the solution is not a mere superimposition of modes, but a mix of the excited modes [111]. We integrate numerically [116] the model to verify if it reproduces a beating pattern. Let us rewrite the equations of motion for $\mu = p = 1$:

$$\begin{aligned}\xi_{\perp}\partial_t h &= -\kappa\partial_x^4 h + c_t\partial_x f \\ \gamma_f\partial_t f &= D\partial_x^2 f + f - n_l f^3 + \partial_x^2 h.\end{aligned}\quad (6.7)$$

To compare the results with our previous analyses (chapter 5), we impose pinned boundary conditions:

$$\begin{aligned}h(s=0) &= \partial_s h(s=0) = \partial_s^2 h(s=L) = \partial_s^3 h(s=L) = 0 \\ f(s=0) &= \partial_s f(s=0) = 0\end{aligned}$$

where length, stiffness and viscous drag are $L = 30$, $\kappa = 1$, $n_l = 80$ and $\xi_{\perp} = \gamma = 1$.

In Fig. 6.4 we plot 7 frames that show how the wave grows from left to right with the same linear envelope measured for Human sperm (Fig. 5.3). In Fig. 6.5 we plot the frequency ω and beating amplitude h_{\max} versus D (left panel) and c_t (right panel). Since the displacement h is due to the derivative of f we expect that the interface term D penalizes the beating amplitude, however this is not the case: the amplitude is approximately constant (green line), the frequency decreases (red line), instead.

The beating frequency, amplitude and the stroboscopic plot do not represent a complete set of features. In particular, if ones target is to match a particular biological systems the non-linear interaction between the modes leads to non-intuitive results: we find that when $c_t < -40$ the wave develops a steep propagation front, while when D is small the down-stream side shows curly profiles but smoother fronts. This means that a careful analysis is needed to map the current model to the experimental

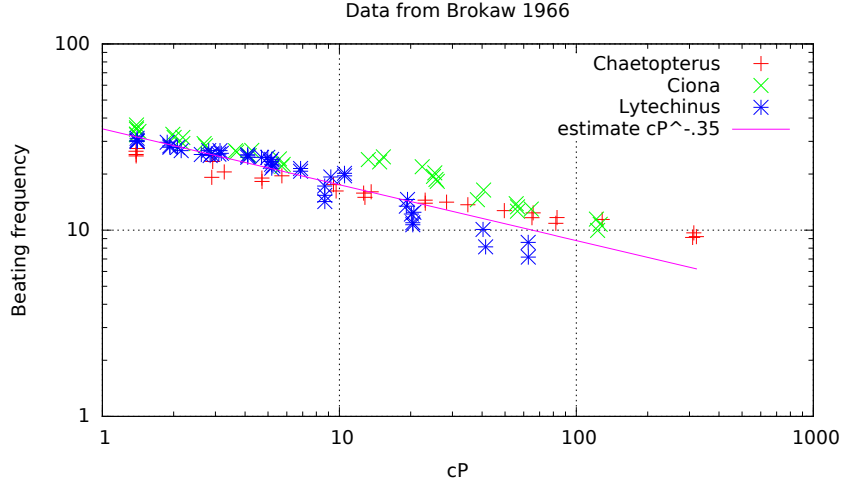


Figure 6.6.: Plot of the data reported in Ref. [117]. In the original work the trend is hard to judge because the three data series are plotted in three separate plots in a semi-log plot. Here the three series are plotted together in a log-log plot to show the qualitative trend. The purple line corresponds to $\omega = \eta^{-0.35} + 35$.

beating patterns analyzed in chapter 5.

6.4.1. Internal and external viscous dissipation

The effect of viscosity on the beating frequency of spermatozoa of some invertebrates (*Ciona*, *Chaetopterus*, and *Lytechinus*) has been investigated in Ref. [117] reporting that the frequency has a power law dependence on the viscosity with exponent ≈ 0.35 (Fig. 6.6). Eq. (6.7) has two viscosity-like terms: ξ_{\perp} and γ_f and numerical integration confirms that the frequency has the simple (expected) dependence $(\xi_{\perp} + \gamma_f)^{-1}$ (Fig. 6.7(left)). At the same time, the beating amplitude decrease and the beating pattern is strongly affected. In the current parameters' regime the model is more sensible to variations of the viscosity than the experimental system under examination. It may be that the regime of our simulations, dominated by the “external drag” $\xi_{\perp} \gg \gamma_f$, does not represent the biological one. But, we can also advance the hypothesis that the model is incomplete, and that in the real system the internal dissipation dominates over the external one, making the system more robust against certain types of perturbations.

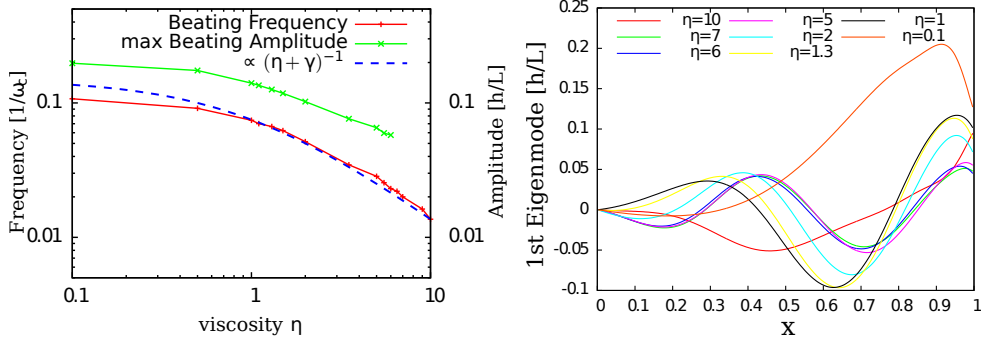


Figure 6.7.: Plots of the beating frequency and amplitude (**Left panel**) and of the first eigenmode (**Right panel**) for increased values of viscous drag ξ_{\perp} . As the viscosity increases, the active beating amplitude and frequency decrease faster than in the experiments.

We think to two sources of internal viscosity. The effective internal friction γ_f models the time needed by the conformational changes of the motor proteins to take place as consequence of ATP hydrolysis or of external forces. We can, in addition, consider the effect of a viscous-elastic resistance between the sliding filaments (due, e.g., to crosslinks): the equation for h becomes than $\xi_{\perp} \partial_t h = -\kappa \partial_x^4 h + c_t \partial_x f + \gamma \partial_t \partial_s^2 h + k \partial_s^2 h$, where the term $\partial_s^2 h$ is the curvature force induced by the shear displacement [64]. When $\gamma \gg \xi_{\perp}$ the internal dissipation dominates and we rewrite the equation in terms of the curvature $z = \partial_s^2 h$ only:

$$\begin{aligned} \gamma \partial_t z &= \kappa \partial_x^2 z - c_t \partial_x f - kz \\ \gamma_f \partial_t f &= D \partial_x^2 f + f - n_l f^3 + z. \end{aligned} \quad (6.8)$$

The corresponding eigenvalue problem has the same structure of the original model, hence the same solutions are expected.

Concluding this note: we expect that the internal dissipation be one way that the biological system has to tune the response of cilia and spermatozoa to external perturbations as can be the change of rheological properties of the medium, although at the moment this is just a speculative hypothesis and more experimental evidence has to be provided.

6.4.2. Dynamical behavior

In the past decades much attention was devoted to the beating pattern of spermatozoa, on their efficiency and hydrodynamics [10, 14, 32, 118], with some attention to the feature that distinguish them the most from non-biological systems: the ability to adapt and change behavior as response to external stimuli [40, 47, 117]. It is observed that spermatozoa dynamically tune their beating frequency as they approach each other, *Chlamydomonas*, instead, seems to be less interested in this kind of entrainment; in the latter case the behavior depends on many experimental factors that are currently being addressed².

Our model allows a systematic investigation along this direction. We choose to study the response of the beating pattern to two types of perturbations: a fixed harmonic tube and a periodic external force .

As reported in Ref. [117], we expect that many observables that characterize the beating pattern be affected, namely the beating frequency, the wavelength, the amplitude and the principal eigenmodes. To measure how the beating shape changes in response to the external forces, we decompose the displacement in its normal modes $\phi_n(x)$, as defined in the chapter 3. For unperturbed beating, we find that two modes always contribute at, at least, 90% of the signal- We are doing an “effective” numerical phase reduction of the problem, as introduced analytically in Ref. [84]. The beating frequency is estimated from the Poincaré map of $\chi_1(t)$ vs $\chi_2(t)$ [85]. This method is more robust than Fourier decomposition because we are not interested in the different Fourier components but only on the period of the slowest mode.

Harmonic Tube

We constrain the beating displacement in a harmonic potential:

$$\begin{aligned}\xi_{\perp} \partial_t h &= -\kappa \partial_x^4 h + c_t \partial_x f - kh \\ \partial_t f &= D \partial_x^2 f + f - n_l f^3 + \partial_x^2 h,\end{aligned}\tag{6.9}$$

²Private communication with groups in TU Delft and Cambridge.

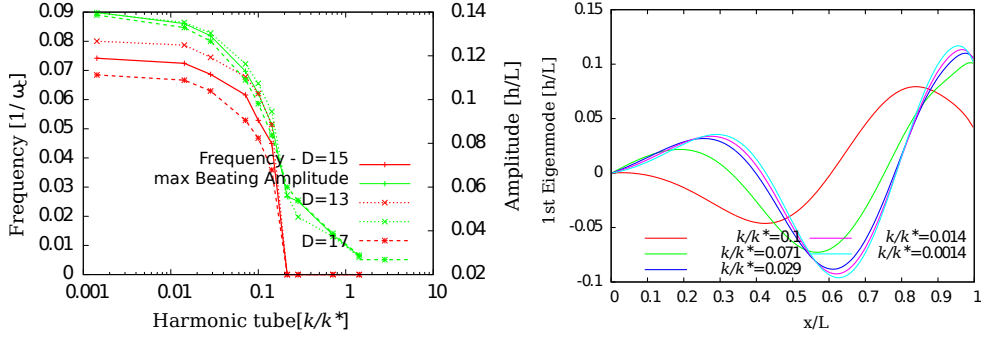


Figure 6.8.: Self-organized beating inside a “harmonic tube”. **(Left panel):** Plot of beating frequency and amplitude versus confinement strength. Note that as $k \geq 0.1$ the filament does not show self-organized beating. **(Right panel):** The principal eigenmode for $k < 0.1$ shows that as the filament was squeezed by the harmonic potential, it adapted its wavelength. In this plot, $D = 15$.

where k is the potential strength. We measure the force strength k in units of the maximum internal force $k^* = c_t \frac{\partial_x f_{\max}}{h_{\max}}$, where the maximum is evaluated from the unperturbed case (Fig. 6.4): $k^* h_{\max}$ is than an estimate of the maximum force exerted by the internal forces. We find that, on the contrary to the case of prescribed internal forces, both beating amplitude *and* wavelength are adapted to the confinement (Fig. 6.8(right)). In Fig. 6.8(left) we plotted the variation of beating frequency and amplitude (h_{\max}/L) for different strengths k/k^* . Frequency and amplitude decrease as consequence of increasing work against the potential, until the movement ceases for $k/k^* = \tilde{k} \sim 0.1$. Note that \tilde{k} is independent of D (Fig. 6.8(left)). Ideally, this setup allows estimating the strength of the internal forces from the confinement, providing an independent and complementary measure to the results of the fitting protocol proposed in section 5.2.4.

6. Autonomous Flagellar Beating

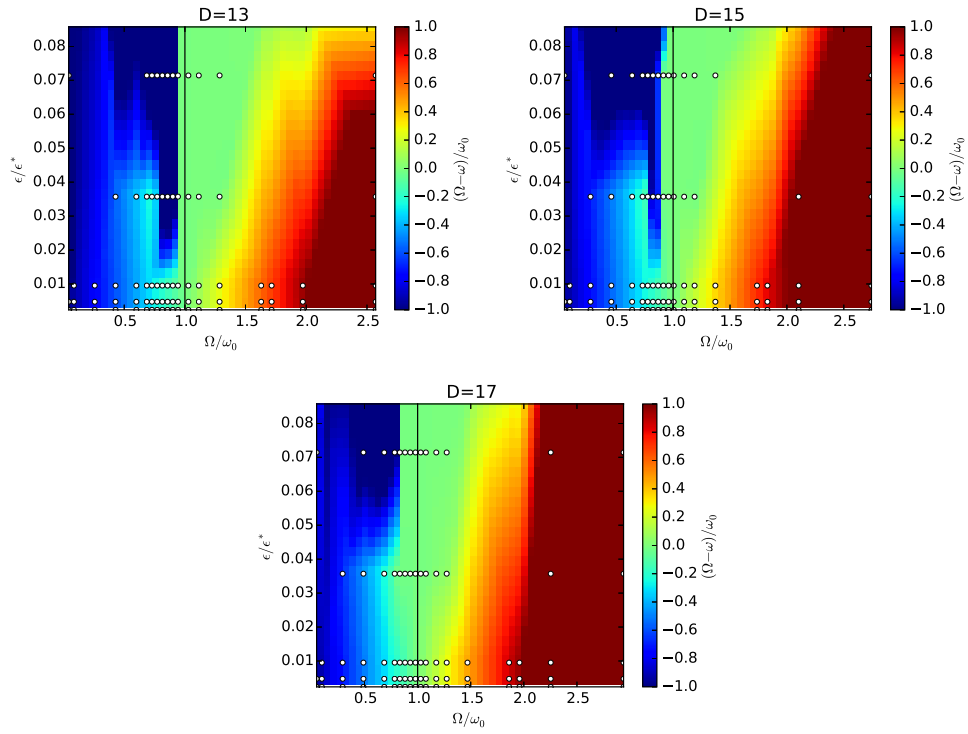


Figure 6.9.: Plot of the frequency difference $\Delta\omega = (\Omega - \omega)/\omega_0$ when the system with natural frequency ω_0 is forced with the periodic force $\epsilon \sin(\Omega t)$ as the intensity ϵ and the forcing frequency Ω are varied. The green triangular area corresponding to $\Delta\omega \approx 0$ shows that the system is entrained by the external forcing. White dots corresponds to simulations whose first two eigenmodes summed up to 90% of the signal, heat-map is obtained from linear interpolation.

Periodic Forcing

In the second case the filament is forced by an external periodic force along the direction normal to the filament:

$$\begin{aligned}\xi_{\perp} \partial_t h &= -\kappa \partial_x^4 h + c_t \partial_x f + \epsilon \sin(\Omega \tau) \\ \partial_t f &= D \partial_x^2 f + f - n_l f^3 + \partial_x^2 h\end{aligned}\tag{6.10}$$

where ϵ is the force strength and Ω its frequency. We measure the force in units of $\epsilon = c_t \partial_s f_{\max}$ computed from the unperturbed system as done for k^* .

It is known that non-linear oscillators display entrainment when forced by a (weak) external periodic force [83]. In Fig. 6.9 we show that this is indeed the case for our “autonomous sperm”: we plotted the frequency difference $(\Omega - \omega)/\omega_0$ between the forcing frequency and the beating frequency *versus* the force strength ϵ/ϵ^* and the forcing frequency Ω/ω_0 (with ω_0 the natural beating frequency of the unperturbed system). The force strength is always small enough to avoid driving, chaotic behaviors and loss of self-organized beating; in practice, we check that 90% of the shape of every simulation is described by just two modes.

In Fig. 6.9 we recognize the well-known shape of the Arnold-Tongue and of the entrainment plateau that surrounds Ω/ω_0 ; it is curious to observe that entraining is difficult at frequencies lower than the natural one. By increasing the parameter D we observe that the synchronization plateau (the green cone) shrinks. We may think that D defines an effective stiffness to entraining, that has nothing to do with the bending stiffness κ . Unfortunately, further numerical investigations, without a solid theoretical background would not help in understanding the role of the parameters, and we postpone this investigation for future works.

6.5. Discussion

In the first part we showed that direct simulation of the 2D sliding model filament displays two kind of unexpected behaviors:

1. lack of any wave-like pattern

2. formation of buckling instability near the base.

Such a direct approach hindered our vision of the problem because of the many technical details involved in the simulations; hence we turned to a simplified approach, in which the bundle is described as an effective filament. The second problem is thus circumvented by removing the degrees of freedom needed by the buckling instability.

The simplified approach allows a top-down development of a model for active traveling waves in a one dimensional material. Linear stability analysis shows that of three possible feedback mechanisms two, namely the sliding control and sliding-velocity control, are less likely to be as they have unstable eigenvalues not connected with oscillatory motion. Because of the variability of the biological environment and of the resilience of spermatozoa in the most disparate conditions, we expect that any representative model has no ill-defined behaviors. From this point of view, the curvature-control mechanism seems more reliable, and numerical investigation allows to asses that the traveling wave is smoothly controllable by the parameters D , c_t and p , and has a qualitative match to the observed shapes. In this model we break the symmetry via the polarization parameter p , as the real microtubules polarize the axoneme with respect to the traveling direction of motor proteins [1].

Focusing on the curvature control model, we begin to investigate how an active material reacts to external perturbations. We have shown that, not only the beating frequency is affected, but also the beating amplitude and wave-vector change in response to external stimuli. It is of great interest now to test how the biological systems behave under similar stresses, and to refine the proposed concepts until we reach a quantitative agreement between data and model.

It is also of primary relevance to extend the model to a planar filament model than can reproduce the experimental recording. We should not forget that the similarity between the spermatozoa axoneme and cilia axoneme poses the question whether this model can reproduce the cilia beating. This would be for sure an important step towards the possibility to discuss experimental measures that are, at the moment, not done on spermatozoa, such as the beating noise and synchronization/slip phases.

7. Concluding Summary

The elasticity and dynamics of semiflexible filaments, their hydrodynamic interactions, and their active motion, play a very important role in biological systems at the cellular level, but also in technological applications such as polymer suspensions under flow and the construction of micro-robots. A detailed understanding of such systems is, therefore, essential.

We investigated the dynamics and stability of semi-flexible filaments exposed to an external homogeneous field and interacting only via hydrodynamic fluid fields. Due to the competition between hydrodynamic interactions and bending stiffness, the appearing dynamical behavior is different than for entropy-dominated polymers or interacting rods. We inspected the conformational changes projecting the simulated shapes on the modes of the corresponding partial differential equation. With this tool, we found two new dynamical transitions that excite non-planar shapes that lead to drift and helical settling trajectories. Finally, we have demonstrated that three filaments display an unexpected periodic dynamics even at field strengths far weaker than expected by the analysis of the one and two filaments.

We presented, then, a way to decompose the beating shape of an isolated and pinned human spermatozoon in a basis of three empirical eigenmodes computed from the flagellum curvature. Not all eigenmodes are equally important. At each eigenmode, a corresponding eigenvalue is associated to represent its importance. The first two eigenmodes describe the periodic motion, their eigenvalues are very similar. Although the beating pattern is different from cell to cell, the eigenmodes are universal among our sample. The standard deviation of the beating frequency of the single cell is shown to be comparable to the variance found for beating cilia of a quite different microswimmers, green alga the *Chlamydomonas*. Surprisingly, the data suggest that the wave vector and the beating frequency are not freely chosen

7. Concluding Summary

by each cell; we find instead that there is a linear dispersion relation.

We developed a sperm model to quantitatively match the observed eigenmodes, allowing insight into the internal beating dynamics. This is a novel approach, as previous analyses were restricted only to the observable kinematics, unable to infer the internal forces, without using micro-manipulation techniques. The model represents the sperm as a semi-flexible filament activated by a traveling wave of bending torques with constant amplitude. The simulated beating pattern matches the empirical eigenmodes, without the need to explicitly model the left-right asymmetry as the beating amplitude increases towards the flagellum tip.

We discovered a new steering mechanism based on a beating pattern with higher harmonics. The theoretical prediction matches with the experimental observations. Simulations with bending torques given by the sum of two traveling waves reproduce the observed beating pattern and rotation velocity. The model highlights also that, although the bending torque has zero average value, the often observed average curvature is spontaneously generated.

Finally, we presented a model in which the beating pattern develops as an active response to the filament shape. Because of the variability of the biological environment and of the resilience of spermatozoa in the most disparate conditions, we expect that any representative model of active beating should have no ill-defined behaviors. We analyzed different functional forms for the active forces, and showed that curvature-control feedback mechanism seems more suited as each mode of the partial differential equation with positive eigenvalue has also an imaginary eigenvalue, which implies that the final shape is smooth and periodic.

In the previous study with given bending torques, the beating pattern parameters are externally fixed and cannot adapt to a mechanical perturbation. The active model instead shows a more natural and intuitive behavior. We highlighted that the model forecasts a change in beating frequency, wavelength and amplitude as it is squeezed by a harmonic potential. For the investigated parameters, the beating ceases when the external potential becomes stronger than 10% the internal maximum forces. We also showed that entrainment of the beat with an external periodic perturbation can occur, and underlined that the entrainment-stiffness can be tuned by changing the

internal driving parameters, while leaving the mechanical bending rigidity unaltered.

8. Outlook

The three main topics of this thesis are linked by the common idea of understanding and modeling the dynamics of slender filaments in a viscous fluid, like for the human spermatozoon. The results of each topic are interesting by their own as they allow deepening and widening our knowledge of that particular topic. But, all together, we expect to merge the concepts and models into a joint framework which allows the investigation of human spermatozoa and other microswimmers quantitatively.

Now, it is possible to simulate the motion of a human sperm with realistic shapes and forces. Matching quantitatively the generated forces and flow fields, we expect to reproduce hydrodynamic interaction between swimmers and obstacles. Another possible scenario is the study of swimming trajectories of interacting spermatozoa and the influence on the chemotactic efficiency. At the same time, the intensity and stability of the hydrodynamic attraction can be carefully assessed and compared to experimental observations.

An important aspect of research in physics is the transfer of the developed techniques and concepts to different contexts. We have developed a way to quantify and analyze slender shapes, but our technique is not limited to sperm cells data. It is possible, in principle, to apply the same protocol to other swimmers, like *Chlamydomonas*, or to extend the technique to bi-dimensional objects like cells. The classification of cell-shapes via empirical cell-eigenmodes can improve, e.g., the current estimation of anomalous cells as done to assess the presence of cancer cells¹.

We proposed a model for a generic autonomous beating pattern. It is of great interest now to test how the spermatozoa behave when perturbed with external forces, e.g. generated by flows, and to refine the proposed concepts until we reach a quantitative agreement between experiment and model. The same modeling concepts

¹Suggested by Prof. R. Austin.

8. Outlook

applied to cilia can deepen our understanding on cilia metachronal waves and, in principle, to contribute to the studies of related diseases.

We conclude by highlighting the importance of further investigation to deepen our understanding of autonomous beating models, as they represent a simple prototype of an active nonlinear material that may lead to technological applications once we are more acquainted with the underlying concepts. In particular, we would like to stress two directions, the inclusion of noise, as at small sizes it is an important player, and the effect of non-linear contributions on the system response.

Appendices

A. Adaptive time-step Velocity-Verlet

It is a standard approach of molecular dynamics to integrate the equation of motion with Velocity-Verlet algorithm [119, 120]. It is simple, reversible and energy conserving [121].

To clarify how we changed the algorithm, let's start by recalling the regular Velocity-Verlet. The algorithm to update the configuration and velocity $\{\mathbf{x}_i, \mathbf{v}_i\}$ from time t to time $t + \Delta t$ is, essentially, made of four steps:

1. Half-step for the velocities: $\mathbf{v}(t + 1/2\Delta t) = \mathbf{v}(t) + \frac{1}{2m}\mathbf{f}(t)\Delta t$
2. Full-step for the positions: $\mathbf{x}(t + \Delta t) = \mathbf{x}(t) + \mathbf{v}(t + 1/2\Delta t)\Delta t$
3. Update of the forces to $f(t + \Delta t)$
4. Second half-step for the velocities: $\mathbf{v}(t + \Delta t) = \mathbf{v}(t + 1/2\Delta t) + \frac{1}{2m}\mathbf{f}(t + \Delta t)\Delta t$

Note that the algorithm to update the forces is not specified by the Velocity-Verlet scheme. When the forces do not depend on the velocities (e.g. for bonds and bending energies) there are no possible misunderstandings. On the contrary, when the forces depend on velocity, like in the case of viscous forces, the protocol may be confusing as the velocity is known at half-a-step before – the Oseen tensor adds another layer of complexity because the background flow is generated by the conservative forces. Here we report the scheme we used to update the forces (step 3 of Velocity-Verlet algorithm):

1. Update the conservative forces:
 $\mathbf{f}^C(t) \rightarrow \mathbf{f}^C(t + \Delta t)$
2. Update the background flow field due to the new forces:
 $\mathbf{u}_i(t + \Delta t) \propto \sum_{i \neq j}^N H(i, j)\mathbf{f}_i^C(t + \Delta t)$

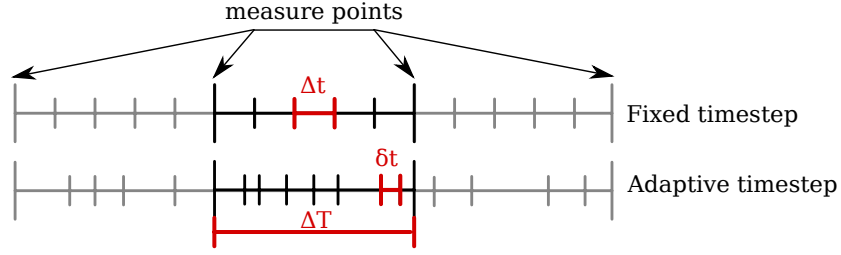


Figure A.1.: Illustration of the concept of adaptive time-stepping.

3. Update the dissipative forces:

$$\mathbf{f}^D(t + \Delta t) = -\gamma_0 (\mathbf{v}(t + 1/2\Delta t) - \mathbf{u}(t + \Delta t)).$$

This algorithm is stable as long as the time-step is short compared to the characteristic time-scales of the dynamics. Selecting a good time-step is crucial to correctly integrate the equation of motion while running at a reasonable speed. In our projects it is not always possible to estimate manually the required time-step either because the forces generated by the Oseen tensor are hard to estimate, or because the simulation is embedded in a fitting routine that changes the parameters by few orders of magnitude.

One way to solve this problem is by integrating at constant error, instead of integrating at constant time-step.

We can think then to encapsulate the Velocity-Verlet inside an algorithm that decides the appropriate time-discretization needed to update the system configuration from time t to time $t + \Delta t$ using as many steps $\delta t \leq \Delta T$ as needed to satisfy a given accuracy δ [122, 123] (Fig. A.1). This approach introduces two time partitions: the one of the simulation ΔT and the one of the molecular dynamics δt . In different context, a similar approach is used to couple molecular dynamics simulations with MPC simulations [78]; the major difference being that the inner partition is not fixed but computed on-the-fly (Fig. A.1).

The algorithm can be summarized as follows:

1. Compute the expected error: $\text{Err}(t) = (\Delta t_{MD})^2 \max_i f_\alpha(t)$
2. Compute the new proposed time-step as: $\delta t^p = \max(\delta t_{min}, \beta \sqrt{2\delta \max_i f_\alpha(t)})$

-
3. Accept the shorter timestep if $\delta t^p \leq \gamma \delta t$ and $Err > \delta$.
 4. Perform the Velocity-Verlet algorithm with the given δt .
 5. Update current time to $t = t + \delta t$.
 6. If $Err < \delta/2$ accept a longer timestep $\delta t = \min(\min(\delta t^p, \chi \delta t), \delta_{max})$.
 7. If the next time step is too long ($t > t_0 + \Delta T$) then shorten the time-step to finish at the correct time.
 8. If $t < t_0 + \Delta T$ then go back to step 1 else exit.

The algorithm requires three constants. δ is the required precision. The constants $\beta < 1$, and $\chi > 1$ characterize the smoothness of the algorithm: the proposed timestep is β times the required (nr. 2), and it is increased only when the proposed one is bigger than χ times the current timestep (nr. 6). Overall, these two constants reduces updated frequency of the timestep. The last two parameters δ_{max} and δ_{min} define the maximum and minimum timesteps. In the following projects we always used the following set of parameters: $\beta = 0.9$, $\chi = 5$ and $\delta = 10^{-5}$. The maximum and minimum timestep are chosen accordingly to the project.

Besides the very conservative and not aggressive implementation of our adaptive integrator (the Euler error overestimates the actual error and the chances to update the timestep are kept low by β and χ) this approach overcomes the classical bottleneck in computer simulations given by a poorly chosen time-step. When the forces are small, the integration speeds up, on the contrary, the integrator automatically decreases its stepping if there are transients with stiff forces, and returns to a longer timestep when the transient is over.

We gain than in speed and precision, but we loose the time-reversibility and energy conservation. In the context of the following chapters this is not a major issue because we study systems that are naturally dissipative. However, if the energy conservation is an important aspect of the simulation, for example in the case of a gas of hard-spheres, then this algorithm may not be the best choice.

Bibliography

- [1] J. Howard. *Mechanics of Motor Proteins and the Cytoskeleton*. Sinauer Associates, 2001.
- [2] J. S. Guasto, R. Rusconi, and R. Stocker. Fluid Mechanics of Planktonic Microorganisms. *Annu. Rev. Fluid. Mech.*, 44(1):373–400, 2012. doi: 10.1146/annurev-fluid-120710-101156.
- [3] R. D. Leonardo, L. Angelani, D. Dell’Arciprete, G. Ruocco, V. Iebba, S. Schippa, M. P. Conte, F. Mecarini, F. D. Angelis, and E. D. Fabrizio. Bacterial ratchet motors. *Proc. Nat. Acad. Sci. USA*, 107(21):9541–9545, 2010. doi: 10.1073/pnas.0910426107.
- [4] G. Gompper. Der Weg zum schwimmenden Nanoroboter. *Spektrum der Wissenschaft*, pages 84–91, April 2015.
- [5] J. Gray and G. J. Hancock. The Propulsion of Sea-Urchin Spermatozoa. *J. Exp. Biol.*, 32(4):802–814, 1955.
- [6] H. C. Berg and D. A. Brown. Chemotaxis in *Escherichia coli* analysed by Three-dimensional Tracking. *Nature*, 239(5374):500–504, 1972. doi: 10.1038/239500a0.
- [7] E. M. Purcell. Life at low Reynolds number. *Am. J. Phys.*, 45(1):3, 1977. doi: 10.1119/1.10903.
- [8] S. Childress. *Mechanics of Swimming and Flying*. Cambridge Studies in Mathematical Biology. Cambridge University Press, 1981.
- [9] J. Elgeti, R. G. Winkler, and G. Gompper. Physics of microswimmers—single

- particle motion and collective behavior: a review. *Rep. Prog. Phys.*, 78(5):056601, 2015. doi: 10.1088/0034-4885/78/5/056601.
- [10] J. Lighthill. Flagellar Hydrodynamics. *SIAM Rev.*, 18(2):161–230, 1976. doi: 10.1137/1018040.
- [11] P. H. Raven, R. F. Evert, and S. E. Eichhorn. *Biology of Plants*. W. H. Freeman, 2005.
- [12] E. Knobil and J. D. Neill. *Knobil and Neill's Physiology of Reproduction*. Gulf Professional Publishing, 2006.
- [13] B. Baccetti, B. Gibbons, and I. Gibbons. Bidirectional swimming in spermatozoa of Tephritid flies. *J. Submicrosc. Cytol. Pathol.*, 21(4):619–625, 1989.
- [14] E. Gaffney, H. Gadêlha, D. Smith, J. Blake, and J. Kirkman-Brown. Mammalian Sperm Motility: Observation and Theory. *Annu. Rev. Fluid. Mech.*, 43(1):501–528, 2011. doi: 10.1146/annurev-fluid-121108-145442.
- [15] U. B. Kaupp. 100 years of sperm chemotaxis. *J. Gen. Physiol.*, 140(6):583–586, 2012. doi: 10.1085/jgp.201210902.
- [16] C. J. Brokaw. Bending moments in free-swimming flagella. *J. Exp. Biol.*, 53(2):445–464, 1970.
- [17] I. H. Riedel, K. Kruse, and J. Howard. A Self-Organized Vortex Array of Hydrodynamically Entrained Sperm Cells. *Science*, 309(5732):300–303, 2005. doi: 10.1126/science.1110329.
- [18] Y. Yang, J. Elgeti, and G. Gompper. Cooperation of sperm in two dimensions: Synchronization, attraction, and aggregation through hydrodynamic interactions. *Phys. Rev. E*, 78(6):061903, 2008. doi: 10.1103/PhysRevE.78.061903.
- [19] K. Marx. *Self-propelled Rod-Like Swimmers Near Surfaces*. PhD thesis, Universität zu Köln, 2011.

-
- [20] M. Abkenar, K. Marx, T. Auth, and G. Gompper. Collective behavior of penetrable self-propelled rods in two dimensions. *Phys. Rev. E*, 88(6):062314, 2013. doi: 10.1103/PhysRevE.88.062314.
- [21] T. Vicsek and A. Zafeiris. Collective motion. *Physics Reports*, 517(3–4):71–140, 2012. doi: 10.1016/j.physrep.2012.03.004.
- [22] H. Moore, K. Dvorková, N. Jenkins, and W. Breed. Exceptional sperm cooperation in the wood mouse. *Nature*, 418(6894):174–177, 2002. doi: 10.1038/nature00832.
- [23] H. S. Fisher and H. E. Hoekstra. Competition drives cooperation among closely related sperm of deer mice. *Nature*, 463(7282):801–803, 2010. doi: 10.1038/nature08736.
- [24] G. Nicolis and I. Prigogine. *Self-organization in Nonequilibrium Systems: From Dissipative Structures to Order Through Fluctuations*. Wiley, 1977.
- [25] A. M. Turing. The chemical basis of morphogenesis. *B. Math. Biol.*, 52(1): 153–197, 1990.
- [26] C. R. Doering, C. Mueller, and P. Smereka. Interacting particles, the stochastic Fisher–Kolmogorov–Petrovsky–Piscounov equation, and duality. *Physica. A*, 325(1–2):243–259, 2003. doi: 10.1016/S0378-4371(03)00203-6.
- [27] F. Borgogno, P. D’Odorico, F. Laio, and L. Ridolfi. Mathematical models of vegetation pattern formation in ecohydrology. *Rev. Geophys.*, 47(1), 2009. doi: 10.1029/2007RG000256.
- [28] P. Satir. Studies on Cilia III. Further Studies on the Cilium Tip and a ”Sliding Filament” Model of Ciliary Motility. *J. Cell. Biol.*, 39(1):77–94, 1968. doi: 10.1083/jcb.39.1.77.
- [29] K. E. Machin. Wave Propagation along Flagella. *J. Exp. Biol.*, 35(4):796–806, 1958.

- [30] C. J. Brokaw. Bend Propagation by a Sliding Filament Model for Flagella. *J. Exp. Biol.*, 55(2):289–304, 1971.
- [31] J. Lubliner. An analysis of interfilament shear in flagella. *J. Theor. Biol.*, 41(1):119–125, 1973. doi: 10.1016/0022-5193(73)90192-6.
- [32] E. Lauga and T. Powers. The hydrodynamics of swimming microorganisms. *Rep. Prog. Phys.*, 72:096601, 2009.
- [33] S. B. Babu and H. Stark. Modeling the locomotion of the African trypanosome using multi-particle collision dynamics. *New J. Phys.*, 14(8):085012, 2012. doi: 10.1088/1367-2630/14/8/085012.
- [34] M. L. Ginger, N. Portman, and P. G. McKean. Swimming with protists: Perception, motility and flagellum assembly. *Nat. Rev. Microbiol.*, 6(11):838–850, 2008. doi: 10.1038/nrmicro2009.
- [35] J. Elgeti and G. Gompper. Emergence of metachronal waves in cilia arrays. *Proc. Nat. Acad. Sci. USA*, 110(12):4470–4475, 2013. doi: 10.1073/pnas.1218869110.
- [36] H. J. Hoops and G. B. Witman. Outer doublet heterogeneity reveals structural polarity related to beat direction in *Chlamydomonas* flagella. *J. Cell. Biol.*, 97(3):902–908, 1983. doi: 10.1083/jcb.97.3.902.
- [37] M. Hines and J. J. Blum. Bend propagation in flagella. I. Derivation of equations of motion and their simulation. *Biophys J*, 23(1):41–57, 1978.
- [38] C. J. Brokaw. Bend Propagation along Flagella. *Nature*, 209(5019):161–163, 1966. doi: 10.1038/209161a0.
- [39] J. Lubliner and J. Blum. Model of flagellar waves. *J. Theor. Biol.*, 34(3): 515–534, 1972. doi: 10.1016/0022-5193(72)90139-7.
- [40] C. Shingyoji, J. Katada, K. Takahashi, and I. R. Gibbons. Rotating the plane of imposed vibration can rotate the plane of flagellar beating in sea-urchin sperm without twisting the axoneme. *J. Cell. Sci.*, 98(2):175–181, 1991.

- [41] R. E. Goldstein, M. Polin, and I. Tuval. Emergence of Synchronized Beating during the Regrowth of Eukaryotic Flagella. *Phys. Rev. Lett.*, 107(14):148103, 2011. doi: 10.1103/PhysRevLett.107.148103.
- [42] D. R. Brumley, K. Y. Wan, M. Polin, and R. E. Goldstein. Flagellar synchronization through direct hydrodynamic interactions. *eLife Sciences*, 3:e02750, 2014. doi: 10.7554/eLife.02750.
- [43] F. Jülicher, K. Dierkes, B. Lindner, J. Prost, and P. Martin. Spontaneous movements and linear response of a noisy oscillator. *Eur. Phys. J. E*, 29(4): 449–460, 2009. doi: 10.1140/epje/i2009-10487-5.
- [44] S. Camalet, F. Jülicher, and J. Prost. Self-Organized Beating and Swimming of Internally Driven Filaments. *Phys. Rev. Lett.*, 82(7):1590–1593, 1999. doi: 10.1103/PhysRevLett.82.1590.
- [45] A. Hilfinger, A. K. Chattopadhyay, and F. Jülicher. Nonlinear dynamics of cilia and flagella. *Phys. Rev. E*, 79(5):051918, 2009. doi: 10.1103/PhysRevE.79.051918.
- [46] P. V. Bayly and K. S. Wilson. Equations of Interdoublet Separation during Flagella Motion Reveal Mechanisms of Wave Propagation and Instability. *Biophys. J*, 107(7):1756–1772, 2014. doi: 10.1016/j.bpj.2014.07.064.
- [47] C. B. Lindemann. Testing the Geometric Clutch hypothesis. *Biol. Cell*, 96(9): 681–690, 2004. doi: 10.1016/j.biocel.2004.08.001.
- [48] D. W. Pelle, C. J. Brokaw, K. A. Lesich, and C. B. Lindemann. Mechanical properties of the passive sea urchin sperm flagellum. *Cell. Motil. Cytoskel*, 66(9):721–735, 2009. doi: 10.1002/cm.20401.
- [49] J. Lighthill. *Mathematical Biofluidynamics*. Society for Industrial and Applied Mathematics, Philadelphia, Pa., 1987.
- [50] G. Gompper. Microswimmers. In *Macromolecular Systems in Soft and Living Matter*, number 42 in IFF Spring School. 2011.

- [51] A. Najafi and R. Golestanian. Coherent hydrodynamic coupling for stochastic swimmers. *Europhys. Lett.*, 90(6):68003, 2010. doi: 10.1209/0295-5075/90/68003.
- [52] B. M. Friedrich, I. H. Riedel-Kruse, J. Howard, and F. Jülicher. High-Precision Tracking of Sperm Swimming Fine Structure Provides Strong Test of Resistive Force Theory. *J. Exp. Biol.*, 213(8):1226–1234, 2010. doi: 10.1242/jeb.039800.
- [53] J. B. Keller and S. I. Rubinow. Slender-body theory for slow viscous flow. *J. Fluid. Mech*, 75(04):705–714, 1976.
- [54] B. Rodenborn, C.-H. Chen, H. L. Swinney, B. Liu, and H. P. Zhang. PNAS Plus: Propulsion of microorganisms by a helical flagellum. *Proc. Nat. Acad. Sci. USA*, 110(5):E338–E347, 2013. doi: 10.1073/pnas.1219831110.
- [55] M. M. Tirado, C. L. Martínez, and J. G. de la Torre. Comparison of theories for the translational and rotational diffusion coefficients of rod-like macromolecules. Application to short DNA fragments. *J. Chem. Phys*, 81(4):2047–2052, 1984. doi: 10.1063/1.447827.
- [56] M. Doi. *The Theory of Polymer Dynamics*. Number 73 in The International Series of Monographs on Physics. Oxford University Press, 1988.
- [57] C. Broedersz and F. MacKintosh. Modeling semiflexible polymer networks. *Rev. Mod. Phys.*, 86(3):995–1036, 2014. doi: 10.1103/RevModPhys.86.995.
- [58] F. Nédélec, T. Surrey, A. C. Maggs, and S. Leibler. Self-organization of microtubules and motors. *Nature*, 389(6648):305–308, 1997. doi: 10.1038/38532.
- [59] S. Linder and M. Aepfelbacher. Podosomes: Adhesion hot-spots of invasive cells. *Trends. Cell. Biol*, 13(7):376–385, 2003. doi: 10.1016/S0962-8924(03)00128-4.
- [60] K. van den Dries, M. B. M. Meddens, S. de Keijzer, S. Shekhar, V. Subramaniam, C. G. Figdor, and A. Cambi. Interplay between myosin IIA-mediated contractility and actin network integrity orchestrates podosome composition and oscillations. *Nat Commun*, 4:1412, 2013. doi: 10.1038/ncomms2402.

-
- [61] C. P. Brangwynne, G. H. Koenderink, E. Barry, Z. Dogic, F. C. MacKintosh, and D. A. Weitz. Bending Dynamics of Fluctuating Biopolymers Probed by Automated High-Resolution Filament Tracking. *Biophys. J*, 93(1):346–359, 2007. doi: 10.1529/biophysj.106.096966.
- [62] C. Heussinger, M. Bathe, and E. Frey. Statistical Mechanics of Semiflexible Bundles of Wormlike Polymer Chains. *Phys. Rev. Lett.*, 99(4):048101, 2007. doi: 10.1103/PhysRevLett.99.048101.
- [63] K. Soda. Dynamics of Stiff Chains. I. Equation of Motion. *J. Phys. Soc. Jpn*, 35(3):866–870, 1973. doi: 10.1143/JPSJ.35.866.
- [64] S. Camalet and F. Jülicher. Generic aspects of axonemal beating. *New. J. Phys.*, 2:24–24, 2000. doi: 10.1088/1367-2630/2/1/324.
- [65] H. Gadêlha, E. A. Gaffney, D. J. Smith, and J. C. Kirkman-Brown. Nonlinear instability in flagellar dynamics: a novel modulation mechanism in sperm migration? *J. R. Soc. Interface*, 7(53):1689–1697, 2010. doi: 10.1098/rsif.2010.0136.
- [66] C. H. Wiggins, D. Riveline, A. Ott, and R. E. Goldstein. Trapping and wiggling: Elastohydrodynamics of driven microfilaments. *Biophys J*, 74(2 Pt 1):1043–1060, 1998.
- [67] L. Harnau, R. G. Winkler, and P. Reineker. Dynamic structure factor of semiflexible macromolecules in dilute solution. *J. Chem. Phys.*, 104(16):6355–6368, 1996. doi: 10.1063/1.471297.
- [68] S. R. Aragon and R. Pecora. Dynamics of wormlike chains. *Macromolecules*, 18(10):1868–1875, 1985.
- [69] K. Kroy and E. Frey. Dynamic scattering from solutions of semiflexible polymers. *Phys. Rev. E*, 55(3):3092, 1997.
- [70] M. Peltomäki and G. Gompper. Sedimentation of single red blood cells. *Soft Matter*, 9(34):8346–8358, 2013. doi: 10.1039/C3SM50592H.

- [71] R. G. Winkler, P. Reineker, and L. Harnau. Models and equilibrium properties of stiff molecular chains. *J. Chem. Phys.*, 101(9):8119–8129, 1994. doi: 10.1063/1.468239.
- [72] M. Cosentino Lagomarsino, I. Pagonabarraga, and C. Lowe. Hydrodynamic Induced Deformation and Orientation of a Microscopic Elastic Filament. *Phys. Rev. Lett.*, 94(14), 2005. doi: 10.1103/PhysRevLett.94.148104.
- [73] K. E. Machin. The Control and Synchronization of Flagellar Movement. *Proc. R. Soc. Lond. B*, 158(970):88–104, 1963. doi: 10.1098/rspb.1963.0036.
- [74] C. J. Brokaw. Computer Simulation of Flagellar Movement. *Biophys. J.*, 12(5): 564–586, 1972. doi: 10.1016/S0006-3495(72)86104-6.
- [75] J. Lubliner and J. Blum. Model for bend propagation in flagella. *J. Theor. Biol.*, 31(1):1–24, 1971. doi: 10.1016/0022-5193(71)90117-2.
- [76] T. Guérin, J. Prost, and J.-F. Joanny. Dynamical behavior of molecular motor assemblies in the rigid and crossbridge models. *Eur. Phys. J. E*, 34(6):21, 2011. doi: 10.1140/epje/i2011-11060-5.
- [77] F. Taslimi. *End-Functionalized Rodlike Colloid Suspensions Under Shear Flow*. PhD thesis, RWTH Aachen, 2013.
- [78] M. Ripoll. Mesoscale Hydrodynamics. In *Macromolecular Systems in Soft and Living Matter*, number 42 in IFF Spring School. 2011.
- [79] J. Elgeti, U. B. Kaupp, and G. Gompper. Hydrodynamics of Sperm Cells near Surfaces. *Biophys. J.*, 99(4):1018–1026, 2010. doi: 10.1016/j.bpj.2010.05.015.
- [80] M. Lagomarsino, P. Jona, and B. Bassetti. Metachronal waves for deterministic switching two-state oscillators with hydrodynamic interaction. *Phys. Rev. E*, 68(2), 2003. doi: 10.1103/PhysRevE.68.021908.
- [81] G. J. Stephens, B. Johnson-Kerner, W. Bialek, and W. S. Ryu. Dimensionality and Dynamics in the Behavior of *C. elegans*. *Plos. Comput. Biol.*, 4(4):e1000028, 2008. doi: 10.1371/journal.pcbi.1000028.

- [82] D. Dalle. Comparison of numerical techniques for Euclidean curvature. *Rose–Hulman Undergraduate Math. J.*, 7(1):1–29, 2006.
- [83] A. Pikovsky, M. Rosenblum, and J. Kurths. *Synchronization: A Universal Concept in Nonlinear Sciences*. Cambridge University Press, Cambridge, 1 edition edition, 2003.
- [84] Y. Kuramoto. Phase Dynamics of Weakly Unstable Periodic Structures. *Prog. Theor. Phys.*, 71(6):1182–1196, 1984. doi: 10.1143/PTP.71.1182.
- [85] B. Kralemann, L. Cimponeriu, M. Rosenblum, A. Pikovsky, and R. Mrowka. Phase dynamics of coupled oscillators reconstructed from data. *Phys. Rev. E*, 77(6):066205, 2008. doi: 10.1103/PhysRevE.77.066205.
- [86] K. Y. Wan and R. E. Goldstein. Rhythmicity, Recurrence, and Recovery of Flagellar Beating. *Phys. Rev. Lett.*, 113(23), 2014. doi: 10.1103/PhysRevLett.113.238103.
- [87] R. Ma, G. S. Klindt, I. H. Riedel-Kruse, F. Jülicher, and B. M. Friedrich. Active Phase and Amplitude Fluctuations of Flagellar Beating. *Phys. Rev. Lett.*, 113(4):048101, 2014. doi: 10.1103/PhysRevLett.113.048101.
- [88] G. Saggiorato, J. Elgeti, R. G. Winkler, and G. Gompper. Conformations, hydrodynamic interactions, and instabilities of sedimenting semiflexible filaments. *Phys. Rev. E*, 11(37):7337–7344, . doi: 10.1039/C5SM01069A.
- [89] P. E. Arratia, C. C. Thomas, J. Diorio, and J. P. Gollub. Elastic Instabilities of Polymer Solutions in Cross-Channel Flow. *Phys. Rev. Lett.*, 96(14):144502, 2006. doi: 10.1103/PhysRevLett.96.144502.
- [90] C. M. Schroeder, H. P. Babcock, E. S. G. Shaqfeh, and S. Chu. Observation of Polymer Conformation Hysteresis in Extensional Flow. *Science*, 301(5639):1515–1519, 2003. doi: 10.1126/science.1086070.
- [91] N. Coq, A. Bricard, F.-D. Delapierre, L. Malaquin, O. du Roure, M. Fermigier, and D. Bartolo. Collective Beating of Artificial Microcilia. *Phys. Rev. Lett.*, 107(1):014501, 2011. doi: 10.1103/PhysRevLett.107.014501.

- [92] J. Happel and H. Brenner. *Low Reynolds Number Hydrodynamics: With Special Applications to Particulate Media*. Springer, 1983.
- [93] M. Manghi, X. Schlagberger, Y.-W. Kim, and R. R. Netz. Hydrodynamic effects in driven soft matter. *Soft Matter*, 2(8):653–668, 2006.
- [94] I. Llopis, I. Pagonabarraga, M. Cosentino Lagomarsino, and C. P. Lowe. Sedimentation of pairs of hydrodynamically interacting semiflexible filaments. *Phys. Rev. E*, 76(6):061901, 2007. doi: 10.1103/PhysRevE.76.061901.
- [95] X. Schlagberger and R. R. Netz. Orientation of elastic rods in homogeneous Stokes flow. *Europhys. Lett.*, 70(1):129, 2005. doi: 10.1209/epl/i2004-10461-5.
- [96] S. Y. Reigh, R. G. Winkler, and G. Gompper. Synchronization and bundling of anchored bacterial flagella. *Soft Matter*, 8(16):4363, 2012. doi: 10.1039/c2sm07378a.
- [97] M. L. Ekiel-Jeżewska, T. Gubiec, and P. Szymczak. Stokesian dynamics of close particles. *Phys. Fluids*, 20(6):063102, 2008. doi: 10.1063/1.2930881.
- [98] M. L. Ekiel-Jeżewska. Class of periodic and quasiperiodic trajectories of particles settling under gravity in a viscous fluid. *Phys. Rev. E*, 90(4), 2014. doi: 10.1103/PhysRevE.90.043007.
- [99] R. G. Winkler. Diffusion and segmental dynamics of rodlike molecules by fluorescence correlation spectroscopy. *J. Chem. Phys.*, 127(5):054904, 2007. doi: 10.1063/1.2753160.
- [100] B. M. Friedrich and F. Jülicher. Chemotaxis of sperm cells. *Proc. Nat. Acad. Sci. USA*, 104(33):13256–13261, 2007.
- [101] L. Alvarez, B. M. Friedrich, G. Gompper, and U. B. Kaupp. The computational sperm cell. *Trends Cell. Biol.*, 24(3):198–207, 2014. doi: 10.1016/j.tcb.2013.10.004.
- [102] J. Elgeti. *Sperm and Cilia Dynamics*. PhD thesis, Universität zu Köln, 2006.

-
- [103] G. Saggiorato, J. Jikeli, L. Alvarez, J. Elgeti, G. Gompper, and B. Kaupp. Steering with higher harmonics. *In preparation*, .
- [104] U. B. Kaupp, N. D. Kashikar, and I. Weyand. Mechanisms of Sperm Chemotaxis. *Annu. Rev. Physiol*, 70(1):93–117, 2008. doi: 10.1146/annurev.physiol.70.113006.100654.
- [105] O. H. Shapiro, V. I. Fernandez, M. Garren, J. S. Guasto, F. P. Debaillon-Vesque, E. Kramarsky-Winter, A. Vardi, and R. Stocker. Vortical ciliary flows actively enhance mass transport in reef corals. *Proc. Nat. Acad. Sci. USA*, 111(37):13391–13396, 2014. doi: 10.1073/pnas.1323094111.
- [106] C. Wollin and H. Stark. Metachronal waves in a chain of rowers with hydrodynamic interactions. *Eur. Phys. J. E*, 34(4):1–10, 2011. doi: 10.1140/epje/i2011-11042-7.
- [107] N. Bruot, J. Kotar, F. de Lillo, M. Cosentino Lagomarsino, and P. Cicutta. Driving Potential and Noise Level Determine the Synchronization State of Hydrodynamically Coupled Oscillators. *Phys. Rev. Lett*, 109(16), 2012. doi: 10.1103/PhysRevLett.109.164103.
- [108] T. Guérin, J. Prost, P. Martin, and J.-F. Joanny. Coordination and collective properties of molecular motors: Theory. *Curr. Opin. Cell. Biol*, 22(1):14–20, 2010. doi: 10.1016/j.ceb.2009.12.012.
- [109] S. H. Strogatz. *Nonlinear Dynamics And Chaos: With Applications To Physics, Biology, Chemistry, And Engineering*. Westview Press, 1 edition, 2001.
- [110] I. S. Aranson and L. Kramer. The world of the complex Ginzburg-Landau equation. *Rev. Mod. Phys.*, 74(1):99–143, 2002. doi: 10.1103/RevModPhys.74.99.
- [111] V. García-Morales and K. Krischer. The complex Ginzburg–Landau equation: An introduction. *Contemp. Phys*, 53(2):79–95, 2012. doi: 10.1080/00107514.2011.642554.

- [112] H. Haken. Generalized Ginzburg-Landau equations for phase transition-like phenomena in lasers, nonlinear optics, hydrodynamics and chemical reactions. *Z. Phys. B Con. Mat.*, 21(1):105–114, 1975.
- [113] P. Malgaretti, I. Pagonabarraga, and D. Frenkel. Running Faster Together: Huge Speed up of Thermal Ratchets due to Hydrodynamic Coupling. *Phys. Rev. Lett.*, 109(16), 2012. doi: 10.1103/PhysRevLett.109.168101.
- [114] T. Guérin, J. Prost, and J.-F. Joanny. Dynamic Instabilities in Assemblies of Molecular Motors with Finite Stiffness. *Phys. Rev. Lett.*, 104(24):248102, 2010. doi: 10.1103/PhysRevLett.104.248102.
- [115] J. F. G. Auchmuty and G. Nicolis. Bifurcation analysis of reaction-diffusion equations—iii. Chemical oscillations. *B. Math. Biol.*, 38(4):325–350, 1976. doi: 10.1016/S0092-8240(76)80015-8.
- [116] J. E. Guyer, D. Wheeler, and J. A. Warren. FiPy: Partial Differential Equations with Python. *IEEE Comput. Sci. Eng.*, 11(3):6–15, 2009. doi: 10.1109/MCSE.2009.52.
- [117] C. J. Brokaw. Effects of Increased Viscosity on the Movements of Some Invertebrate Spermatozoa. *J. Exp. Biol.*, 45(1):113–139, 1966.
- [118] D. Tam and A. E. Hosoi. Optimal kinematics and morphologies for spermatozoa. *Phys. Rev. E*, 83(4):045303, 2011.
- [119] L. Verlet. Computer "Experiments" on Classical Fluids. I. Thermodynamical Properties of Lennard-Jones Molecules. *Phys. Rev.*, 159(1):98–103, 1967. doi: 10.1103/PhysRev.159.98.
- [120] M. Allen and D. Tildesley. *Computer Simulation of Liquids (Oxford Science Publications)*. Oxford University Press, 1989.
- [121] D. Frenkel. *Understanding Molecular Simulation: From Algorithms to Applications*. Number 1 in Computational science series. Academic Press, San Diego, 2nd edition, 2002.

- [122] P. Eastman, M. S. Friedrichs, J. D. Chodera, R. J. Radmer, C. M. Bruns, J. P. Ku, K. A. Beauchamp, T. J. Lane, L.-P. Wang, D. Shukla, T. Tye, M. Houston, T. Stich, C. Klein, M. R. Shirts, and V. S. Pande. OpenMM 4: A Reusable, Extensible, Hardware Independent Library for High Performance Molecular Simulation. *J. Chem. Theory Comput.*, 9(1):461–469, 2013. doi: 10.1021/ct300857j.
- [123] Galassi , M. and et al. *GNU Scientific Library Reference Manual (3Rd Ed.)*. GNU Foundation, 3rd edition, 2013.
- [124] M. C. Marchetti, J.-F. Joanny, S. Ramaswamy, T. B. Liverpool, J. Prost, M. Rao, and R. A. Simha. Soft Active Matter. Technical Report 1207.2929, 2012.
- [125] J. Toner, Y. Tu, and S. Ramaswamy. Hydrodynamics and phases of flocks. *Ann. Phys-New York*, 318(1):170–244, 2005. doi: 10.1016/j.aop.2005.04.011.
- [126] T. Mora and W. Bialek. Are biological systems poised at criticality? *J. Stat. Phys.*, 144(2):268–302, 2011. doi: 10.1007/s10955-011-0229-4.

Erklärung

Ich versichere, dass ich die von mir vorgelegte Dissertation selbständig angefertigt, die benutzten Quellen und Hilfsmittel vollständig angegeben und die Stellen der Arbeit – einschließlich Tabellen, Karten und Abbildungen –, die anderen Werken im Wortlaut oder dem Sinn nach entnommen sind, in jedem Einzelfall als Entlehnung kenntlich gemacht habe; dass diese Dissertation noch keiner anderen Fakultät oder Universität zur Prüfung vorgelegen hat; dass sie – abgesehen von unten angegebenen Teilpublikationen – noch nicht veröffentlicht worden ist, sowie, dass ich eine solche Veröffentlichung vor Abschluss des Promotionsverfahrens nicht vornehmen werde. Die Bestimmungen der Promotionsordnung sind mir bekannt. Die von mir vorgelegte Dissertation ist von Prof. Dr. Gerhard Gompper betreut worden.

Jülich, 30 Okt. 2015

Guglielmo Saggiorato